Chirality Control and Magnetization Dynamics in a Dual Vortex Spin Valve Nanopillar

by

Joseph Edward Kolthammer
B.S., Case Western Reserve University, 2006

A Dissertation Submitted in Partial Fulfillment of the
Requirements for the Degree of

DOCTOR OF PHILOSOPHY

in the Department of Physics and Astronomy

Chirality Control and Magnetization Dynamics in a Dual Vortex Spin Valve Nanopillar

by

Joseph Edward Kolthammer

B.S., Case Western Reserve University, 2006

Supervisory Committee

Dr. Byoung-Chul Choi, Supervisor

Department of Physics and Astronomy

Dr. Rogerio de Sousa, Departmental Member

Department of Physics and Astronomy

Dr. Geoff Steeves, Departmental Member

Department of Physics and Astronomy

Dr. Robin Hicks, Outside Member

Department of Chemistry

Abstract

A new method for dynamic chirality control of a magnetic vortex is demonstrated with micromagnetic simulations. Spin transfer torque and giant magnetoresistance in an asymmetric spin valve nanopillar provide fast, reliable, and compact single-bit manipulation and readout. Magnetization relaxation following chirality switching proceeds via formation and dissipation of spin wave eigenmodes. Combined time- and frequency-domain analysis reveals a novel radial eigenmode spectrum with large edge amplitudes and nonuniform phase in the fundamental mode, in contrast with existing analytical models and experimental precedents. With the aim to determine the sources of this departure, we implement signal processing methods to identify and characterize the effects of interlayer coupling and nanoscale spatial confinement on the magnetization dynamics. Variation of the interlayer coupling and relative chirality is found to modify the eigenfrequencies but not the eigenfunctions. Examination of the interlayer phase and dynamic stray field provides quantitative and qualitative explanation of frequency splitting with relative chirality.

Contents

List of Figures

List of Tables

Publications

1. *Modified high frequency radial spin wave mode spectrum in a chirality-controlled nanopillar*
   J. E. Kolthammer, J. Rudge, B. C. Choi, and Y. K. Hong, Spin **6**, 1650008 (2016).

2. *Sub-nanosecond time-resolved near-field scanning magneto-optical microscope*
   J. Rudge, H. Xu, J. Kolthammer, Y. K. Hong, and B. C. Choi, Review of Scientific Instruments **86**, 023703 (2015).

3. *Magnetic properties of nanostructured Fe-Co alloys*
   C. Rizal, J. Kolthammer, R. K. Pokharel, and B. C. Choi, Journal of Applied Physics **113**, 113905 (2013).

4. *Current pulse induced toggle switching of dual-vortex magnetization in Ni80Fe20/Cu/Co nanopillar element*
   J. Kolthammer, R. Gardner, Th. Speliotis, Y. K. Hong, G. Abo, Q. Liu, and B. C. Choi, Journal of Applied Physics **112**, 083928 (2012).

5. *Magnetization process in vortex-imprinted Ni80Fe20/Ir20Mn80 square elements*
   H. Xu, J. Kolthammer, J. Rudge, E. Girgis, B. C. Choi, Y. K. Hong, G. Abo, Th. Speliotis, and D. Niarchos, Journal of Magnetics **16**, 83 (2011).

6. *Nonequilibrium process of magnetization switching influenced by thermal spin fluctuations*
   B. C. Choi, Y. K. Hong, J. Rudge, E. Girgis, J. Kolthammer, and G. W. Donohoe, Physica Status Solidi B **244**, 4486 (2007).

7. *Spin-current pulse induced switching of vortex chirality in PermalloyCuCo nanopillars*
   B. C. Choi, J. Rudge, E. Girgis, J. Kolthammer, Y. K. Hong, and A. Lyle, Applied Physics Letters **91**, 2005 (2007).

8. *Dynamics of magnetic vortex core switching in Fe nanodisks by applying in-plane magnetic field pulse*
   Q. F. Xiao, J. Rudge, E. Girgis, J. Kolthammer, B. C. Choi, Y. K. Hong, and G. W. Donohoe, Journal of Applied Physics **102**, 103904 (2007).

Acknowledgments

Thanks to Professor Byoung-Chul Choi for his guidance, my parents for their support, my brothers for leading the way, and my partner for her patience.

Chapter 1

Introduction

Computing in the information age has evolved with persistent technological advancement punctuated by fundamental shifts in research and development. Monotonically increasing performance, proliferation, and miniaturization have diverse implications for social change [1, 2], economic growth [3, 4, 5], health care [6], and poverty reduction [7]. Limits to advancement emerge aperiodically with scaling and provide new and compelling problems for applied physics. As throughout history [8], magnetism and magnetic materials bridge these practical applications and fundamental interests, and a central goal of nanomagnetism research is to identify and characterize the effects of nanoscale spatial confinement on ferromagnetic dynamics. This thesis presents new contributions within that scope.

The technological and physical motivations for the work presented in this thesis are detailed in this chapter, beginning with a brief history of magnetic memory, persistent challenges, and relevant figures of merit. The representative cases of hard disk drive and memory development get particular focus as they span the historical and technological extent. Then, present efforts in magnetic memory and the state of experimental spintronics

are reviewed, contextualizing the system of interest in the balance of this work. Finally, the contents of the remaining chapters are previewed.

1.1 A brief history of memory

After the discovery of the point-contact transistor in 1947 [9], the transistorization of mainframe computers in the 1950s unlocked rapid improvements in computational efficiency. These practical gains in processing made necessary complementary advancements in computer memory. Magnetic core memory, developed in 1951 and commercialized by 1955, became the standard implementation of random access memory (RAM) in mainframe computers. Magnetic core memory is a regular grid of ferromagnetic toroid bits threaded by wires. To write a bit, coincident current pulses are directed through two perpendicular write wires intersecting in the bit. The pulses are individually subcritical, but the Oersted field of their combined amplitude is sufficient to set the binary, clockwise or counterclockwise magnetic state of the bit. This half-select addressing ensures that only the target bit in the grid is switched. The read process is similar: Assuming the bit is in a zero state, the pulse controller attempts to write a one. If switching occurs, an induced voltage pulse is picked up via a sense wire, indicating that the bit was indeed a zero, and vice versa. Scaling aside, core memory saw few changes in the subsequent two decades. This basic architecture for computer memory introduces the original figures of merit: readability, writeability, areal density, and cost per storage unit. With thin film fabrication still too exotic for mainstream production, the latter two points formed a road block for magnetic core memory. For these interdependent reasons, transistor-based dynamic random access memory (DRAM) overtook magnetic core memory in the early 1970s. Incremental improvements in design and fabrication ensured steady growth in DRAM performance over the subsequent decades, and

it is the dominant paradigm to this day.

Like early main memory, secondary storage also relied on magnetic means. Mechanical hard disk drives were introduced in 1956, became standard for mainframes in the 1960s and accessible for personal computers in the 1980s, and remain foremost in medium term data storage today. Hard disk bits are stored in regions of ferromagnetic thin films on rotating platters. Bits are accessed with read/write heads mounted on actuated arms that translate radially across the platters. To write a bit, a current is passed through the write transducer, essentially an electromagnet, generating a magnetic field that imposes the desired bit polarization on the adjacent region of the platter. This write mechanism is still used today. To read bits, in the original implementation, the read head senses the electromotive force induced by the bit stray fields as the platter rotates under the read head.

Hard drive areal density increases by reducing the size of bits. Successively finer radial arm positioning and lower head flying heights, photolithographically patterned thin film write heads, and exchange decoupled granular microstructured media have each played a role in this miniaturization. From 1970 to 1990 areal density increased from 1 to 100 Mbits/in^2, an average of 25% per year [10]. However, there are two basic problems with decreasing bit size: readability and thermal stability of the bit [11].

When sensing a stray field through induction, the signal strength is proportional to the flux captured from the bit, the number of turns of wire on the read head, and the velocity of the head relative to the platter. Flux and the number of turns decreases with miniaturization, and there is a mechanical limit to the angular velocity of the platter. This problem of decreasing read signal strength was addressed with a series of new technologies following the emergence of spintronics in the 1980s, enabled by advances in thin flim fabrication. Spintronic is a portmanteau of spin and electronic describing phenomena and

technologies that rely on the spin as well as the charge of electrons. In 1991, the first hard disk drives shipped with read heads that employed the anisotropic magnetoresistance (AMR) effect [12]. AMR is the variation of electrical resistance with the angle included by the direction of the electric current and the direction of the magnetization in a material. An AMR read head is basically a ferromagnet connected to an ohmmeter – as it flies over a bit, the stray field of the bit rotates the magnetization in the ferromagnet, changing its electrical resistance. Since the stray field is oriented by the bit polarization, the resistance signal corresponds to the bit value. In 1997, read heads debuted based on giant magnetoresistance (GMR), an even more sensitive, multilayer analog to AMR whose discovery warranted a Nobel prize in 2007. The compounded annual growth rates of areal density from 1991 to 1997 and 1997 to 2001 were 60 and 100% respectively. However, despite further developments, including tunneling magnetoresistance (TMR) read heads in 2004, perpendicular magnetic recording in 2005, and shingled magnetic recording in 2013, the areal density growth rate has slowed considerably, to 37% from 2001 to 2010.

The problem of thermal stability is entangled with the problem of read sensitivity. At 1 Tbit/in^2, a hard disk bit covers roughly 650 nm^2 and consists of fewer than 100 exchange-decoupled grains of the ferromagnetic media. The ratio of read signal to media noise, the dominant noise contribution, is inversely proportional to the number of grains per bit [11]; however, grain size has a lower limit due to thermal stability – if the grains become too small, room temperature thermal energy is sufficient to spontaneously switch the bit [13] – and increasing grain stability with magnetic anisotropy increases the requisite write field strength, which in turn is limited by material saturation, field leakage, and heat dissipation.

After an eight orders of magnitude increase in areal density, conventional hard drives are headed for an inevitable interdependent impasse of readability, writability, and

stability.

1.2 Present limits and future integration

A different approach is bit patterning, combining the strengths of magnetic hard disk drives with the individually defined cells of semiconductor RAM. Instead of collective regions on extended media, bits can be encoded in individual elements with geometries defined by lithographic techniques, each larger than a conventional grain, in fact comprised of many exchange coupled grains, but comparable in size to a conventional bit. Each bit is a single magnetic domain with two thermally stable remanent magnetization states and no incidental coupling to neighbouring bits.

Of course, bit patterned media does not have to be magnetic. Transistor-based flash memory, developed from nonmagnetic read-only memory and introduced in 1984, has made significant inroads as lightweight and shock resistant secondary storage media. Flash, an electrically erasable read-only memory rather than RAM, requires neither spinning platters nor read/write head actuation and so integrates well in embedded systems. Likewise it outperforms hard disk drives in bandwidth, and may soon exceed hard disk bit density [14]. However, it suffers from limited write endurance, possible long-term instability, high write voltage (that will not scale with decreasing silicon logic level), and higher production cost per byte than hard disk drives. These qualities make flash unsuitable for high speed memory but advantageous for portable applications. Thus the case of flash introduces the fifth figure of merit, after readability, writeability, density, and cost: energy efficiency. Miniaturization has lead to portable computing – laptop computers, digital cameras, smart phones – and recent surveys indicate that longer battery life is a top priority for consumers. Future bit patterned media should have low power requirements when active and data remanance

	HDD	SRAM	DRAM	Flash	MRAM
Read	9 ms	0.3 ns	10 ns	50 µs	10 ns
Write (erase)	10 ms	0.3 ns	10 ns	1 (0.1) ms	10 ns
Non-volatile	Yes	No	No	Yes	Yes
Endurance/cycles	> 10 yr	10^{16}	10^{16}	10^5	10^{16}
Cell size	Small	Large	Small	Small	Small
Voltage	High	Low	Medium	High	Low
Application	Secondary	Cache	Main	Secondary	Secondary/Main

Table 1.1: Relative merits of current and proposed memory technologies [16, 17, 18, 19].

when unpowered, that is, be non-volatile. And volatility is a persistent problem with main memory as well in both small and large systems: DRAM requires frequent refreshing (every 64 ms is standard) and is responsible for at least 25% of the 100 terawatt-hours of electricity consumed by datacenters in 2013.

Scaling also has implications beyond secondary storage: annual performance increases for microprocessors and RAM have slowed. Microprocessors, whose clock rates plateaued in 2004, have stayed stasis by moving to multi-core architectures. Meanwhile, DRAM architecture is mostly unchanged since 1973, and CPU speed gains significantly outpaced those of DRAM in the microcomputer era, resulting in a bandwidth-limiting performance gap. This relative latency bottleneck is problematic as software increasingly avails parallelism. DRAM latency, already 250 times slower than processors', is no longer improving, and DRAM scaling is expected to reach fundamental limits due to transistor leakage and capacitor breakdown in the next decade, after five orders of magnitude improvement in areal density over the last forty years [15].

A computer or smart phone typically employs, in order of speed, SRAM for processor caches, DRAM for primary memory, and hard disks or flash memory for secondary storage, each with different merits. Magnetic RAM (MRAM), as a so-called universal memory, could in principle fulfill all three roles – denser than SRAM, faster and more energy efficient than DRAM, and faster, more energy efficient, and more durable than flash (Table 1.1). And while SRAM requires a battery for data remanence, and DRAM bits must be refreshed frequently due to leakage, MRAM is non-volatile. Having fewer distinct memory types in a device decreases complexity, increasing reliability and decreasing production cost; the best scenario for many applications is on-chip integration of some or all of the memory subsystems. In the short term, MRAM is ideal to replace embedded flash; in the long term, MRAM or another universal memory could be a central feature in highly integrated systems.

1.3 MRAM and contemporary spintronics

MRAM is essentially magnetic core memory made nanoscale with the benefit of spintronics. The basic unit is a GMR or TMR read head, detailed schematically in Figure 1.1, in which two ferromagnetic layers sandwich a nonmagnetic spacer layer. The magnetization in one ferromagnetic layer is fixed in a given orientation (blue arrow and layer) while the other is free to rotate (light grey). In the case of a hard disk read head, it does so in response to the stray field of a bit. The electrical resistance of the trilayer depends on the angle included by the fixed and free layer magnetizations, therefore it is an analog representation of the state of the bit.

When integrated directly into bit patterned media, the GMR or TMR stack can assume not only the role of reader but also bit storer. Addressing is performed directly via

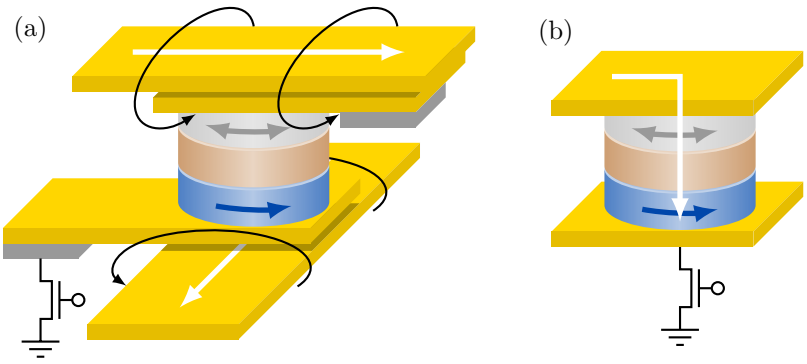

Figure 1.1: Schematic MRAM cells with (a) field and (b) current switching.

wires, like in core memory or RAM. The boolean value of the bit is written directly into the free layer, and read as the resistance of the stack. The first modern implementation, developed since 1995 and produced since 2003, uses current-induced fields for writing. Half-select addressing, like for core memory, is shown in Figure 1.1(a), where the white arrows depict the write currents and the black arrows the write field. This limits scaling, as magnetic fields unavoidably leak, perturbing neighbouring bits, and writing to smaller bits requires larger fields. The solution to the write problem originates in the 1996 discovery of spin transfer torque, essentially that a spin polarized electric current can rotate the magnetization in a ferromagnet. In the trilayer geometry, this means that a current pulse traveling perpendicularly through the layers can switch the free layer orientation, toggling the state of the bit. With this write method, one transistor and one GMR or TMR stack suffice for writing, reading, and storing a bit (Figure 1.1(b)). Current-induced magnetization switching is more compact than field-based writing, requires less power, and scales advantageously with bit size. Prototype MRAM with spin torque transfer write was revealed in 2007, and in 2016, 11 nm, 7.5 µA, 10 ns MRAM was announced, with an error-rate of one in 1.4 billion writes, all competitive figures [20, 21].

While demand for magnetic memory and its CMOS integration has encouraged certain practical short term tracks, a comprehensive sphere of spin-based devices is also un-

der development. Microwave spin torque oscillators outputting in the microwatt range can be tuned between hundreds of MHz and tens of GHz with a combination of material and geometric properties; likewise, nanoscale spin torque diodes can be used to detect and rectify microwave signals [22]. And there are pure spin devices in which charge currents play only supporting roles. One functional basis is spin waves, fundamental magnetization excitations with characteristic frequencies in the GHz range and potential for wave-based computing. Corresponding subfields called magnonics and magnon spintronics have emerged, magnons being the quanta of spin waves [23, 24]. Interfacing magnonic and spintronic circuits is straightforward in principle: spin-magnon transmutation, via spin transfer torque, its thermodynamic reciprocal, spin pumping, and the spin Hall effects, provides a bidirectional path to exchange information between conduction electron spins and magnetization [25]. However, a spin current carried exclusively by magnons rather than spin-polarized electrons precludes the Ohmic waste heat of charge currents in CMOS devices, and a nanoscale magnonic transistor that does not rely on spin torque is one of the persistent challenges for realizing magnonic chips [26]. Several spin wave logic gates have been demonstrated [27], and there are a number of proposals for a complete family of spin wave-based logic devices operating at GHz frequencies [28]. Finally, if a practical material exhibiting 100% spin polarization were found, nonvolatile, reprogrammable magnetic logic could lead to a new paradigm of adaptive microprocessors [29]. Like GMR, TMR, and spin transfer torque before them, realizing these emerging technologies will rely on fine grained fabrication.

Spintronics has adopted topological features of ferromagnets as well, including domain walls, vortices, and skyrmions. Racetrack memory, demonstrated in 2008, features sequential magnetic domains traversing nanowires under the influence of spin transfer torque, acting as bits in a shift register – racetrack memory is to the short-lived magnetic bubble memory of the 1970s as modern MRAM is to magnetic core memory. Numerous

challenges have hindered its development: domain wall control in nanowires requires high current densities and has stochastic sensitivity to fabrication quality, field-based read and write heads fell out of favor for the reasons enumerated above, and proposed 3D packing of wires, necessary for competitive bit density, would require distinct methods of fabrication. Skyrmions, related to the aforementioned bubbles, have recently attracted experimental attention but are difficult to isolate and manipulate and are generally found in more exotic materials [30].

Magnetic vortices are attractive features for study and routine participants in spintronic research [31]. A vortex is a stable, naturally occuring state in patterned thin-film ferromagnets. It has two boolean topological degrees of freedom, polarity and chirality, so a single vortex carries two bits of information. Manipulating these indices is possible with both fields and currents and has led to proposals of vortex- and antivortex-based MRAM cells in the literature. Other vortex based devices have been demonstrated as well. For example, a vortex in the free layer of a GMR or TMR nanopillar can be made to gyrate under the influence of spin transfer torque, forming a discrete order-GHz oscillator [22].

The system described in this thesis unites several of these features. Its basis is a spin valve nanopillar with vortex magnetization configurations in both magnetic layers – a patterned vertical cylindrical element on the nanometric scale is a called a nanopillar, and a metallic GMR stack is called a spin valve, with parallel magnetizations corresponding to an open valve with low electrical resistance and antiparallel to a closed valve with high resistance. Reading and writing are performed with GMR and spin transfer torque respectively, and the bit is stored in the chirality of the free layer vortex.

1.4 Overview

Ferromagnetism is an intricate physical state that is both fundamentally understood and persistently relevant. After the Pauli exclusion principle and identification of intrinsic electron spin in 1925, and Heisenberg's resultant exposition of the electrostatic exchange interaction in 1929, Dirac declared that the basic problems of solid state physics and chemistry were all understood in principle, if with "equations much too complicated to be soluble" [32]. But in the ensuing 86 years, "filling in the details has proved to be astonishingly rich and endlessly useful" [8]. This thesis aspires to expound the complexity, richness, and potential usefulness of magnetization dynamics in a chirality controlled dual-vortex spin valve nanopillar.

Chapters 2 and 4 introduce the salient physics of micromagnetics, a combined phenomenological theory and practical methodology for modelling ferromagnetic dynamics. Motivated by the development of bit patterned media, and generally thematic of contemporary solid state physics, we are interested in the effects of spatial confinement, surfaces, and interfaces. Chapter 2 connects these effects to the micromagnetic energies that describe equilibrium magnetization configurations. Specific cases of the magnetic vortex configuration in patterned elements and spin valves are explored in the first part of Chapter 3, followed by an introduction to giant magnetoresistance. The first part of Chapter 4 extends micromagnetics into the dynamic regime, introducing the Landau-Lifshitz-Gilbert equation of motion for magnetization under the influence of an applied field. Then, the essentials of spin transfer torque in a spin valve, the write complement to GMR's read, are discussed and integrated into the equation of motion. Chapter 5 then reviews the literature on magnetization dynamics in magnetic vortex systems, comparing various methods for vortex manipulation and their suitability for device integration.

Numerical simulation results and analysis thereof comprise Chapters 6, 7, and 8. In Chapter 6, a method of chirality control with spin transfer torque in a spin valve nanopillar system is presented. The method of excitation, its micromagnetic effects, and the influence of the spin valve geometry are discussed. Chapter 7 concerns the dynamic relaxation of the system after chirality switching, in which the formation and dissipation of spin wave eigenmodes plays a key role. These modes fundamentally differ from previously reported ones, and their features are contrasted with an existing model. To clarify the role of the interdependent energetic and geometric origins of the eigenmodes, Chapter 8 reports on frequency domain changes with relative chirality and variation of the thickness of the non-magnetic central layer of the spin valve. Both factors affect coupling between the magnetic layers. The chapter wraps up with visualizations of the dynamic stray field that mediates the interlayer coupling. Finally, the concluding Chapter 9 summarizes the findings of the thesis and gives potential directions for extensions to the research.

Chapter 2

Equilibrium micromagnetics

Vortices occur in correlated systems on all length scales: macroscopic and dynamic in tide pools and black hole accretion discs, microscopic and static as screw dislocations in crystals, and quantum mechanical, carrying quantized magnetic flux in type-II superconductors [33] and angular momentum in bosonic [34, 35] and fermionic [36] superfluids. A magnetic vortex is a nonuniform magnetization configuration in a ferromagnet that constitutes a stable ground state in some cases and emerges as a nonlinear excitation in others. Before a magnetic vortex was directly observed, it was established as a type of fundamental excitation in model systems, occurring even in the absence of magnetic dipolar interactions. For example, in a Heisenberg model of any dimension and anisotropy, the first anharmonic term in the Hamiltonian for the magnetization describes the two-magnon interaction and takes the form of an attractive delta-function potential. This mutual attraction of magnons in relatively high-lying states can lead to stable, spatially localized excitations called magnetic solitons [37]. Solitons that continuously deform to the ground state are called dynamic solitons and their dissipation is a key process in magnetization relaxation following a perturbation. These are common long-wavelength spin waves. The other kind of soliton is a

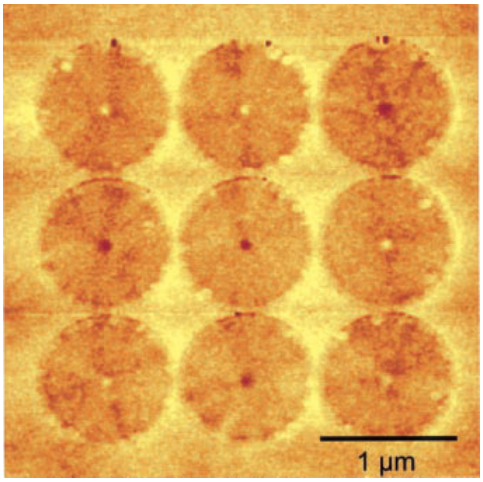

Figure 2.1: Magnetic force microscopy image of permalloy dots 1 µm in diameter and 50 nm thick. The light or dark contrast in the centre of each dot corresponds to up or down polarity of the magnetic vortex core. From Ref. [38].

topological soliton, an exemplary noncollinear magnetization configuration. These cannot be continuously transformed to recover a uniform ground state, and include domain walls and vortices.

When one or more physical dimensions is constrained, topological solitons adapt to the boundary conditions. In thin films, Bloch and Nèel domain walls form, differing in their orientation with respect to the film normal, and where they intersect, vortices and antivortices can be found. In patterned thin film wires and polygonal elements, more exotic domain wall structures can include vortices, antivortices, and fractional versions thereof, and in a disk-shaped element, a vortex forms in isolation. In each of these cases, the spatial confinement influences the topology.

Direct observation of magnetic vortices in NiFe disks was achieved in 2000 by magnetic force microscopy (MFM) (Figure 2.1, from Ref. [38]). Numerous groups confirmed the remanent vortex state and probed its dynamic properties with additional techniques, including Lorentz transmission electron microscopy [39, 40], spin-polarized scanning tunneling microscopy [41], magnetic transmission x-ray microscopy (MTXM) [42, 43, 44],

electron holography [45, 46], spin-resolved scanning electron microscopy [47], and time-resolved near-field scanning magneto-optical Kerr effect microscopy [48]. Modal analysis of time resolved Kerr effect (TR-MOKE) [49] and Brillouin light scattering (BLS) [50, 51] experiments further revealed the energetics of excitation and relaxation in these systems.

To contextualize these analytical and experimental findings, further understand the static and dynamic properties of isolated and coupled magnetic vortices, and assess the magnetic vortex as a candidate for memory applications, we first seek to compile a model for nanoscale ferromagnets. In this chapter, after a brief introduction to micromagnetism, the magnetic energies responsible for the emergence and evolution of magnetization configurations are enumerated and classified. Exchange interactions and demagnetization energy are described as competitive forces in confined magnetic structures, in preparation for the review of equilibrium magnetic disks and spin valves in Chapter 3. Then we write down the micromagnetic Hamiltonian and identify its fundamental nonlinearity.

2.1 Micromagnetic energies

Micromagnetism is the continuum phenomenological model built to investigate spatial and temporal evolution of magnetization configurations, and it underpins the numerical modeling presented in Chapters 6, 7, and 8. It is a patchwork semiclassical theory assembled from the Heisenberg model, for a quantum mechanical exchange interaction, classical electrodynamics, for the basic equations of magnetization, and solid state crystallographic and band structure effects. In order to describe ground state configurations as well as nonlinear magnetization dynamics, compare with analytical models, and provide insight into experimental results, the micromagnetic model and its implementation have regularly evolved over the last 50 years.

Ferromagnetism emerges in a second-order phase transition, a continuous transformation from a high temperature, disordered phase to a low temperature phase exhibiting order. The ordered system has reduced symmetry: the Hamiltonian that prescribed a unique vacuum in the disordered phase now allows degenerate, local free energy minima. The reduced symmetry and the strength of the breaking are described by an order parameter – for the ferromagnetic phase this is its spontaneous magnetization $\mathbf{M}$, the vector density of magnetic moments. Equilibrium magnetization states, called configurations as in statistical mechanical models, are found by minimization of the system's free energy.

Phases describe a macroscopic length scale in which ferromagnets are aggregates of domains. Micromagnetism on the other hand concerns the length scale from nanometers to microns, small enough to resolve magnetization inhomogeneities including domain walls and vortices, but computationally efficient enough, versus many-body atomistic approaches, to treat ferromagnets functional in the context of Chapter 1. For stability, fabrication, and topological reasons, we are interested in magnetic elements with in plane dimensions on the order of 100 nm and aspect ratio (out of plane thickness divided by in plane radius) less than 0.5. For micromagnetic calculations, we partition the volume region containing the element into a regular grid of nanometric cells, each of which contains a statistically large number of electrons. Each cell contains an elementary magnet, a composite moment that emerges from electronic correlation with both localized and conduction electrons participating. Assuming the moments are uniformly distributed and locally almost parallel (Section 2.1.1), the discrete moments $\mathbf{m}_i$ with positions $\mathbf{r}_i$ effectively comprise a continuous magnetization

$$\mathbf{M}(\mathbf{r}) \approx \frac{1}{V(\mathbf{r})} \sum_i \mathbf{m}_i(\mathbf{r}_i). \tag{2.1}$$

With a homogeneous density of constituent moments, $\mathbf{M}$ uniformly has magnitude M_s, the material property saturation magnetization. It is only defined inside the element,

and therefore discontinuous on the boundary. For the numerical calculations, $|\mathbf{M}|$ remaining constant constrains the boundary value problem. For convenience, we define the reduced magnetization $\mathbf{m} = \mathbf{M}/M_\mathrm{s}$, the unit vector field in the direction of $\mathbf{M}$.

The goal of this section is to formalize the interdependence of the micromagnetic energies and the magnetization itself. In general, an energy density due to a field $\mathbf{H}$ interacting with the magnetization has the form $E = -\int \mathbf{M} \cdot \mathbf{H}\, \mathrm{d}V$, and the effective field due to the magnetic energy E is

$$\mathbf{H} = -\frac{1}{M_\mathrm{s}} \frac{\delta E}{\delta \mathbf{m}}. \tag{2.2}$$

2.1.1 Exchange

The ultimate driving force for magnetic effects is the exchange interaction [52].

In metals the ground state electron density $n(\mathbf{r})$ determines the crystal structure, density, charge density, magnetic order, and susceptibility, and its low-energy excitations constitute transport phenomena [53]. In ferromagnets the electrons are further divided into majority (spin up, $\uparrow$) and minority (spin down, $\downarrow$) populations, according to the orientation of their magnetic moments parallel or antiparallel to the magnetization respectively, and the ground state $n^\uparrow \neq n^\downarrow$ is a product of electron correlation. Weiss postulated a causal mean field [8] that was later identified in the atomic limit by Heisenberg [54] and Dirac [32] as an exchange interaction.

Pauli's exclusion principle states that because a wavefunction of indistinguishable fermions must change sign under permutation, electrons with the same spin cannot occupy the same position. That is, since parallel spins are spin-symmetric on interchange, the wavefunction must be space-antisymmetric to satisfy the exclusion principle. Since electrons in an antisymmetric wavefunction are found further apart than electrons in a symmetric wavefunction, the antisymmetric state is lower in Coulomb energy, and the probability of

finding oppositely oriented spins close together is decreased relative to that of like spins. So although Coulomb repulsion is spin-independent, the Coulomb eigenenergies are spin-dependent. This intra-atomic exchange gives ferromagnetic ordering to, e.g., localized spins in a nickel atom [52]. The resulting polarization grants majority and minority electrons different characteristics, affecting transport properties in Sections 3.2.2 and 4.2.

Ferromagnetism also requires a specific band structure. In a metal, band paramagnetism is characterized by a small positive Pauli susceptibility χ_{P} proportional to the density of states at the Fermi level. Narrower bands have a higher susceptibility, and with a high enough density of states, the majority and minority bands spontaneously split and the metal becomes ferromagnetic. The Stoner model describes this splitting in a free electron electron gas with magnetization $M = (n^{\uparrow} - n^{\downarrow})\mu_{\mathrm{B}}$ and exchange energy $-(\mathcal{I}/4)(n^{\uparrow} - n^{\downarrow})^2$, where $\mathcal{I}$ is the Stoner exchange parameter that describes energy reduction due to correlation. The resulting susceptibility is $\chi = \chi_{\mathrm{P}}/(1 - n_{\mathrm{S}}\chi_{\mathrm{P}})$, where n_{S} is akin to the Weiss coefficient, measuring the contribution of the magnetization to the internal field. When $n_{\mathrm{S}}\chi_{\mathrm{P}} > 1$ this susceptibility diverges, corresponding to the Stoner criterion $\mathcal{I}n_{\uparrow,\downarrow}(E_{\mathrm{F}}) > 1$. For Fe, Co and Ni, $n_{\mathrm{S}} \approx 10^3$, $\mathcal{I} \approx 1.0$ eV is comparable to the bandwidth, and a narrow, high peak in the density of states proximal to the Fermi energy leads to spontaneous ferromagnetism.

In transition metal ferromagnets there is also interatomic exchange between spins on neighbouring atoms. This leads to the usual starting point for micromagnetics, the classical Heisenberg Hamiltonian

$$E_{\mathrm{exch}} = -\sum_{i,j} \mathcal{J}_{i,j}\mathbf{S}_i \cdot \mathbf{S}_j, \tag{2.3}$$

which describes an interaction that favours parallel spins. The exchange integral $\mathcal{J}_{i,j}$ is nonzero only for exchange coupled spins, usually nearest neighbours in a lattice model,

and $\mathcal{J} > 0$ corresponds to ferromagnetism. The equivalent micromagnetic exchange is an interaction between moments in adjacent cells:

$$E_{\text{exch}} = A \sum_i \mathbf{m}(\mathbf{r}) \cdot \mathbf{m}(\mathbf{r} + \Delta\mathbf{r}_i), \tag{2.4}$$

where $\Delta\mathbf{r}_i$ is the position vector between the cells, $i = \{x, y, z\}$, and A is the exchange constant. By the law of cosines,

$$\mathbf{m}(\mathbf{r}) \cdot \mathbf{m}(\mathbf{r} + \Delta\mathbf{r}_i) = 1 - \frac{1}{2}[\mathbf{m}(\mathbf{r}) - \mathbf{m}(\mathbf{r} + \Delta\mathbf{r}_i)]^2. \tag{2.5}$$

Taking $\mathbf{m}$ to be a continuous function, the distance vector $\mathbf{m}(\mathbf{r}) - \mathbf{m}(\mathbf{r} + \Delta\mathbf{r}_i)$ can be written $\Delta\mathbf{r}_i \cdot \boldsymbol{\nabla}\mathbf{m}$ [55]. With Equations 2.4 and 2.5, the total exchange energy is found by integrating over the magnetic element:

$$E_{\text{exch}} = A \int \sum_i |\boldsymbol{\nabla}\mathbf{m}_i|^2 \, \mathrm{d}V, \tag{2.6}$$

where we have dropped a constant of integration by convention. For computational reasons we require the effective exchange field via Equation 2.2:

$$\mathbf{H}_{\text{exch}} = -\frac{A}{M_{\text{s}}} \frac{\delta}{\delta\mathbf{m}} (\boldsymbol{\nabla}\mathbf{m})^2 = \frac{2A}{M_{\text{s}}} \boldsymbol{\nabla}^2\mathbf{m}. \tag{2.7}$$

E_{exch} is short range and contributes a Helmholtz free energy. It is minimal for parallel neighbouring spins and so favours a uniform magnetization configuration. Exchange is responsible for dynamically distributing the angular momentum of a spin flip over a collective spin wave, and maximizing the width of a domain wall by minimizing the angle between neighbouring spins in the wall. Also called exchange stiffness, A gives the strength of the interaction. It is a material property that depends on $\mathcal{J}$ and thus point group symmetry. The exchange length

$$l_{\text{ex}} = \sqrt{\frac{2A}{4\pi M_{\text{s}}^2}} \approx 5\text{nm} \tag{2.8}$$

is the characteristic length of the competition between exchange and magnetostatic interactions. (There are many alternative definitions of l_{ex}, not all equivalent [56, 50, 57, 58].) l_{ex} also sets the practical lower limit to miniaturizing isolated elements – reduction to about 1–2 exchange lengths in diameter approaches the superparamagnetic limit, wherein temperature fluctuations overwhelm the remanent magnetization (Section 1.1). Exchange between nearest neighbour spins is equivalent to a local field of order 100-1000 T [59]. Applied fields in this range, in theory, would diminish M_{s} due to spin-wave instabilities.

2.1.2 Magnetocrystalline anisotropy

Magnetocrystalline anisotropy energy E_{mxtal} is the tendency for magnetization to lie along certain crystal axes. It is attributed to spin-orbit interactions, equivalent to a field on the order of 0.1 T that is local on the scale of the Brillouin zone. E_{mxtal} is expressed as a power series in magnetization components with as many coefficients as necessary for the symmetry of the point group. Thus we typically speak of uniaxial anisotropies (point groups with a c-axis), cubic anisotropies (cubic systems), etc., each truncated in practice to second order. As throughout solid state phenomenology, deviations from the bulk occur at surfaces and interfaces, resulting in modified expressions for surface anisotropy. Intentional fabrication can result in polycrystalline microstructure with grain size $\approx l_{\mathrm{ex}}$, so anisotropic effects are suppressed by averaging over grains. For this reason, the anisotropy term is neglected from here on. This is consistent with the usual approximation, for the transition metals considered here, that the spin-orbit interaction is quenched by the strong hybridization of the d electrons [60]. (The free electron and transition ferromagnet g-factors differ by about 5–10%.) A full treatment of anisotropies would necessitate a tensor equation of motion with tensor damping [61, 62]. If the magnetic layers take on a texture during fabrication, the large uniaxial anisotropy of cobalt should be taken into account.

2.1.3 External fields

External fields $\mathbf{H}_{\text{ext}}$ contribute Zeeman energy via the Maxwellian interaction $E_{\text{ext}} = -\int \mathbf{M} \cdot \mathbf{H}_{\text{ext}} \, \mathrm{d}V$. E_{ext} is a minimum when $\mathbf{M}$ is uniformly parallel to $\mathbf{H}_{\text{ext}}$. The effect is long range and hysteretic. Typical applied fields are order 10–100 Oe to manipulate soft magnets and up to order 1 T in frequency domain experiments on hard magnets. For the reasons in Chapter 1, we are not interested in external applied fields, but the Oersted field generated by an applied current with density $\mathbf{J}$

$$\boldsymbol{\nabla} \times \mathbf{H}_{\text{ext}} = \mathbf{J} \tag{2.9}$$

does contribute via this term.

2.1.4 Demagnetization

The magnetostatic self energy of the system measures the interaction of the magnetization with its own stray field. The dipole field in the cell at $\mathbf{r}$ due to the moments in every other cell is [63]

$$\mathbf{H}(\mathbf{r}) = \frac{1}{4\pi} \sum_{\mathbf{r}' \neq \mathbf{r}} \left\{ \frac{3[\mathbf{m}(\mathbf{r}') \cdot (\mathbf{r} - \mathbf{r}')] \cdot (\mathbf{r} - \mathbf{r}')}{|\mathbf{r} - \mathbf{r}'|^5} - \frac{\mathbf{m}(\mathbf{r}')}{|\mathbf{r} - \mathbf{r}'|^3} \right\}. \tag{2.10}$$

This can be rewritten in terms of a continuous magnetization using classical magnetostatics. In the absence of applied currents the field $\mathbf{H}$ is curl free, $\boldsymbol{\nabla} \times \mathbf{H} = 0$, and $\boldsymbol{\nabla} \cdot \mathbf{B} = 0$. Thus $\mathbf{H}$ is equal to the gradient of a scalar magnetic potential u,

$$\mathbf{H} = -\boldsymbol{\nabla} u, \tag{2.11}$$

due to sources $\boldsymbol{\nabla} \cdot \mathbf{M}$, yielding the Poisson equation

$$\nabla^2 u = \boldsymbol{\nabla} \cdot \mathbf{M}. \tag{2.12}$$

Since $\mathbf{M}$ is bounded by the element, $u(\mathbf{r}) \to 0$ as $\mathbf{r} \to \infty$. Using this so-called open boundary condition, equation 2.12 is solved using the Green's function of the Laplace operator $-1/(4\pi|\mathbf{r}-\mathbf{r}'|)$ [64]:

$$u(\mathbf{r}) = -\frac{1}{4\pi}\int \frac{\boldsymbol{\nabla}' \cdot \mathbf{M}(\mathbf{r}')}{|\mathbf{r}-\mathbf{r}'|}\,\mathrm{d}V'. \tag{2.13}$$

Using Gauss's law and invoking the localization of $\mathbf{M}$ results in the simplified form

$$u(\mathbf{r}) = \frac{1}{4\pi}\int \mathbf{M}(\mathbf{r}') \cdot \boldsymbol{\nabla}' \frac{1}{|\mathbf{r}-\mathbf{r}'|}\,\mathrm{d}V'. \tag{2.14}$$

Finite difference methods simplify solving equations 2.11 and 2.14. Since the magnetization within a cell is uniform, the potential due to $\mathbf{M}'$ in a cell with volume V' is

$$u(\mathbf{r}) = \frac{1}{4\pi}\mathbf{M}' \cdot \int \boldsymbol{\nabla}' \frac{1}{|\mathbf{r}-\mathbf{r}'|}\,\mathrm{d}V'. \tag{2.15}$$

A second cell in volume V experiences an average field $\mathbf{H}'$ due to this potential that can be expressed in terms of a demagnetizing tensor [65, 66],

$$\langle \mathbf{H}'(\mathbf{r}) \rangle_V = -\boldsymbol{\nabla} u(\mathbf{r}) = -\int \mathsf{N}(\mathbf{r}-\mathbf{r}')\mathbf{M}'(\mathbf{r}')\,\mathrm{d}V, \tag{2.16}$$

where

$$\mathsf{N}(\mathbf{r}-\mathbf{r}') = -\frac{1}{4\pi}\boldsymbol{\nabla}\boldsymbol{\nabla}' \frac{1}{|\mathbf{r}-\mathbf{r}'|} \tag{2.17}$$

is a 3×3 matrix in every cell. For cuboid cells

$$\mathsf{N}(\mathbf{r}-\mathbf{r}') = -\frac{1}{4\pi V}\int \mathrm{d}V\, \boldsymbol{\nabla} \int \boldsymbol{\nabla}' \frac{1}{|\mathbf{r}-\mathbf{r}'|} dV', \tag{2.18}$$

and Equation 2.16 has an analytical solution [67, 66]. The demagnetization field at each grid point is calculated via convolution:

$$\mathbf{H}_\mathrm{m}(\mathbf{r}) = -\sum \mathsf{N}(\mathbf{r}-\mathbf{r}')\mathbf{M}'(\mathbf{r}') = -\mathcal{F}^{-1}[\mathcal{F}(\mathsf{N}) \cdot \mathcal{F}(\mathbf{M})]. \tag{2.19}$$

This is the strategy employed by most finite difference micromagnetic packages.

An alternate approach from Ref. [68] is used to calculate the stray field outside the sample in Chapter 8. Equation 2.16 can be rewritten in terms of an auxiliary vector field:

$$\mathbf{H}(\mathbf{r}) = -\boldsymbol{\nabla} u = -\boldsymbol{\nabla} \int \mathbf{S}(\mathbf{r}-\mathbf{r}')\mathbf{M}(\mathbf{r}')\,\mathrm{d}V'. \tag{2.20}$$

On a finite difference grid,

$$\mathbf{S}(\mathbf{r}-\mathbf{r}') = \frac{1}{4\pi}\int \boldsymbol{\nabla}' \frac{1}{|\mathbf{r}-\mathbf{r}'|}\,\mathrm{d}V', \tag{2.21}$$

and the scalar potential of the stray field is

$$u(\mathbf{r}) = \sum \mathbf{S}(\mathbf{r}-\mathbf{r}')\mathbf{M}'(\mathbf{r}') = -\mathcal{F}^{-1}[\mathcal{F}(\mathbf{S})\cdot\mathcal{F}(\mathbf{M})]. \tag{2.22}$$

By calculating the scalar potential of the stray field first, the Fourier space tensor-vector multiplication in Equation 2.19 is simplified to a vector-vector operation. This reduces the number of arithmetic operations, the number of inverse Fourier transforms, and the memory consumption of the numerical stray field calculation [68].

Magnetostatic self energy $E_{\mathrm{dem}} = -\frac{1}{2}\int \mathbf{M}\cdot\mathbf{H}_{\mathrm{m}}\,\mathrm{d}V$ is long range and minimized by suppressing the formation of volume ($\boldsymbol{\nabla}\cdot\mathbf{M}$) and surface ($\mathbf{M}\cdot\hat{\mathbf{n}}$) charges. The tendency of $\mathbf{H}_{\mathrm{m}}$ to diminish the overall magnetic moment of the system by rearranging the magnetization gives it the common name demagnetizing field and the associated energy demagnetizing energy. The first direct probe of surface magnetization configurations was mapping the stray field generated by $\mathbf{M}\cdot\hat{\mathbf{n}}$ with fine magnetic particles; techniques such as hall probe microscopy [69], SQUID magnetometry, and magnetic force microscopy [70] are contemporary equivalents. The local demagnetization field strength inside a thin film element is of order 1 T, and it falls off as the cube of the distance outside.

Demagnetization acts to align $\mathbf{M}$ tangent to surfaces, driving the formation of nonuniform configurations inside ferromagnetic elements. It competes with exchange, which

uninhibited would relax $\mathbf{M}$ into a solenoidal configuration with costly, in terms of demagnetization energy, surface poles. This competition strongly influences equilibrium and nonequilbrium magnetization configurations, and the consequently nontrivial ground states are the initial conditions for magnetization dynamics.

2.2 Micromagnetic Hamiltonian

The micromagnetic Hamiltonian for internal ferromagnetic energy used in this thesis is, with terms in order of characteristic length, is

$$E_{\text{tot}} = E_{\text{exch}} + E_{\text{dem}} + E_{\text{ext}} \tag{2.23}$$

The effective field acting on the magnetization consists of the effective exchange field (Equation 2.7) and the classical magnetostatic fields $\mathbf{H}_{\text{m}}$ (Equation 2.19) and $\mathbf{H}_{\text{ext}}$ (Equation 2.9). The resulting total system energy (Equation 2.23) and effective field (Equation 2.2) are interdependent:

$$E_{\text{tot}} = E_{\text{exch}} + E_{\text{dem}} + E_{\text{ext}} = -\int \mathbf{H}_{\text{eff}}(\mathbf{r}) \cdot \mathbf{M}(\mathbf{r}) \, \mathrm{d}V. \tag{2.24}$$

In the next chapter, we consider the case $\mathbf{H}_{\text{ext}} = 0$ in thin films and isolated and vertically coupled magnetic disks.

Chapter 3

Vortices in disks and spin valves at equilibrium

We have previously discussed the prevalence of the magnetic vortex state (the introduction to Chapter 2) and its potentially useful static properties (Section 1.3). With this context, the present chapter first builds on the descriptions of exchange (Section 2.1.1) and demagnetization (Section 2.1.4) with a review of common magnetization configurations in disk-shaped magnetic structures. Then, a classic micromagnetic problem demonstrates typical approximations and common representations of the vortex magnetization. This treatment previews the dynamical cases outlined in Section 5.3. The second part of this chapter reviews the static properties of spin valves. First, configurations in the magnetic layers of a spin valve are shown to be modified by interlayer coupling. Second, the physical basis for giant magnetoresistance and the related approximations used in the micromagnetic model are discussed.

3.1 Disk systems and topology

Configurations in patterned thin film structures with negligible magnetocrystalline anisotropy reflect their spatial confinement. Demagnetization causes the magnetization to lie in plane and tangent to edges. Exchange between adjacent moments translates the alignment of the edge magnetization inward from the edges with gradual and smooth variation, inducing vorticity or curling of the magnetization about the center or foci of a polygonal or elliptical element. If a vortex is formed, the exchange stiffness of the media competes with the demagnetization field to determine the core diameter – typically about twice the exchange length. Therefore the micromagnetic stability of the vortex configuration is a combined geometric and material property.

3.1.1 Configurations

In real cylindrical samples, equilibrium states range from quasiuniform to essentially nonuniform. Deviations from the uniform single domain configuration are driven by the competition of demagnetization (magnetization tangent to boundaries) and exchange (maximum uniformity) energies. Figure 3.1, from Ref. [71], presents six equilibrium states found in submicron $Ni_{80}Fe_{20}$ disks with varying aspect ratios. Planar onion, C, and S states (a, e, and f) and the out of plane vortex (b) are most prevalent in thin film disks [72]. Each configuration is labeled with its spread function ($0 \leq \mathrm{SF} < 1$), a scalar measure of nonuniformity and proxy for total exchange energy. Of these states, the onion is the exchange minimum but also the demagnetization maximum. The C and S states show first- and second-order buckling, increasing in exchange energy but decreasing in demagnetization energy. The latter is evident in terms of the stray field – the edge poles have decreasing pitch and so flux closure outside the element occurs along successively shorter paths. Finally, the vortex state has the highest exchange energy but no poles at the radial boundary and rela-

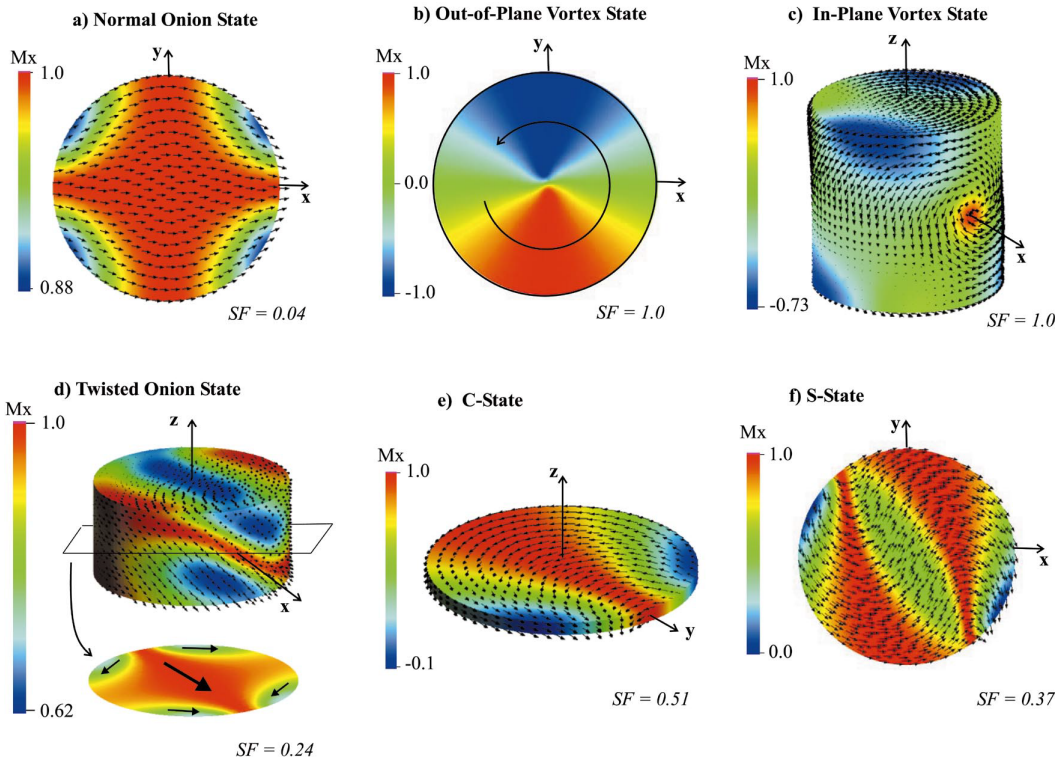

Figure 3.1: Equilibrium states of an isolated disk. Onion, C, S, and vortex states are most common. The spread function *SF* is a measure of the nonuniformity. From Ref. [71].

tively short stray field lines connecting the vortex core to its oppositely polarized halo (not shown). In any case, the ground state is a local energy minimum and its configurational stability strongly influences the systemic response to excitation (Chapter 5).

By adjusting the aspect ratio and minimizing the energy, one can identify the limits to the vortex configuration for a given material. Boundaries between phases are not rigid, rather configurations are local minima and there is overlap. The room temperature relaxation process, during fabrication or after excitation, is both stochastic and hysteretic. Experiments typically employ an external field or other impetus to ensure a certain starting configuration.

An ideal vortex is specified by two boolean topological indices: counterclockwise

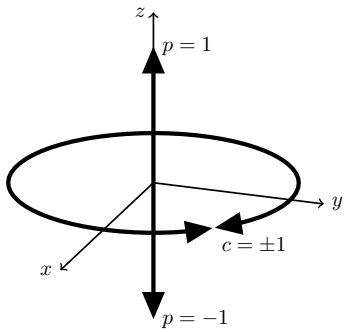

Figure 3.2: Vortex chirality and polarity.

or clockwise chirality $c = \pm 1$ and up or down polarity $p = \pm 1$, shown schematically in Figure 3.2. These are binary labels that do not strictly apply to real confined systems. Alternatives are the spread factor depicted in Figure 3.1, vorticity, a continuum measure of curl in a system related to the winding number, and the discrete chirality

$$c = \frac{1}{N} \sum_i \mathbf{m}_i \cdot \hat{\boldsymbol{\phi}}_i, \tag{3.1}$$

where $\hat{\boldsymbol{\phi}}$ is the azimuthal unit vector in disk coordinates (N is the number of cells) [73]. A third dimension adds further complexity. Disks with low aspect ratio and thickness less than about 2–3 times the exchange length have a cylindrical vortex core. In thicker disks, the vortex diameter is smaller at the surfaces in order to reduce demagnetization energy and balloons about its vertical center to reduce the exchange cost of a tightly wound core. The magnetic layers in Chapters 6, 7, and 8 obey the former condition and the configurations are assumed uniform through their thickness.

Two additional features of vortex configurations are worth noting. First, there is often a dip that circumscribes the vortex core due to its dipole field, oriented opposite the core polarity. Its shape and stability become critically important during translational mode vortex core dynamics (Section 5.1). Second, the edge magnetization can be tilted at equilibrium, also opposite the core polarization, for large aspect ratio, small radius, or due

to the influence of another vortex. The dip is a feature in a few ansatzes used for finding the ground state, the edge deviation as a rule is not; both features play roles in Sections 5.3 and 6.2.

3.1.2 Bloch points

A Bloch point is a volume singularity in a ferromagnet. Whereas for an ideal vortex the magnetization vectors on a closed loop about core map to the unit hemisphere, in a Bloch point the magnetization vectors measured on a closed surface about the Bloch point map to the unit sphere [74]. Bloch points come in several configurations, including a monopole form which resembles the radially diverging field of a point charge; an axial form where the magnetization curls around the azimuth like a vortex but the core has both polarities, resembling two vortices with opposite polarity stacked atop one another; and an axial antivortex-like form where the magnetization points radially in along the equator and up and down along the axis. Ref. [74] measured a 10 nm radius for a Bloch point by way of micromagnetic simulations with a variable mesh, on the order of a vortex core radius and approximately twice a soft magnet exchange length, and also calculated the micromagnetic energy of a Bloch point. Bloch points arise in Section 5.1.2 in regards to vortex dynamics.

3.1.3 Analytical models

Analytic micromagnetics gives additional insight into the static energetics of vortices. The general prescription was first used by Feldtkeller and Thomas to calculate the core radius of a vortex in a Bloch line, a type of domain wall containing sequential vortices and antivortices [75]. Cylindrical coordinates $\mathbf{r} = (\rho, \phi, z)$ are used, coaxial with an integration volume of thickness L and radius R centered on the vortex. Since the length of magnetization is constant, the spherical-basis magnetization reduces to $\mathbf{m} = (\Theta, \Phi)$.

The ground state is found by minimizing the Landau-Lifshitz free energy functional. With exchange and magnetostatic terms, Equation 2.24 takes the form

$$E_{\text{tot}} = \int \left[A(\boldsymbol{\nabla}\mathbf{m})^2 - \frac{1}{2}\mathbf{H}_{\text{m}} \cdot \mathbf{m} \right] \mathrm{d}V. \tag{3.2}$$

The exchange term simplifies to

$$E_{\text{exch}} = 2\pi AL \int_0^R \left[\left(\frac{d\Theta}{d\rho} \right)^2 + \frac{\sin\Theta}{\rho^2} \right] \rho \, \mathrm{d}\rho, \tag{3.3}$$

which first appeared in [76]. Next, an expression for $\mathbf{H}_{\text{m}}$ is needed. At minimum, $\mathbf{H}_{\text{m}} = -\nabla u$, $\nabla^2 u = \boldsymbol{\nabla} \cdot \mathbf{M}$, and the sources $\boldsymbol{\nabla} \cdot \mathbf{M}$ are just the top and bottom surface charges due to the vortex core.

Both the demagnetization and exchange terms require an ansatz for the magnetization. There is no radial magnetization component in an ideal vortex, so $m_\rho = 0$. The remaining components are complementary: $m_\phi = 0$ where $m_z = 1$, at the vortex core, and vice versa outside the core. In terms of the polar angle Θ,

$$\mathbf{m} = (m_\rho, m_\phi, m_z) = [0, \sin\Theta(\rho), \cos\Theta(\rho)]\,. \tag{3.4}$$

With this ansatz, the demagnetization term can be simplified using Bessel functions to

$$E_{\text{dem}} = \pi \int_0^\infty (1 - e^{-\alpha L}) \left[\int_0^\infty \rho \cos\Theta(\rho) J_0(\alpha\rho) d\rho \right]^2 d\alpha. \tag{3.5}$$

Fedltkeller and Thomas chose the ansatz $\Theta(\rho) = \arccos e^{-2\beta^2\rho^2}$, with β a variational parameter. Substituting the relevant equations into Equation 3.2, they found a vortex (Bloch line) radius of 6.6 nm.

Using this method, the single vortex ground state of an isolated magnetic particle was predicted by Aharoni, who studied the upper spatial limit for the uniform configuration [79]. Usov and Peschany and others refined the treatment and suggested various ansatzes for the vortex configuration, some of which include the dip surrounding the vortex

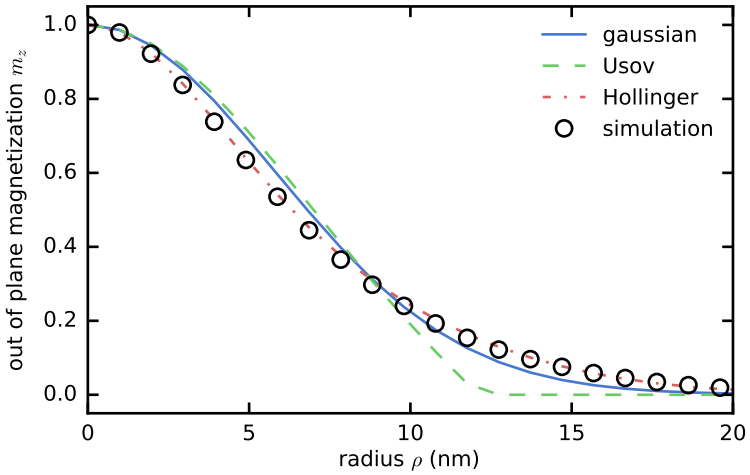

Figure 3.3: Common ansatzes for m_z compared to minimization of Equation 2.24.

	Notation	Value (nm)	Ref.
gaussian	σ_x	5.83	—
Usov	a	12.12	[56]
Hollinger	R_{eff}	7.70	[77]
Metlov	R_{V}	12.02	[78]
exchange length	l_{ex}	5.11	Equation 2.8

Table 3.1: Characteristic lengths of the vortex core.

core [56, 77]. Figure 3.3 shows $m_z(\rho)$ for the gaussian, Usov, and Hollinger ansatzes and micromagnetic simulation of a 5 nm-thick $Ni_{80}Fe_{20}$ disk with 50 nm radius. Note that the ρ axis is truncated to allow for more detail in the core region. The Usov and gaussian curves are fits to the simulation data, the Hollinger ansatz is a function of only radius, the exchange length, and the disk thickness. Table 3.1 compares the core radius from each of these ansatzes to the analytical solution of Metlov and the exchange length in $Ni_{80}Fe_{20}$. We generally use a 2D gaussian fit for analysis, as it provides not only two orthogonal radii but

also the core position, rotation, and m_z offset.

Analytical approaches to vortex dynamics follow a similar method, starting with Equation 3.2 and an ansatz for the magnetization. In the ground state for first-order calculations of spin wave eigenmodes, only the limits on $\Theta(\rho)$ are important:

$$\begin{aligned} \cos\Theta &\to p \ \text{ as } \ \rho \to 0 \\ \Theta &\to \pi/2 \ \text{ as } \ \rho \to R. \end{aligned} \tag{3.6}$$

There are relatively few ansatzes that yield closed-formed expressions for the demagnetization energy, all of which exclude a radial magnetization component. Further simplifications are also required for dynamic calculations; for example, in most cases the vortex core is assumed to not participate in the dynamics despite contributing the majority of the static demagnetization energy. These approximations and limitations are discussed in Section 5.3 in a discussion of spin wave eigenmodes and Chapter 7 in a comparison of dynamic micromagnetic calculations and the predictions of a recent analytical vortex model.

3.2 Spin valves

Coupled solitons can occur naturally in a single element, such as an ellipse, and likewise solitons can couple between proximal elements via their stray field, or, particularly if the separation distance is less than the exchange length and spans a nonmagnetic intermediary, some form of exchange coupling. In plane coupling between two or more disks has been studied extensively, for vortex and other configurations [80, 81]. Out of plane coupling, with more complicated requirements for fabrication and magnetization detection, has also received considerable attention [82, 83]. Spin valve nanopillars naturally exhibit the latter (Section 2.1.4), and this section begins with a brief account of the effects of vertical coupling on the overall magnetic configuration. The geometry and relative magnetization of a spin

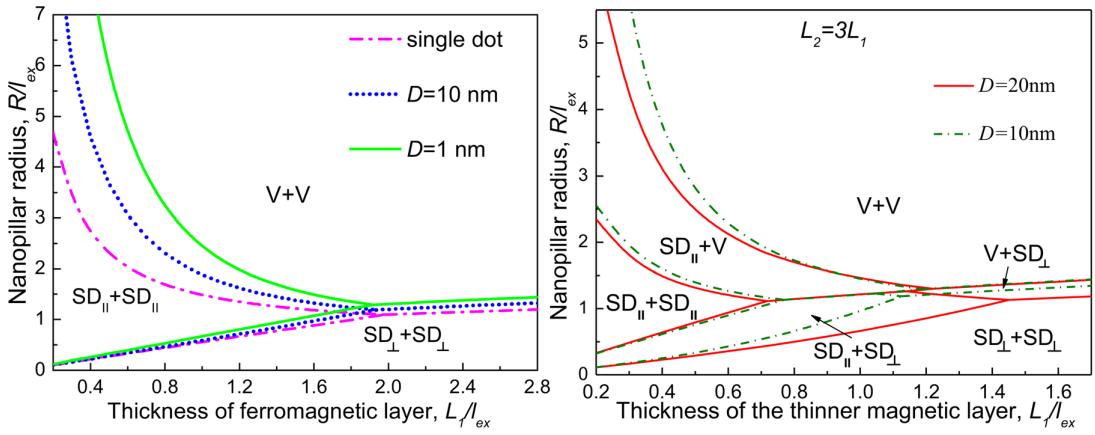

Figure 3.4: Aspect ratio phase diagram for symmetric (left panel) and asymmetric (right) circular spin valve nanopillars. From Ref. [84].

valve are also reflected in its transport properties, and we conclude with an overview of giant magnetoresistance.

3.2.1 Configurations

Spin valves are trilayer structures with ferromagnetic layers sandwiching a non-magnetic metallic spacer layer. With in plane dimensions patterned on a submicron scale, they form nanopillars. If the magnetic layer thicknesses or materials differ, the spin valve nanopillar is said to be asymmetric, with the magnetically harder layer called fixed and the other free (Section 1.3). Aspect ratio phase diagrams for circular spin valve nanopillars from Ref. [84] are shown in Figure 3.4. For different combinations of materials, aspect ratios, and spacer thickness, vortex (V), planar uniform ($SD_{\parallel}$), and perpendicular uniform ($SD_{\perp}$) configurations in the ferromagnetic layers are all stable states. The overall pillar configuration can be labeled by the configuration of its fixed and free layers: V+V (vortex-vortex), $V+SD_{\parallel}$ (vortex-single domain planar), etc. [84].

The second disc in the system alters the configuration phase diagram from that of an isolated disk. Whereas a planar single domain configuration in an isolated disk has edge

poles and a bar magnet-like stray field, a pair of single domains stacked vertically can assume antiparallel alignment with a flux-closed stray field, stabilizing each disk's configuration. The energy of the system then depends on the spacer layer thickness. This effect is evident for the symmetric nanopillar phase diagram (left panel of Figure 3.4): it has three stable states, each with like configurations in the top and bottom magnetic layers, and the SD+$SD_{\parallel}$ configuration is stabilized compared to the $SD_{\parallel}$ configuration of an isolated dot (here D is the spacer layer thickness). With asymmetry (right panel) there are six stable states. In each case the spacer thickness and the ratio of magnetic layer thicknesses both contribute to the location of the phase boundaries.

Two results of this study are important to our development. First, the asymmetric pillar that is the subject of Chapters 6, 7, and 8 is firmly in the V+V region of the phase diagram, vital for repeatable dynamics. Second, interlayer coupling between magnetic layers affects the magnetizations. For example, in a V+$SD_{\parallel}$ pillar the vortex core is displaced by the stray field of the other disk. In our case, significant modification of the equilibrium vortices in a V+V pillar, not reported in Ref. [84], plays a key role in Chapter 6.

3.2.2 Giant magnetoresistance

Interlayer exchange coupling (IEC) was discovered in a trio of 1986 experiments as antiferromagnetic coupling between the sequential ferromagnetic layers of Fe/Cr/Fe trilayers and rare earth-yttrium multilayers [85, 86, 87]. It was later demonstrated that the exchange coupling J oscillated with the thickness of the nonmagnetic spacer layer, so it could be tailored antiferromagnetic or ferromagnetic through fabrication [88]. IEC has subsequently been observed in numerous other layered transition metal [89] and transition ferromagnet-noble metal systems [90], and in sputtered polycrystalline films [88] alongside the epitaxial. On application of a sufficient magnetic field, the iron layer moments in the

Fe/Cr system were found to rotate into a parallel configuration, and the resulting large drop in the electrical resistance of the system was named giant magnetoresistance (GMR) [91]. The advances in fabrication that allowed for such delicate control over film thickness, and the elucidation of IEC and GMR, were followed by increasingly accessible methods for patterning, defining the in-plane dimensions of samples. The GMR property of the trilayer system earned it the moniker spin valve, and variously patterned spin valves have become the workhorses of magnetoelectronics.

GMR is also evident in a trilayer or multilayer without antiferromagnetic IEC when successive ferromagnetic layers have different coercivities. Such a spin valve in a low-resistance parallel configuration, having been subject to a saturating field, can be switched to a high-resistance, antiparallel configuration by cycling the field to between the coercive fields of the two magnetic layers. One usually maximizes the higher coercive field by using a relatively thicker or harder or exchange pinned fixed layer, so that only the other free layer can rotate with the applied field. Spin valves without absolute pinning, like the ones in this thesis, are sometimes referred to as pseudo or quasi-spin valves [92, 93]. In time-dependent measurements, the configuration-modulated magnetoresistance serves as an indirect probe of magnetization dynamics.

The GMR effect in a spin valve is shown schematically in Figure 3.5. The left panel represents a trilayer with an antiparallel ground state and its resistance and magnetic configuration during a field cycle. On the right is a trilayer with spacer layer thickness sufficient to suppress IEC and higher (lower) coercivity in the bottom (top) layer. The resistance change in each case is the hallmark of GMR. On the left, the magnetization rotation is continuous and $\mathcal{R}$ changes gradually with $\mathbf{H}$ as the field rotates the free layer magnetization, reaching minima at the saturating field $\pm H_{\mathrm{s}}$. In contrast, the right panel shows abrupt changes in resistance at the coercive fields of the top and bottom layers, as

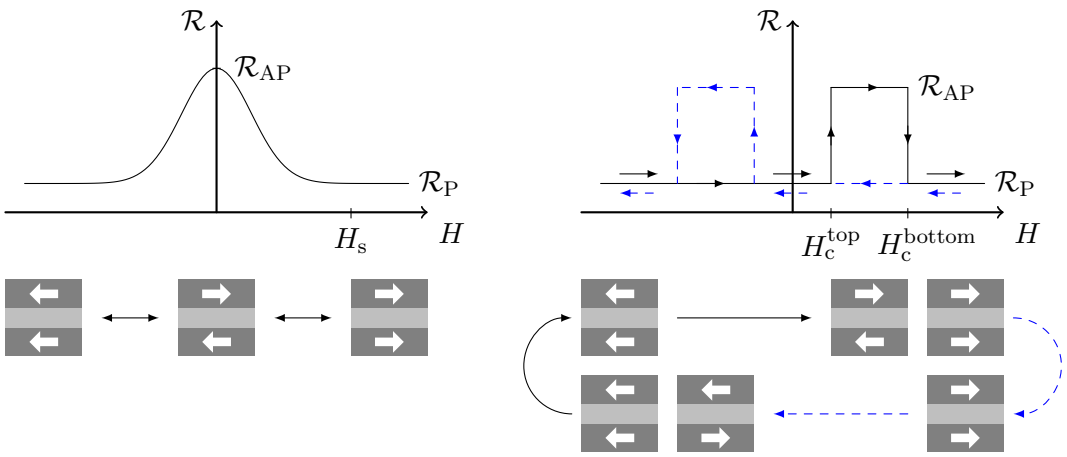

Figure 3.5: Giant magnetoresistance. (a) Resistance as a function of applied field in an extended thin film system with an antiparallel (AP) ground state. (b) A confined system with a parallel (P) ground state and effective uniaxial anisotropy. (Bottom panels) Configurations during field cycles, non-hysteretic and hysteretic respectively. Adapted from Ref. [94]

in bistable spin valve nanowires. Two-level behavior is characteristic of hysteresis, in which the history of the magnetic configuration is important. If the current is applied in the plane of the sample, parallel to the layers, the phenomenon is current in plane (CIP) GMR, while current normal to the layers is current perpendicular to plane (CPP) GMR. Discovery of the former preceded the latter for experimental reasons. CPP GMR is larger than CIP in identical systems and advantageous for device applications [95].

GMR is essentially due to spin dependent scattering, and the semiclassical Mott model of transition metal resistivity gives a sufficient explanation for micromagnetics. The electrons are divided into minority and majority populations depending the relative orientation of their spin and the magnetization (Section 2.1.1), and the majority and minority spin channels conduct in parallel. This is a good approximation when spin-flip scattering events, which couple the two channels, are few in comparison with spin-conserving processes. Scattering is assumed to be spin dependent, and since the spin channels do not mix, resistivity in the relaxation time approximation is different for majority and minority spins.

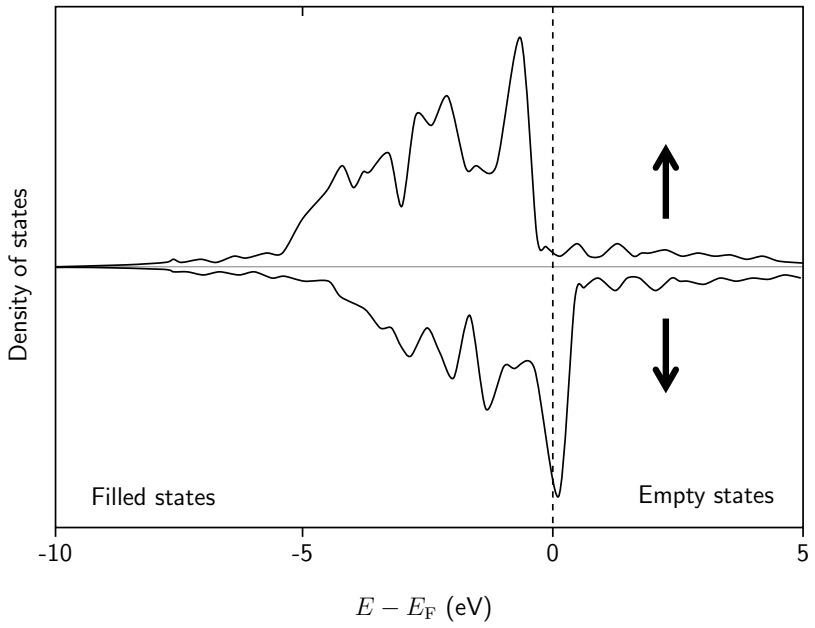

Figure 3.6: Cartoon density of states for majority and minority electrons.

This is generally true of exchange-split band structures.

Figure 3.6 shows an example majority and minority density of states having the features described in Section 2.1.1. For each channel, the Drude conductivity $\sigma \propto k_{\mathrm{F}}^2 \lambda_e$, where k_F is the spin dependent Fermi wave vector and $\lambda_{\mathrm{e}} = (\hbar k_{\mathrm{F}}/m_{\mathrm{e}})\tau$ is the mean free path of an electron with relaxation time τ (m_{e} is the electron mass). Due to the exchange interaction, the spin up band is shifted to a lower energy relative to the spin down band, resulting in a higher density of states for the spin down band at the Fermi energy (dashed line in Figure 3.6).

Fermi's golden rule gives us a scattering probability rate for each spin channel,

$$\tau^{-1} = \frac{2\pi}{\hbar} \left\langle V_{\mathrm{scat}}^2 \right\rangle n(E_{\mathrm{F}}),$$

where V_{scat} is the scattering potential. This equation indicates that the scattering probability for a conduction electron is proportional to the density of states at the Fermi energy $n(E_{\mathrm{F}})$. On inspection of Figure 3.6, since spin is assumed to be conserved on scattering,

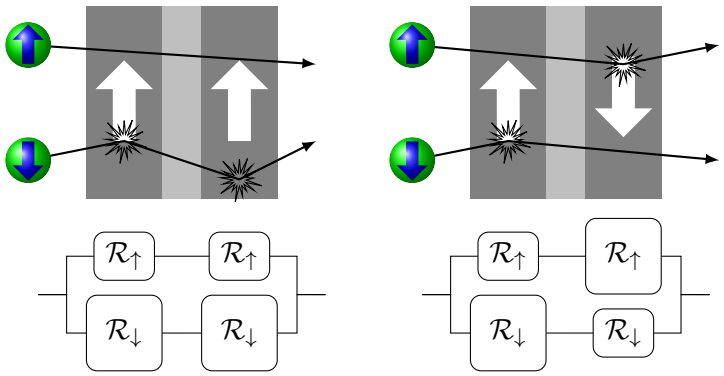

Figure 3.7: Configuration dependent scattering and circuit diagram for the two current model. Adapted from Ref. [94].

a spin up electron has relatively few states to scatter into and therefore a low resistivity. The spin down electrons have a higher $n(E_\mathrm{F})$ and therefore a shorter relaxation time and a higher resistivity [96].

While σ, k_F, and $n(E_\mathrm{F})$ are spin dependent material properties, V_scat is not an instrinsic property of the metal. Contributions to it are often but not always spin-dependent. Magnetic impurities, such as iron in a nickel rich alloy, are generally spin dependent scatterers. Phonons and defects including voids, interdiffused impurities near interfaces, stacking faults, and grain boundaries might carry spin dependence, but are individually opaque from an experimental standpoint. In practice, their inhomogeneity means that their contribution is rendered spin-independent by configurational averaging of V_scat. What persists is that spin dependent band structure largely determines λ_e and σ.

In summary, electrons are weakly scattered when their spin is parallel to the magnetization, and strongly scattered when it is antiparallel. As a result, in a GMR system with all parallel magnetizations, one spin channel is scattered strongly in every ferromagnetic layer while the other sees an effective short circuit. The shorted channel is highly conductive and the overall resistance in the multilayer is low. Conversely, the system with alternating moments scatters each spin channel strongly in turn, and the overall resistance

is high. These two cases are shown schematically in Figure 3.7 with a simple resistor model for parallel spin channels. More resistors can be added to the circuit too, such as contact resistances, where the current sources and sinks, and spin dependent resistances at the interfaces. Interface contributions are extensive [88], including (spin dependent) potential steps at interfaces and (possibly spin dependent) interface disorder, but accurate inclusion of them goes beyond the resistor model. In this thesis, the simple resistor model is adequate: the model band structure is representative of the transition metals used, d is not so thick as to invite channel mixing spin diffusion, the samples modeled are polycrystalline and so grain boundary scattering is present, and interface disorder through interdiffusion is probable.

For a given system, the magnetoresistance ratio is given by

$$\frac{\Delta\mathcal{R}}{\mathcal{R}} = \frac{\mathcal{R}_{\mathrm{AP}} - \mathcal{R}_{\mathrm{P}}}{\mathcal{R}_{\mathrm{P}}} \tag{3.7}$$

where AP (P) is the antiparallel (parallel) configuration. (There are other common definitions of $\Delta\mathcal{R}/\mathcal{R}$.) It has also been shown that GMR varies linearly with the cosine of the angle between the magnetizations in a spin valve [97, 94]:

$$\mathcal{R}(\theta) = \mathcal{R}_{\mathrm{P}} + \frac{1}{2}(\mathcal{R}_{\mathrm{AP}} - \mathcal{R}_{\mathrm{P}})(1 - \cos\theta). \tag{3.8}$$

A small radius dual vortex spin valve has an approximately 30% lower magnetoresistance ratio than a dual single domain configuration due to the parallel orientation of the cores. The nominal resistances presented in this thesis are approximations that underestimate real world values by neglecting disorder, thermal effects, and the resistance of leads. For comparison, simulated resistances are around 200 mΩ, and a well-fabricated spin valve with leads measures a few ohms in the lab.

Chapter 4

Magnetization dynamics

In this chapter we extend the micromagnetics of Chapter 2 to the dynamic regime. To model the time-dependent response of the spin valve nanopillar system, we use an equation of motion for magnetization under the influence of a dynamic effective field. The origin and micromagnetic approximation of magnetic damping are discussed. Spin transfer torque is integrated into the equation of motion.

4.1 Magnetization equation of motion

The spin magnetic moment of an electon is

$$\boldsymbol{\mu} = -\frac{g\mu_{\mathrm{B}}}{\hbar}\mathbf{s}, \tag{4.1}$$

where $g \approx 2$, μ_{B} is the Bohr magneton, and $\mathbf{s}$ is the spin of the electron. The dissipationless classical Hamiltonian $H = -\boldsymbol{\mu} \cdot \mathbf{h}$ describes a field $\mathbf{h}$ exerting a torque on the moment and changing its angular momentum, inducing Larmor precession of the moment about the field. Landau and Lifshitz predicted the ferromagnetic resonance of this precession and introduced a corresponding phenomenological equation for precession of the magnetization, which has

since been substantiated with classical, statistical mechanical, and quantum mechanical derivations.

In the Heisenberg picture, the time dependence of the spin vector $\hat{\mathbf{S}} = (\hat{S}_x, \hat{S}_y, \hat{S}_z)$ is

$$\frac{\mathrm{d}\hat{\mathbf{S}}}{\mathrm{d}t} = \frac{1}{i\hbar}\left[\hat{\mathbf{S}}, \hat{\mathbf{H}}\right]. \tag{4.2}$$

Using the commutator of spins $[\hat{S}_i, \hat{S}_j] = i\epsilon_{ijk}\hat{S}_k$ it has been shown that [98, 99]

$$\frac{1}{i\hbar}\left[\hat{\mathbf{S}}, \hat{\mathbf{H}}\right] = \hat{\mathbf{S}} \times \frac{\partial \hat{\mathbf{H}}}{\partial \hat{\mathbf{S}}} + \mathcal{O}(\hbar). \tag{4.3}$$

In the classical limit $\hbar \to 0$, so we neglect the second term on the right hand side of Equation 4.3, and $S \to \infty$, giving the spins a definite direction [98]. The partial derivative in the first term gives the so-called local field $-g\mu_{\mathrm{B}}\mathbf{h}(\mathbf{S}) \equiv \partial H/\partial \mathbf{S}$, and furthermore the spin operators can be replaced with the continuous magnetization $\mathbf{m} = \mathbf{M}/M_{\mathrm{s}}$. We identify H with the micromagnetic Hamiltonian (Equation 2.23), so the field $\mathbf{h} = \mathbf{H}_{\mathrm{eff}} = -\delta E_{\mathrm{tot}}/M_{\mathrm{s}}\delta\mathbf{m}$. With these substitutions we assemble the classical equation

$$\frac{\mathrm{d}\mathbf{m}}{\mathrm{d}t} = -\gamma(\mathbf{m} \times \mathbf{H}_{\mathrm{eff}}), \tag{4.4}$$

where $\gamma = g\mu_{\mathrm{B}}/\hbar$ is the gyromagnetic ratio.

Equation 4.4 describes magnetization precessing about the effective field at a constant angle. The gyroscopic torque $-\mathbf{m} \times \mathbf{H}$ and the associated circular trajectory of $\mathbf{m}$ are indicated in green in Figure 4.1. It also implies the equilibrium condition that the torque vanishes when the magnetization everywhere is aligned with its local field,

$$\mathbf{m} \times \mathbf{H}_{\mathrm{eff}} = 0, \tag{4.5}$$

the first of Brown's equations [76]. The second is the Neumann boundary condition

$$\frac{\partial \mathbf{m}}{\partial \mathbf{n}} = 0 \tag{4.6}$$

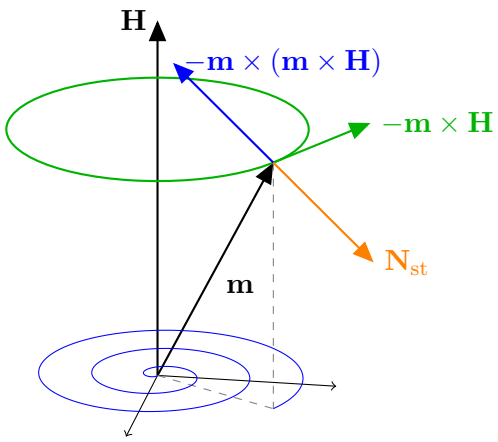

Figure 4.1: Torques in the magnetization equation of motion. Green: gyroscopic torque. Blue: damping torque. Orange: a spin transfer torque (Section 4.2).

required for the exchange field. (On a finite difference grid, so-called mirror boundary conditions at surfaces implicitly satisfy Equation 4.6 [100, 101].) These two equations provide the conditions for metastable configurations and the framework for their calculation. For dynamics, we use open boundary conditions on the scalar magnetic potential (Section 2.1.4) and mirror boundary conditions on the exchange field.

Landau and Lifshitz also introduced a phenomenological mechanism by which $\partial\mathbf{m}/\partial t \to 0$, connecting the conservative precession of Equation 4.4 to the stationary equilibrium of Equation 4.5. The modified equation is

$$\frac{\partial \mathbf{m}}{\partial t} = -\gamma' \mathbf{m} \times \mathbf{H}_{\text{eff}} - \alpha' \mathbf{m} \times (\mathbf{m} \times \mathbf{H}_{\text{eff}}). \tag{4.7}$$

The second term on the right hand side exerts a torque perpendicular to the first that moves the magnetization towards parallel with the effective field while preserving the length of $\mathbf{m}$. The damping torque and the in plane projection of a damped magnetization trajectory are indicated in blue in Figure 4.1. The material property damping parameter α' in Equation 4.7 determines the rate of dissipation of angular momentum.

Landau-Lifshitz damping is unphysical, $\partial\mathbf{m}/\partial t \to \infty$, in the limiting case $\lambda_{LL} \to$

∞, which is itself unphysical. Gilbert derived an alternative to Equation 4.7 using Lagrangian mechanics. He treated the magnetization as a rigid rotatable rod, with potential energy given by Equation 2.23, the kinetic energy of rotation about the symmetry axis of the magnetization, fictitious in the sense that magnetization has no rotational inertia, and a dissipative function representing viscous damping, perpendicular and proportional to the angular velocity. The associated damping coefficient α is a material property representing the average damping throughout the system. Typically $0 < \alpha \lesssim 0.1$. Numerous pathways exist by which micromagnetic energy can transfer to microscopic degrees of freedom, including spin-lattice relaxation, spin-orbit coupling, and the thermal excitation of conduction electrons, and rates corresponding to some of these pathways can be identified experimentally. However, these details do not explicitly enter the micromagnetic effective field, instead we use a homogeneous and isotropic average damping constant extracted from experiment. The Landau-Lifshitz-Gilbert equation is

$$\frac{\partial \mathbf{m}}{\partial t} = -\gamma \mathbf{m} \times \mathbf{H}_{\text{eff}} + \alpha \mathbf{m} \times \frac{\partial \mathbf{m}}{\partial t}. \tag{4.8}$$

Equations 4.7 and 4.8 are equivalent with the substitutions $\gamma' = \gamma/(1+\alpha^2)$ and $\alpha' = \gamma\alpha/(1+\alpha^2)$. These coefficients renormalize the Landau-Lifshitz equation so that in the limit of large damping $\partial \mathbf{m}/\partial t \to 0$:

$$\frac{\partial \mathbf{m}}{\partial t} = -\frac{\gamma}{1+\alpha^2} \mathbf{m} \times \mathbf{H}_{\text{eff}} - \frac{\gamma\alpha}{1+\alpha^2} \mathbf{m} \times (\mathbf{m} \times \mathbf{H}_{\text{eff}}). \tag{4.9}$$

Although no experiment can test whether Equation 4.9 or Equation 4.8 is more "correct" [60], some controversy nevertheless persists [102, 103, 104]. Both forms are now called the Landau-Lifshitz-Gilbert (LLG) equation, with α the (Gilbert) damping constant. For computational reasons we retain the triple product rather than the time derivative in the damping term, so Equation 4.9 is the basis for the numerical methods used in this work.

4.2 Spin transfer torque in a spin valve

When a current of polarized electrons enters a ferromagnet, there is generally a transfer of angular momentum between the propagating electrons and the magnetization of the film [105].

In this section, interfacial spin transfer torque is introduced and integrated into the micromagnetic model. The model system is a spin valve comprised of two ferromagnetic layers F separated by a nonmagnetic metallic spacer layer N, now traversed by a current. The mechanism for the transfer of angular momentum is an exchange interaction between the itinerant spins that carry the spin current and the localized spins that constitute the magnetization [106, 107, 108, 109]. Like giant magnetoresistance, spin transfer torque is a product of band structure and spin dependent scattering. Our understanding originates in Slonczewski's 1D quantum mechanical treatment of conduction electrons in an F/N/F trilayer [106]. We use the subsequent bookkeeping approach of Stiles [60, 105, 52, 110] and others [111, 112] to establish the physical context, basic transport equations, and a formal connection to micromagnetics. We then add a quantitative Slonczewski spin torque term to Equation 4.9.

Slonczewski and Berger's independent derivations of spin transfer torque have far-reaching implications (Section 1.3) [106, 107]. The main prediction was that spin torques could induce mutual precession in the ferromagnetic layers, with the implication of dynamic switching of the magnetization. Berger also described the enhancement of itinerant electron-spin wave coupling near N/F interfaces under the same conditions, predicting altered spin dynamics and damping in the presence of currents, spontaneous precession of the magnetization for supercritical current densities, and an increased electrochemical potential due to spin accumulation. These phenomena can all be detected via the electrical resistance

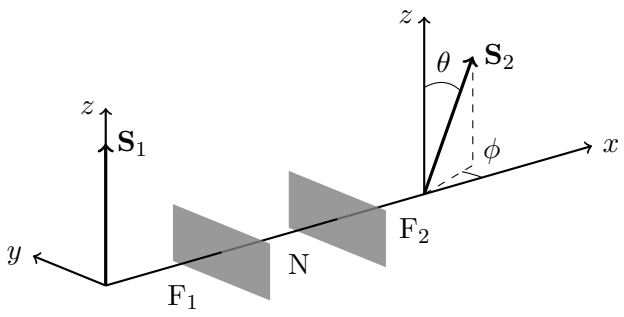

Figure 4.2: Coordinate system for the F/N/F trilayer. Adapted from Ref. [107].

of the system. Slonczewksi additionally predicted spin torque-modulated bistable devices in the vein of field-modulated ones and the spin torque oscillator wherein a dc current excites a dynamical magnetization [106]. Because spin valve systems are metallic, the necessary currents on the of order 10^6–10^8 A/cm^2 can be obtained under relatively low bias [113]. Experimentalists have since demonstrated current induced precessional modes [114] and switching of domains [115], phase locking of spin torque precession with an ac field [116], and electrical detection of current induced microwave oscillations [117].

4.2.1 Spin current basics

An ensemble of moving electrons with number density $n(\mathbf{r})$ comprise a number current density $\mathbf{j}(\mathbf{r})$. With $\mathbf{j}(\mathbf{r})$ being a flux, the continuity equation

$$\frac{\partial n}{\partial t} + \boldsymbol{\nabla} \cdot \mathbf{j} = 0 \tag{4.10}$$

encapsulates both number conservation and the divergence theorem [52]. The spin analogues to $n(\mathbf{r})$, $\mathbf{j}(\mathbf{r})$, and Equation 4.10 are the spin density $\mathbf{s}(\mathbf{r})$, the spin current $\mathbf{Q} = \mathbf{v} \otimes \mathbf{s}$ with net velocity $\mathbf{v}$, and

$$\frac{\partial \mathbf{s}}{\partial t} + \boldsymbol{\nabla} \cdot \mathbf{Q} = -\hat{\mathbf{s}} \frac{\delta s}{\tau_{\uparrow\downarrow}} + \mathbf{n}_{\text{ext}}. \tag{4.11}$$

$\mathbf{Q}$ represents moving spins, so it is a tensor with both real space and spin space projections. Spin is not conserved, so unlike Equation 4.10 the right hand side of Equation 4.11 is

generally nonzero. The spin accumulation δs is spin density in excess of its equilibrium value [111]. The spin-flip relaxation time $\tau_{\uparrow\downarrow}$ parameterizes its decay via transfer of angular momentum to the lattice, and the unit vector $\hat{\mathbf{s}}$ indicates that spin-flip relaxation diminishes δs but does not change its direction.

Our one-dimensional approach centres on two simplifications (the second arises in Section 4.2.2). First, as in Section 3.2.2, we disregard spin-flip processes and spin accumulation. Equation 4.11 becomes

$$\frac{\partial \mathbf{s}}{\partial t} + \boldsymbol{\nabla} \cdot \mathbf{Q} = \mathbf{n}_{\text{ext}}. \tag{4.12}$$

This continuity equation states that the time rate of change of the spin density is given by the net spin current flux plus the external torques on the spin density [52]. It is basically a spin LLG equation – in principle the external torque $\mathbf{n}_{\text{ext}}$ could encapsulate magnetostatic and Zeeman interactions as well as a phenomenological damping torque. In this context, the generalized spin current has two contributions: the exchange spin current, which mediates the exchange interaction in nonuniform magnetization configurations, and the transport spin current. Since the requisite classical fields, damping, and exchange are already accounted for (Section 2.1), micromagnetics excises $\mathbf{n}_{\text{ext}}$ and associates $\mathbf{Q}$ exclusively with the transport spin current. The remaining current induced torque is

$$\frac{\partial \mathbf{s}}{\partial t} = -\boldsymbol{\nabla} \cdot \mathbf{Q}. \tag{4.13}$$

By convservation of angular momentum, and using the divergence theorem, we can write

$$\begin{aligned} \mathbf{N} &= -\int_V \boldsymbol{\nabla} \cdot \mathbf{Q} \, \mathrm{d}V \\ &= -\int_S \mathbf{Q} \cdot \hat{\mathbf{n}} \, \mathrm{d}A. \end{aligned} \tag{4.14}$$

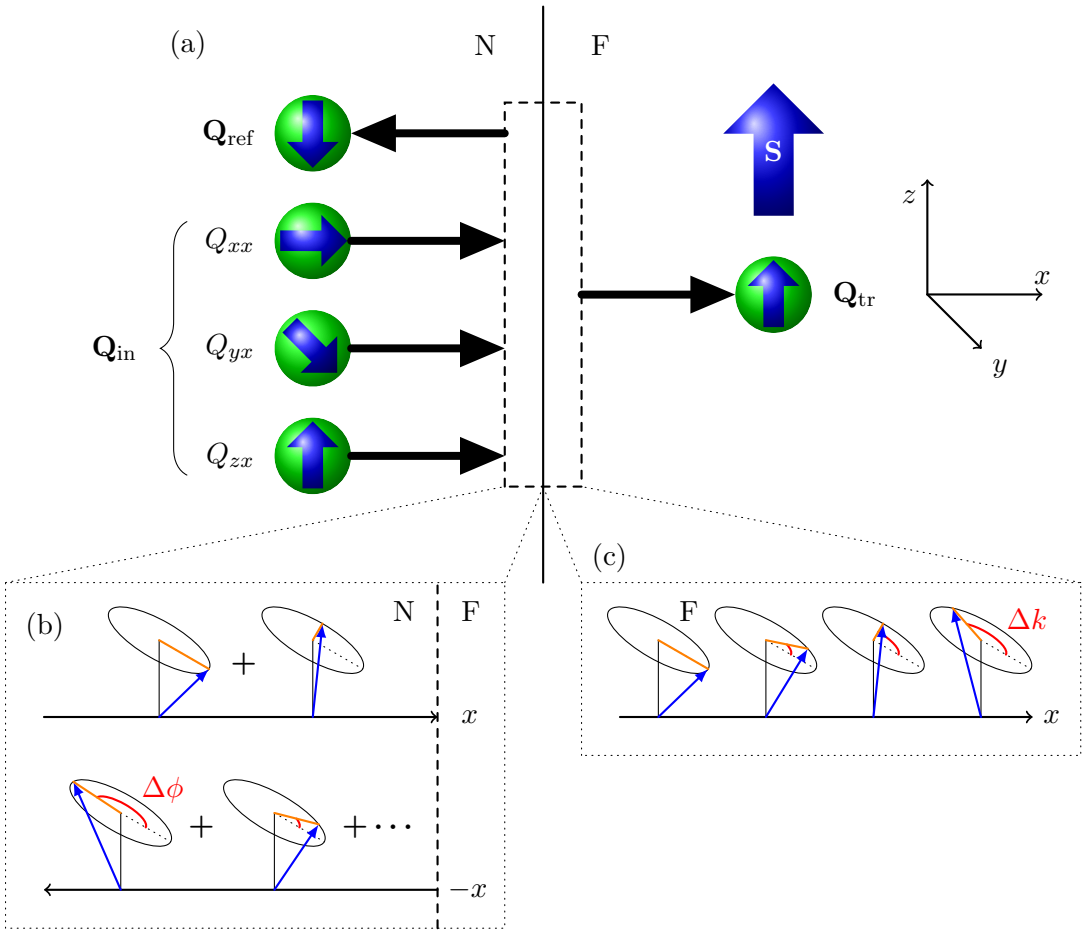

Figure 4.3: (a) A tensor spin current has spin in one direction and propagates in another. (b) Spin rotation. (c) Spin precession.

Equation 4.14 states that the current induced torque on the magnetization in a volume V is given by the net flux of spin current into and out of the surface S that bounds V [105]:

$$\mathbf{N} = \mathbf{Q}_{\text{in}} - \mathbf{Q}_{\text{out}}. \tag{4.15}$$

Discontinuities in $\mathbf{Q}$ are local torques per area exerted by the conduction electrons [118]. Following Section 3.2.2, we expect spin dependent scattering to generate an asymmetric flux, therefore Equation 4.15 implies a spin transfer torque.

In this orientation the spin transfer torque occurs within a few atomic layers of an

N/F interface [106, 108], so we need only consider Equation 4.15 in the integration pillbox in Figure 4.3 [112, 105]. (This coordinate system is the same as Refs. [107, 112, 105, 60] and rotated with respect to Ref. [52] and the experimental convention, Figure 6.1.) The area of each pillbox face is A and $\pm\hat{\mathbf{x}}$ are the surface normals. The spin flux from the left consists of the incident and reflected spin currents, $(\mathbf{Q}_{\text{in}} + \mathbf{Q}_{\text{ref}}) \cdot (-\hat{\mathbf{x}})A$. The spin flux to the right is just the transmitted spin current $(\mathbf{Q}_{\text{tr}} \cdot \hat{\mathbf{x}})A$. According to equation 4.15,

$$\frac{\mathbf{N}}{A} = (\mathbf{Q}_{\text{in}} - \mathbf{Q}_{\text{tr}} + \mathbf{Q}_{\text{ref}}) \cdot \hat{\mathbf{x}}. \tag{4.16}$$

A full account of the scattering problem contained in Equation 4.16 is given in [105]. The incident wavefunction Figure 4.3(a) is a superposition of up and down spins

$$\psi_{\text{in}} = \left[\cos(\theta/2)\mathrm{e}^{-i\phi/2}\,|\uparrow\rangle + \sin(\theta/2)\mathrm{e}^{i\phi/2}\,|\downarrow\rangle\right]\mathrm{e}^{ik_x x} \tag{4.17}$$

where (θ, ϕ) give the orientation of the spin relative to the ferromagnetic spin density $\mathbf{S}$. ($\mathbf{S}$ points opposite $\mathbf{M}$ just as a spin does its magnetic moment.) The outgoing state is also a linear combination of up and down spins, but its component amplitudes depend on transmission and reflection coefficients. The potential step at the interface differs for the two spin components because they have the same energy in the nonmagnet but different energies in the ferromagnet, so the reflection and transmission coefficients are spin-dependent. By the usual prescription of matching the wave functions at the interface (Slonczewski used the WKB approximation), it was shown that $Q_{zx}^{\text{in}} = Q_{zx}^{\text{tr}} - Q_{zx}^{\text{ref}}$ [105], so by Equation 4.16, the longitudinal spin current exerts no torque. However, the same is not true of Q_{xx} and Q_{yx}, so there is a discontinuity in the transverse spin current at the interface and therefore a spin transfer torque (Equation 4.15).

Spin transfer torque due to the spin dependence of transmission and reflection coefficients is called spin filtering. Two other sources of spin torque ensure that the transverse

component furthermore vanishes away from the interface. Spin rotation, Figure 4.3(b), occurs on reflection. The transverse components of the reflected spin current collect a phase factor $e^{i\Delta\phi}$ that rotates the spin from its incident azimuth ϕ. This phase is absent from the transmitted components, so there is discontinuity in the transverse spin current and therefore a second distinct spin transfer torque. Spin precession, Figure 4.3(c), occurs when Q_{xx} and Q_{yx} pick up phase factors $e^{i(k_x^{\uparrow}-k_x^{\downarrow})x}$ on transmission. Since $\Delta k \equiv k_x^{\uparrow} - k_x^{\downarrow} \neq 0$ in a ferromagnet, this term describes spin precession as a function of distance from the interface, and an accumulation of Δkx changes the orientation of the spin vector [52]. According to Equation 4.14, this generates a third spin transfer torque. The magnitude of spin rotation and the spatial period of spin precession are particular to the specific single electron incident wave function in Equation 4.17. Consequently, after summing over an ensemble of electrons spanning the Fermi surface, phase cancellation and classical dephasing respectively eliminate the outgoing transverse components of the spin current.

4.2.2 Slonczewski spin transfer torque

The remaining task is to modify the equation of motion for the magnetization, Equation 4.9, to account for the torques in Section 4.2.1. First we note that torques exerted by itinerant spins on ferromagnetic spin densities are equivalent to torques exerted by itinerant moments on magnetizations. "Spin up" in magnetics usually refers to an electron with magnetic moment parallel to the magnetization, and, according to Equation 4.1, spin antiparallel to the magnetization [119]. Likewise, the localized spin density $\mathbf{S}$ and its magnetization $\mathbf{M}$ are related by $\mathbf{M} = -|g|\mu_B\mathbf{S}/\hbar$, so in transition metal ferromagnets, $\mathbf{M}$ points opposite $\mathbf{S}$ [119]. (Elsewhere g is negative by convention so we make explicit the absolute value [60].) The torque $\mathbf{N}$ defined by Equations 4.13 and 4.15 is a time rate of change of angular momentum and therefore oriented opposite the torque on the magneti-

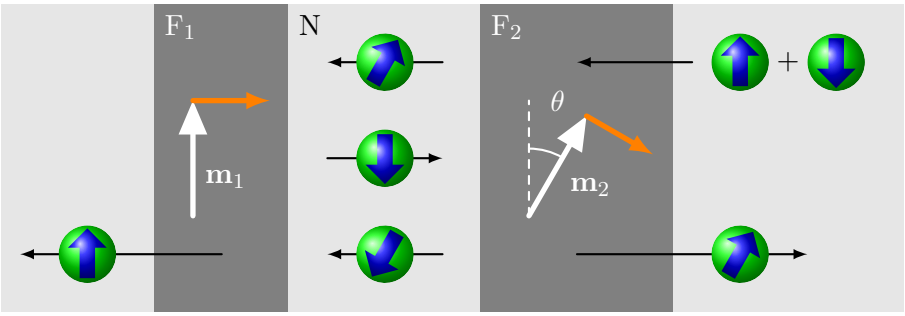

Figure 4.4: Spin transfer torque in a five layer system with ferromagnetic layers F containing magnetizations $\mathbf{m}$ (white arrows), nonmagnetic spacer N, and nonmagnetic left and right leads. The electron current enters from the top right, is spin polarized, and then repeatedly scatters at the N/F interfaces, exerting spin transfer torques (orange arrows) on the magnetizations. Based on a figure from Ref. [112].

zation: $\partial_t \mathbf{M} = -\mathbf{N}|g|\mu_B/(\hbar V)$ in a volume V. In contrast, rotation of the magnetization by an influx of magnetic moments has the same sign as $\partial_t \mathbf{M}$, but "pseudotorque" units of [magnetic moment/(time·volume)] [60].

Our second simplification is perfect spin filtering, that majority spins totally transmit and minority spins totally reflect at an N/F interface [112]. This was Slonczewski's original approach [106] and is a good approximation for transition metal ferromagnets [120, 105]. In this limit we introduce a second ferromagnetic layer and left and right nonmagnetic leads. The five layer system is shown in Figure 4.4, using the same coordinates as Figure 4.3. In Figure 4.4, uniformly polarized ferromagnets F_1 and F_2 have reduced magnetizations $\mathbf{m}_1$ and $\mathbf{m}_2$ (white arrows) that include the angle θ [107]. Conduction electrons represented by Equation 4.17 enter F_2 from the right lead, assume an orientation parallel to $\mathbf{m}_2$ [118], and then transit the spacer layer and impinge on F_1.

Due to spin filtering, the component of the spin-polarized current parallel to $\mathbf{m}_1$ propagates through F_1 and out into the left hand lead, the component antiparallel to $\mathbf{m}_1$ is reflected back into N, and the component transverse to $\mathbf{m}_1$ is completely absorbed at the interface [106], exerting a torque on $\mathbf{m}_1$ proportional to $\sin\theta$ in the $\hat{\mathbf{x}}$ direction (orange

arrow) [112]. For this direction of current, the torque acts to rotate $\mathbf{m}_1$ towards parallel with $\mathbf{m}_2$. The reflected spins now cross the spacer layer from left to right and scatter at the N/F_1 interface. Spin filtering again separates the incident state into three parts, but this torque rotates $\mathbf{m}_2$ away from $\mathbf{m}_1$. For a symmetric spin valve, this induces a windmill-like clockwise rotation of the two magnetizations. With the opposite current direction, the electrons entering from the left lead, the process is the same but the sign of the torque is changed, driving $\mathbf{m}_2$ towards parallel to $\mathbf{m}_1$ and vice versa, leading to mutual counterclockwise rotation. In an asymmetric spin valve, the fixed layer magnetization remains stationary while the free layer rotates, so the two different current directions favour parallel and antiparallel alignment of the magnetizations. Mutiple reflections in the spacer layer diminish the amplitudes but do not change the directions of the spin transfer torques.

In general, from Section 4.2.1 and Figure 4.4, the torque on $\mathbf{m}_1$ is perpendicular to $\mathbf{m}_1$ in the instantaneous plane shared by $\mathbf{m}_1$ and $\mathbf{m}_2$. The unit vector for that plane is $(\mathbf{m}_1 \times \mathbf{m}_2)$, so the direction of the torque is $\mathbf{m}_1 \times (\mathbf{m}_1 \times \mathbf{m}_2)$, the direction of the conduction electron's transverse magnetic moment. Therefore the torque deposited by each electron is $|g|\mu_B/2$ in the $\mathbf{m}_1 \times (\mathbf{m}_1 \times \mathbf{m}_2)$ direction. For a stream of electrons, the rate of incidence is given by Equation 4.10 evaluated in the pillbox of Figure 4.3. In terms of the electric current, it is the charge current density times the surface area divided by the electron charge, $J \cdot A/e$. The time rate of change of the magnetization $\mathbf{m}_1$ in V is then

$$\frac{\partial \mathbf{m}_1}{\partial t} = \frac{|g|\mu_B J}{2eL_1} \mathbf{m}_1 \times (\mathbf{m}_1 \times \mathbf{m}_2). \tag{4.18}$$

where L_1 is the thickness of layer F_1.

Finally, to account for the transport properties of the materials, the right hand side is multiplied by a scalar efficiency function g_τ, giving the Slonczewski spin torque

term [121, 109]

$$\frac{\partial \mathbf{m}_{1,2}}{\partial t} = \gamma \frac{\hbar J g_\tau^{1,2}}{2eL_{1,2}M_{\mathrm{s}}^{1,2}} \mathbf{m}_{1,2} \times (\mathbf{m}_1 \times \mathbf{m}_2) \tag{4.19}$$

with

$$g_\tau = \frac{4P_1P_2^{1/2}}{(1+P_1)^2(1+P_2)(3+\mathbf{m}_1\cdot\mathbf{m}_2) - 16P_1P_2^{1/2}} \tag{4.20}$$

and $\gamma = g\mu_{\mathrm{B}}/\hbar$. The Fermi level polarization factor $P = (n_\uparrow - n_\downarrow)/(n_\uparrow + n_\downarrow)$, with $n_\uparrow$ ($n_\downarrow$) the majority (minority) Fermi level density of states. The efficiency g_τ is often made explicitly dependent on the angle between the magnetizations θ with the substitution $\mathbf{m}_1 \cdot \mathbf{m}_2 = \cos(\theta)$.

We note three features. First, spin transfer torque is proportional to the current amplitude. Second, it peaks in the region $\pi/2 \leq \theta < \pi$ [109]. For weak currents or θ in the vicinity of 0 or π, damping torque compensates spin torque, resulting in the circular or spiral trajectory in Figure 4.1 and no large angle precession or switching. Third, M_{s} and L in the denominator of the prefactor means that magnetically softer materials in thinner layers are comparatively more excitable than harder, thicker layers, making asymmetry in spin valves additionally advantageous for device applications (Chapter 1).

4.3 Summary

This chapter began with dynamic extensions to the micromagnetic model introduced in Chapter 2. The Landau Lifshitz equation for precession in an effective field was introduced and supplemented with a term for magnetic damping. Gyroscopic torque drives the equivalent of Larmor precession for the magnetization in the effective field, and in the absence of external fields or currents it contributes the most torque to the Landau-Lifshitz-Gilbert equation of motion for the magnetization. Damping torque favours magnetization collinear with the effective field, and is smaller than and orthogonal to the gyroscopic torque. Spin transfer torque in the spin valve geometry was introduced in the bookkeeping approach

and then formalized with an additional term in the Landau-Lifshitz-Gilbert equation. Spin transfer torque follows from the total absorption by the magnetization of the transverse component of incident spins. The mechanism that transfers the angular momentum is an exchange interaction between conduction electrons and the localized electrons that comprise the magnetization. With gyroscopic torque, damping, spin transfer torque, and the micromagnetic Hamiltonian of Chapter 2, we have assembled a model sufficient to simulate current-induced magnetization dynamics in multilayered structures. In the following chapter, we review highly nonequlibrium magnetization processes, including switching of the magnetic vortex polarity and chirality, as well as spin wave eigenmodes that form during small-angle excitation or relaxation.

Chapter 5

Vortex dynamics

With the motivations of Chapter 1 and in the subsequently reviewed analytical, experimental, and micromagnetic context, this final background chapter surveys vortex dynamics with an emphasis on switching of topological indices and post-switching relaxation. Polarity switching is most common in the literature due to its experimental accessibility and historical interest in translational motion of the vortex core. Core gyrotropy, the translational mode adapted to a confined system, is an established method to induce dynamic polarity switching and can be motivated by either fields or currents; this as well as switching by excitation with spin waves as predicted by simulation are discussed. Then the brief literature on chirality switching, also via fields or currents, is summarized. The former has been demonstrated experimentally in disks, the latter only in micromagnetic simulations. Various proposed techniques for fourfold control of polarity and chirality are compared. Finally spin wave eigenmodes are introduced, coherent dynamic magnetization structures evident in confined systems during relaxation.

5.1 Polarity switching

5.1.1 Gyrotropy-induced switching

Translational motion of the vortex core has a thorough theoretical framework and is accesible to both time- and frequency-domain experiments. In an influential paper, Thiele started with Equation 4.8 and derived a set of 3D equations for dynamics of a rigid magnetization structure that is parameterized only by its position $\mathbf{X}(t)$ [122]. The Thiele force equation is:

$$\mathbf{F} + \mathbf{G} \times \dot{\mathbf{X}} + \mathbf{D} \cdot \dot{\mathbf{X}} = 0. \tag{5.1}$$

$\dot{\mathbf{X}}$ is the velocity of the structure, $\mathbf{F}$ is an external force, e.g. due to an applied field, $\mathbf{G}$ is the gyrovector, and $\mathbf{D}$ is the dissipation tensor associated with viscous drag.

For any ansatz with the usual limits, see Equation 3.6, the topological gyrovector $\mathbf{G} = -2\pi qp\hat{\mathbf{z}}$, where q and p are the vorticity and polarity respectively [123, 124]. Since $q = 1$ for vortices, the sense of gyration is determined by the polarity. $\mathbf{D}$ is significant near the edge of the disk and depends on the Gilbert damping and the vortex core radius. The right hand side of Equation 5.1 can be replaced with a term $M\ddot{\mathbf{X}}$, an effective mass times acceleration [125], allowing not only for changes in velocity but also deformation of the vortex profile. To first order, a rigid vortex in a disk is a 2D harmonic oscillator, so $M\ddot{\mathbf{X}} = -k\mathbf{X}$. Since $\mathbf{G} \| \hat{\mathbf{z}}$, the resulting equation has only radial components, the restoring force $-k\mathbf{X}$ and gyroforce $\mathbf{G} \times \dot{\mathbf{X}}$. This implies the solution of circular motion about the origin. Higher order solutions reveal a cycloid component to the trajectory, not unlike a charged particle in crossed electric and magnetic fields [126, 127]. The important results we take forward are a dynamic mass that corresponds to core deformation and the identification of a central potential and its associated orbital modes.

Construction of a generally nonlinear confining potential $W(\mathbf{X})$ for a disk system

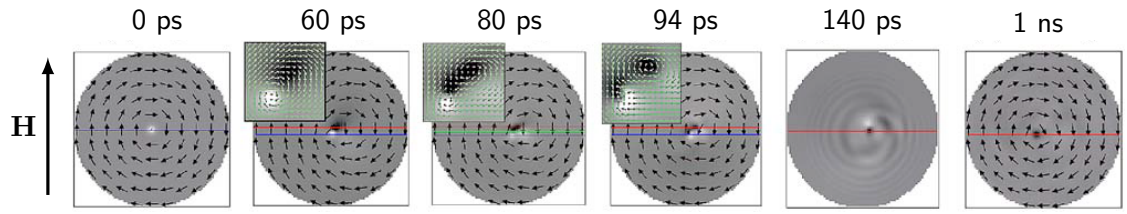

Figure 5.1: Gyrotropic excitation of a vortex core by an in-plane field pulse and nucleation of a vortex-antivortex pair, followed by annihilation of the original vortex with the antivortex, emission of spin waves, and gyrotropic relaxation of the new core. Adapted from Ref. [139].

follows the same methods as section 3.1.3, and the restoring force $-\partial W(\mathbf{X})/\partial \mathbf{X}$ is mainly defined by demagnetization energy [128, 126, 129, 127, 130]. The translational mode as a fundamental excitation of the vortex in a disk was predicted in [131] and later observed with time-resolved magneto-optic Kerr effect microscopy [132]. A model with spin transfer [133] was used to fit the resonance frequency of gyration observed by TR-MXTM and obtain the parameters α and P in Equations 4.9 and 4.19 respectively [134]. Gyration in a symmetric dual vortex nanopillar was considered in Ref. [135] by adding a core-core coupling term to the demagnetization energy. And an elegant method was proposed in Ref. [136] for measuring the nonadiabatic spin torque that occurs when an in-plane current in a ferromagnet encounters a continuously varying magnetization, since executed by pump-probe photoemission electron microscopy [137] and Lorentz microscopy [138].

Two directions on gyrotropic motion have emerged. In the first track, analytical, numerical, and experimental methods are developed to study gyrotropic oscillators. External forces in the presence of damping provoke spiral trajectories, wherefrom circular oscillations become stable when the gyrotropic force compensates the restoring force [131, 140, 141]. Spin transfer torque has been added as a motivating force [142, 143, 144, 145] and coupling between proximal oscillators has been investigated [146, 147, 82, 83, 148, 81, 149], including phase locking [150]. For the accesibility of experiments, technological implications,

and fundamental interest, these pursuits have dominated the literature. The second track focuses on vortex dynamics far from equilibrium. It was noted by Huber and others that the rigid vortex approximation should not hold under realistic fields, and that at realistic velocities the combination of drag and damping could deform the vortex. With the help of micromagnetic simulations, it was found that the topology of the system is not conserved above a critical velocity, and the vortex polarity and circulation can be switched. The critical velocity is several hundred meters per second, as for Walker breakdown of domain walls, and material dependent. Whereas steady state gyrotropic precession is in the realm of broadband FMR, investigation of transient switching dynamics require subnanosecond techniques such as magneto-optic Kerr effect microscopy, x-ray magnetic circular dichroism microscopy, magnetic transmission x-ray microscopy, and numerical micromagnetics.

The first report of dynamic polarity switching by a gyrotropic mechanism was in a simulation paper by Xiao *et al.* [139]. The process is shown in detail in Figure 5.1. During an in plane field pulse, a vortex core ($q = +1$) with positive polarity ($p = +1$), indicated by white contrast in Figure 5.1, spirals out from the center of the disk. E_{dem} increases sharply. As it accelerates, its profile m_z at the radially inward edge of the core dips increasingly into the plane; this distortion causes a rise in E_{exch} but a decrease in E_{dem} due to flux closure between the core and dip. At a critical velocity, the dip decouples from the original vortex, and forms a new vortex with the opposite polarity ($p = -1$), and at the flux boundary between these two vortices, an antivortex ($q = -1, p = -1$) forms due to symmetry. For the thin disk subject to a 290 Oe, 80 ps field pulse in Ref. [139], this occurred within about 80 ps. The stray field of the core at the dip is on the order of -2 kOe, normal to the disk; this determines p for the new pair, and indeed the process can be suppressed by applying an opposing $+2$ kOe pulse [151]. After a short delay (approximately 20 ps in Ref. [139]), the original vortex annihilates with the antivortex, causing a sudden spike in systemic

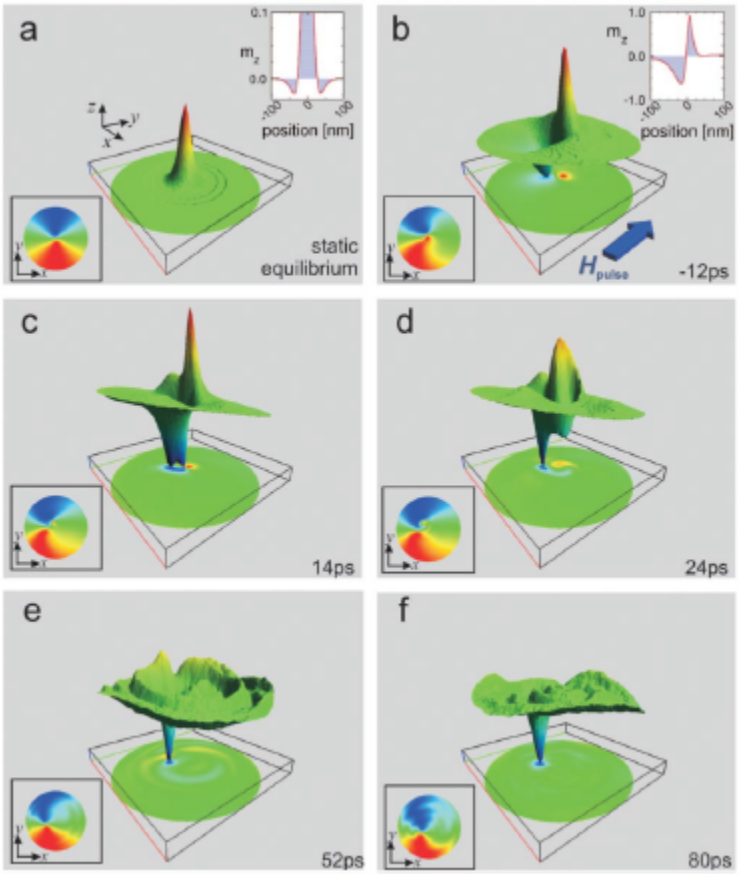

Figure 5.2: Polarity switching visualized with a warped surface plot of m_z. From Ref. [151].

gyroscopic torque with the emission of spin waves radially out from the annihilation site (fifth panel of Figure 5.1). E_{exch} and E_{dem} oscillate in antiphase as they damp back to their original levels; since the short wavelength spin waves are incoherent and dissipate relatively rapidly, this implies an oscillation of the core profile superimposed atop the gyrotropic relaxation. Xiao also described the aftereffects of a supercritical field pulse that induced sequential nucleation and annihilation of multiple vortex-antivortex pairs and left the disk in its original p state. A detailed isoline visualization of polarity switching from Ref. [151] is shown in Figure 5.2.

In the same year, Van Waeyenberge *et al.* demonstrated this mechanism experi-

mentally in a 1.5 µm $Ni_{80}Fe_{20}$ disk [43]. In this experiment, a steady state orbit was induced by a 1 Oe, 250 MHz sinusoidal field and the transient dynamics by a 15 Oe, 4 ns (single period) burst at the same frequency. Their technique, scanning time-resolved MTXM, is sensitive to in plane magnetization components, so they inferred the switch by a change in direction of gyrotropic precession, which is determined by $\mathbf{G}$ and therefore p as predicted in Ref. [131]. This result is remarkable not only for the technique itself but also the very small field amplitude required to reverse the polarity, though the evolution of the magnetization during the 4 ns pulse and switching time could not be obtained. Later micromagnetic simulations have improved on the resolution of the vortex core deformation (Figures 5.2), optimized the pulse parameters, and computed a switching diagram for a subset of the pulse amplitude-duration parameter space [151]. Confirmation has been obtained by time-resolved photoemission electron microscopy with nonresonant pulses [152] and by single-shot magnetic resonance force microscopy with resonant pulses [153]. Chronologically, the next prediction was polarity switching via spin transfer torque. The time evolution of the free layer of a spin valve nanopillar with a perpendicular polarizer has been calculated using versions of Equations 4.9 and 4.19 with various expressions for $\mathbf{H}_{\mathrm{m}}$ [154] and a modified Thiele equation in comparison with micromagnetics [155], both finding critical currents in the range 10^7–$10^8 \mathrm{A/cm}^2$. In the same geometry, Ref. [156] investigated the role of the current induced Oersted field during excitation. In Ref. [157], toggle switching by in plane field pulses was imaged before and after with MFM and compared to micromagnetic simulations. This orientation requires larger amplitude pulses ($10^{10} \mathrm{A/cm}^2$) and involves the nonadiabatic spin torque. Temperature dependent switching diagrams [158] and real time observation via magnetoresistance [159] followed. In summary, switching via pair creation and annihilation is a very general process. It is insensitive to changes in aspect ratio, occurs also in squares and ellipses [151], and does not depend on the damping parameter α.

5.1.2 Nongyrotropic switching

For completeness, we raise one other polarity switching scheme, of which there has been no experimental confirmation. Several groups have reported micromagnetic simulations of resonant switching of vortex polarity without gyrotropic excursion of the core [160, 161, 162, 163]. In Ref. [160], a vortex with $p = 1$ was subjected to a perpendicular 300 Oe, 10.4 GHz sinusoidal field tuned to excite the fundamental radial spin wave mode (Section 5.3). The result was a radial spin wave reflecting between the vortex core and the disk edge, modulating the core radius in phase with the external field. In Fig. 2 of that paper, it appears that the dip around the core maintains its negative polarization with respect to the antinode and core, but the frames are irregularly spaced with respect to the period of excitation so it is difficult to confirm. After building amplitude for about about 600 ps ($\sim$ 6.2 cycles), the standing spin wave became so positive and the dip so negative that the core switched polarity to release the built up exchange energy. The dip also flipped, and short wavelength spinwaves were emitted to dissipate the excess exchange energy. After about 40 ps, the core switched again. In a later paper it was clarified that the switching process involves the axial propagation of a Bloch point (Section 3.1) from top to bottom, breaking the local symmetry of the configuration [162]. The authors of [161] were able to reduce the initial build up and switching time to 150 ps by increasing the field amplitude to 1.4 kOe. And by using a fine, sub-l_{ex} mesh, they were able to resolve the injection and passage of a Bloch point (Section 3.1.2). Bloch point-mediated switching was predicted in Ref. [74], with Bloch point velocities on the order of 2500 m/s, far higher than the critical velocities of domain walls and vortices. There is also the possibility of using azimuthal, rather than radial, spin waves to excite the vortex core, with short bursts of an in-plane alternating field that couple to the gyrotropic mode [164, 165].

The authors of Ref. [166] sought to optimize this technique with nonresonant

excitation. Using fields from 0.4 to 2.0 T, with 1 fs rise times and 0.1–1.0 ns durations, they constructed a switching diagram that shows no systematic dependence on amplitude or duration but rather appeared stochastic. During switching, the pulse amplitude was so large that the core radius approached R; then the edge magnetization rotated opposite the core, the pulse was cut off, and everything reversed polarity. Such large amplitude radial spin waves were excited that the core continued to periodically switch until damping out to a subcritical amplitude, and the resulting switching diagram simply reflects the whether an odd or even number of switches occurred. For lesser amplitudes, 0.23–0.3 T, the switching diagram shows a periodic dependence on pulse width. In these cases the core only switched if the pulse cutoff coincides with a spin wave maximum along the direction of core polarization; this condition corresponds to the resonant spin wave assisted switching discussed above. In order to optimize the high field process, the authors restricted the applied field to a 15×15 nm region centered on the core. Shown for a 1.6 T, 80 ps pulse in Fig. 4 of Ref. [166], Zeeman energy forced reversal of the core without the global excitation of radial waves – spin waves were generated only during relaxation. The result was a switching diagram with two distinct regions and a critical pulse amplitude of about 1.0 T for 40–100 ps pulse widths. With this technique they were able to switch the core polarity in about 15 ps, ten times faster than the radial wave method and without the sensitive dependence on pulse width. It should be pointed out that these pulse parameters are extreme from an experimental standpoint, untenable for device application, and that masking a field to a nanometric region is unproven.

5.2 Chirality switching

Chirality switching is considerably less studied than polarity switching, with results coming from micromagnetic simulations and a small number of experiments. One strategy for switching is to make the chirality states nondegenerate with respect to the relative orientation of a geometric feature and an applied field and then nucleate a fresh vortex in the system. Similar to polarity switching, there are also field pulse methods that require precise pulse timing with respect to the magnetization evolution. Finally, there is the possibility of circulation switching via spin torque transfer (Chapter 6). In this section, we cite and review the experimental and micromagnetic bodies of work regarding these approaches.

5.2.1 Magnetic field methods

The most common scheme for chirality control came about shortly after the first vortex micrographs were published in Ref. [38]. By cutting off one edge of the disk, then applying a saturating field along the flat edge and reducing it to zero, Schneider *et al.* nucleated vortices where the magnetization along the flat edge preferentially aligned with the external field, thus determining the overall chirality [167]. Note that, not dissimilarly to translational mode polarity switching, this requires annihilation of the vortex, in this case by sweeping it out of the disk.

Several studies have built on these results with other defects or deviations from circularity. Yakata *et al.* clarified nucleation rules for odd-sided polygons relaxing from saturation [168]. Using MFM, they contrasted results for triangles, squares, pentagons, etc. In another paper, the same group used an Oersted field in a nonlocal spin valve to field-bias one side of a square-shaped element; this was shown to select chirality on nucleation during a hysteresis cycle [169]. In Ref. [170], before-and-after MFM images were compared to

micromagnetic simulations in triangles. Another paper simulated polarity and circulation control in heptagonal nanomagnets using field pulses [171]. First, the state was saturated with a 1 kOe, 1 ns field pulse along one in plane direction. After the pulse, the magnetization near each heptagonal edge rotated from the field direction to tangent the closest edge, creating a multidomain configuration with two vortices. The one circumscribed by four sides plus the middle of the disk pushed the smaller one out, so the eventual circulation was determined by the relative orientation of the applied field and one reference side, to which the final vortex was antialigned. The annihilation, renucleation, and subsequent annihilation spanned about 3 ns. It should be noted that polygons with or without a vortex at the center of the disk, particularly those with few sides that do not approximate a circle very well, often have domain walls connecting the center of the disk to the vertices. Repeatable processes dependent on the rearrangement of domain walls on top of vortex manipulation or multivortex dynamics are slow and invite nonlinear complications.

In an experimental work, Uhlíř *et al.* demonstrated reliable circulation control using static and pulsed fields. Using directional ion beam sputtering, the authors deposited disks at a 15° angle of incidence so that the mask defining the disk shape also shadowed one edge of it, resulting in a wedge-shaped profile over about a third of the disk. First, static fields were shown to reorient the disks to a circulation determined by the orientation of the field relative to the wedge edge, in before-and-after MTXM images. Then, pulse fields on the order of 250 Oe, 1.5 ns were used to switch the chirality of the vortex. It was found that the required amplitudes for dynamic switching were approximately half of those required for static switching, with the required pulse width increasing linearly with diameter. Second, time-resolved MTXM was used to observe the magnetization dynamics. As expected, they found the vortex core ejected from the disk by the applied field, with chirality selection occuring on renucleation, and pulse width dependence reflecting the time

needed for the core to spiral out from the center to the edge of the disk. The trajectory is affected by the rise time of the pulse relative to the eigenfrequency of the translational mode; for various combinations of these parameters and the aspect ratio the core can be expelled before reaching the critical velocity for polarity switching. Neither the original paper [172], its supplementary material, nor a follow up paper [173] discuss the mechanism that breaks chirality symmetry in their system.

There is also a method that eschews the defect. Ref. [174] found that a position-dependent field can break the symmetry between chiralities, using a 2D classical spin lattice model with exchange, Zeeman, and dipolar energies. As in Ref. [166] above, they used a mask to restrict an in plane field pulse to a region of the disk shaped like a slice of pie with the vertex near one edge and the arc aligned with the opposite edge of the disk, comprising approximately 85% of the surface area. With a 1.6 kOe field parallel to one edge of the mask, the vortex was swept from the disk. The unmasked region aligned uniformly parallel to the field pulse, but the masked regions retained some curl with sign determined by in plane flux closure. Once the transition configuration was obtained, the pulse was cut off (about 7 ns having elapsed) and the magnetization curled into an S state and then a vortex. In Figure 2 of that paper it appears that multiple solitons form during renucleation as the edge poles of the S state reconfigure. For reasons of fabrication this method is unpractical.

Another simulation paper approached this concept micromagnetically [175]. For field pulse amplitudes between 510 and 570 Oe, the vortex in their system exits the disk without switching polarity. After a few nanoseconds, the applied field eventually pins the disk in an onion configuration (Section 3.1). However, the transition configuration between vortex expulsion and the onion state is an indistinct C state that oscillates between slightly clockwise and slightly counterclockwise. If the pulse is cut off when the C state is clockwise, a clockwise vortex will nucleate, and vice versa. The window for the cutoff, to choose the

final chirality, is less than 180 ps (a half-cycle of the reported 2.8 GHz frequency). Timing the pulse according to a resonance of the system is similar to the lower field regime of nonresonant nongyrotropic polarity switching discussed in Section 5.1.2 [166]. Two fast nonresonant analogs have also been reported. The first to employed a 0.5 T, 42 ps out of plane pulse to rapidly and globally rotate the magnetization out of plane [77]. The magnetization was shown to rotate through the hedgehog transition configuration, having no effect on exchange but significantly increasing demagnetization energy, and into the opposite chirality, at which point the pulse was cut off (Figure 10 of Ref. [77]). The second study found a similar result for a Lagrangian model system subject to a 1 T, 1 ps field in a process very sensitive to the pulse amplitude [176]. Despite similar modes of excitation, none of the nonresonant nongyrotropic polarity switching papers discussed above reported chirality reversal, and since the nonresonant field-pulse chirality switching method is likewise inaccessible to experiment, Ref. [77] remains unexplained.

5.2.2 Current methods

Reliable field-based methods for chirality control generally operate no faster than the timescale of annihilation, renucleation, and relaxation, and additionally require special fabrication methods. Also, critical fields increase with decreasing device size [172] and their leakage poses significant device integration issues (Chapter 1). Current-based methods, on the other hand, have the potential advantages of speed, low energy requirements, compactness, and advantageous critical current scaling.

Current induced chirality control typically utilizes spin transfer torque and therefore the spin valve nanopillar geometry. The design requirements are: (1) A combination of aspect ratios and material properties that promote a stable vortex in the free layer and the desired configuration in the polarizer. (2) Band matching for good GMR and spin transfer

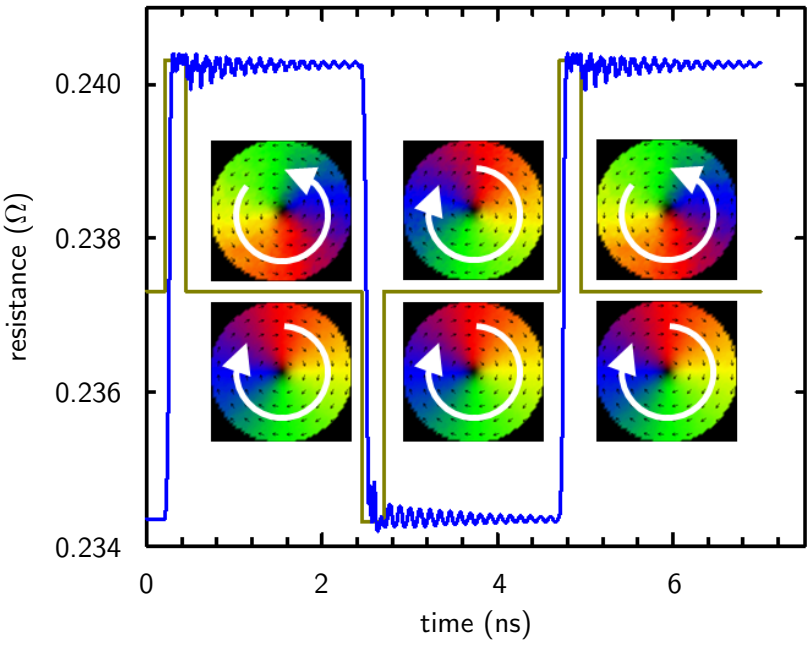

Figure 5.3: Time-resolved magnetoresistance during toggle switching of the free layer chirality in a spin valve nanopillar. The insets show the in plane magnetization of the fixed (bottom row) and free (top) layers. The curve in the background represents the current pulses. Adapted from Ref. [177].

properties. (3) Asymmetry in the fixed and free layer response, for damping and bistability. (4) A nanometric pillar diameter for low critical currents and high GMR signal, and to reduce energy requirements, reduce the Oersted field contribution (if desired), and limit Joule heating.

Chirality switching was demonstrated in micromagnetic simulations shortly after the experimental verification of field pulse polarity switching. In Ref. [179], a 3.8×10^8 A/cm^2, 200 ps current pulse was shown to effect switching of the free layer chirality in a dual vortex spin valve nanopillar. In that case, considerable incoherence in the free layer magnetization accrued during switching, resulting in a complex relaxation process. Further study found more coherent switching over a range of pulse parameters, and a follow up paper reported the detection of time-resolved relative chirality by GMR, a switching

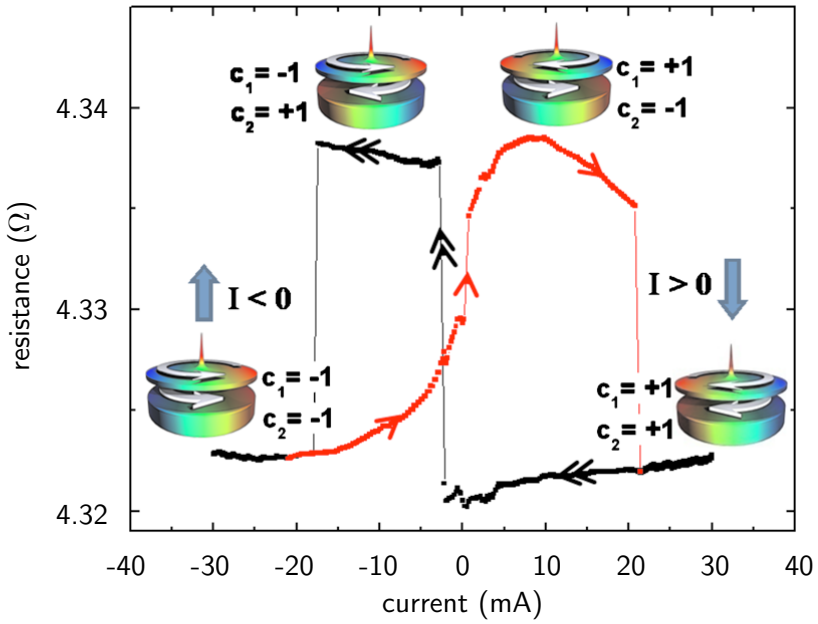

Figure 5.4: Experimental verification of chriality selection by spin torque transfer. From Ref. [178].

diagram, and basic frequency domain properties of the system [177]. Figure 5.3 from that work shows the time-resolved magnetoresistance of a spin valve nanopillar toggle-switched by a current pulse train. Switching occurs within tens of picoseconds after the onset of the pulse, with post-switching ringing damping out over approximately 2 ns. The system, switching mechanism, energetics, and other results of Refs. [179] and [177] are discussed in Chapters 6 and 7.

In the pursuit of a two-bit device, reliable fourfold control (control of both polarity and chirality) is desirable. In the current-based proposal of Ref. [180], Oersted fields were taken into account and the exciting current was assumed polarized, but the polarizing layer was not modeled. First, four phases were identified on a switching time versus current density switching diagram: no excitation, gyrotropic excitation, polarity switching, and polarity plus chirality switching. For positive current polarity, the latter occurred only for vortices with left handed circulation, for the following reason: In that regime, the current

densities and pillar diameter were both large enough that, after the vortex switched polarity, the Oersted field generated by the current imposed the final chirality. (There was also a fifth regime, where currents six times larger forced the final chirality without spin torque.) Quoted pulse widths were 10–250 ns for polarity switching and < 30 ns for polarity-plus-chirality switching. Thus, utilizing both signs of current, any of the fourfold initial states could be transformed to any other state with a one, two, or three pulse train, chirality-only switching requiring an intermediate spell in the wrong polarity state. Overall, this method is disadvantageous due to its relatively slow speed, reliance on gyrotropic polarity switching, and the unfavorable scaling of the Oersted field.

Finally, there have been two experimental confirmations that quasistatic spin polarized currents can favor a particular handedness, assisted by the azimuthal Oersted field to an extent dependent on the pillar radius. The first experiment employed a pillar with a ring shaped cross section, in which a coreless vortex is an equilibrium state, and the Oersted field played a significant role [181]. In contrast, Ref. [178] reported on a conventional nanopillar similar to the ones in Refs. [179] and [177] and this thesis. In both experimetal cases, there was a clear asymmetry to the hysteretic resistance as a function of current that signified spin transfer torque (Figure 5.4). Ref. [178] confirms that spin transfer torque is a viable means of chirality control.

5.3 Spinwave modes in disks

In addition to the low frequency translational mode discussed in Section 5.1 specific to the vortex state, magnetic disks in general support high frequency normal modes not unlike the vibrations of a drum head. Like the ground states, their structure reflects the confining potential due to demagnetization energy and therefore the geometry. Figure 5.5

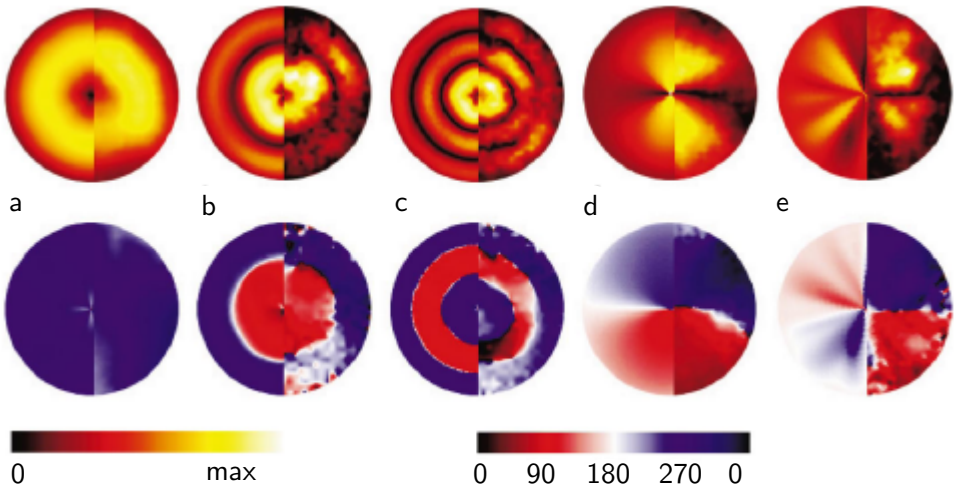

Figure 5.5: Experimental TR-MOKE maps of amplitude (top row) and phase (bottom) for vortex-state eigenmodes. (a–c) Radial modes. (d–e) Azimuthal modes. From Ref. [182].

shows maps obtained by TR-MOKE of the FFT amplitude (top row) and phase (bottom) of disks relaxing after a short out of plane field pulse [182]. The radial modes (a–c) with one, two, and three concentric antinodes are found at increasing frequencies (2.8, 3.8, 4.5 GHz); the azimuthal modes (d–e) have one and two diametric nodal lines and show negative dispersion (2.0, 1.7 GHz). In this section, we summarize two approaches to finding subsets of the eigenmode spectrum of a vortex state disk, then cite several related experiments. Specifically, the conventional radial eigenmode spectrum provides context for the radial spin wave eigenmodes discussed in Chapters 7 and 8 that form during relaxation after chirality switching of a nanometric dual vortex nanopillar.

In the usual notation, the integers (m, n) number the azimuthal and radial character of the eigenmodes. We adopt the convention that the first radial mode, with zero amplitude at the core and edge and zero nodes in between, is labelled $n = 0$. Azimuthal mode labels are consistent: $m = 1$ has a diametric nodal line, $m = 2$ has nodal lines along two perpendicular diameters, and so on. Radial modes have azimuthal (or axial or circu-

lar) symmetry like an archery target, azimuthal modes have radial symmetry like a wagon wheel, and hybrid modes have both like a dartboard.

5.3.1 Radial modes

During coherent relaxation, the magnetization consists of an equlibrium state and a time dependent small angle precession about it: $\mathbf{m}(\mathbf{r}) = \mathbf{m}_0 + \boldsymbol{\mu}(\mathbf{r})$. In an orthonormal basis, these linear, transverse excitations take the form

$$\boldsymbol{\mu}(\mathbf{r}, t) \approx \sum_i c_i(t)\boldsymbol{\mu}_i(\mathbf{r}) \tag{5.2}$$

where c_i are the eigenmode amplitudes and $\boldsymbol{\mu}_i$ their profiles [183]. Trial functions for $\boldsymbol{\mu}(\mathbf{r})$ must have the azimuthal symmetry of $\mathbf{m}_0$, be locally orthogonal to $\mathbf{m}_0$, to preserve the length of $\mathbf{M}$, and satisfy the edge boundary condition due to demagnetization.

To construct the modes, one first builds a model for the potential energy of the confined vortex system as in Sections 3.1.3 and 5.1. In the usual approach developed by Guslienko [140], Zaspel and Ivanov [57] and others [50], using the spherical magnetization basis and cylindrical disk basis, the energy due to exchange and demagnetization is [140]

$$W = L \int \mathrm{d}^2\boldsymbol{\rho} \left[A(\nabla\Theta)^2 + \sin^2\Theta(\nabla\Phi)^2 - \frac{1}{2}\mathbf{H}_\mathrm{m} \cdot \mathbf{M} \right]. \tag{5.3}$$

Foremost are the radial modes $n = \{1, 2, \dots\}$. The exchange energy is concentrated in and stabilizes the vortex core, so the dynamics occur away from the core and the exchange contribution to the potential is constant. In other words, these modes are magnetostatic in origin and have wavelength on the order of the disk radius. In the non-core region where $\Theta(\rho) = \pi/2$, the transverse dynamic part $\boldsymbol{\mu}(\rho) = (\mu_\rho, 0, \mu_z)$ rotates elliptically about the static part $\mathbf{m}_0 = (0, m_0^\phi, 0)$. Nonzero $\mu_\rho(R)$ means side surface charges, and μ_ρ and μ_z in concert create volume charges; both increase the dynamic part of E_dem. In contrast, the rigid translational mode of Section 5.1 has a constant surface charge density and no radial

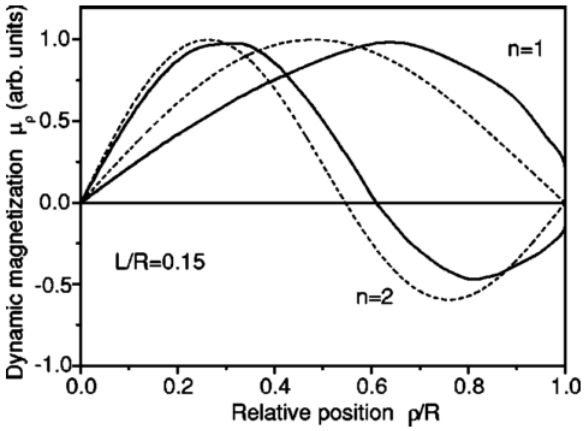

Figure 5.6: First two radial eigenfunctions $\mu_n(\rho)$ for disk aspect ratio 0.15. Dotted lines: Bessel functions. From Ref. [140].

component at the edge. This difference in dynamic magnetostatic energy is the reason the radial eigenmodes have higher frequencies than the translational mode.

Guslienko used the undamped Landau-Lifshitz equation (Equation 4.4) as the equation of motion and the magnetostatic Green's function representation of $\mathbf{H}_\mathrm{m}$ in Equation 5.3,

$$\mathbf{H}_\mathrm{m}(\mathbf{r}) = \hat{G}[\mathbf{m}(\mathbf{r}')] \int \hat{G}[\mathbf{r}, \mathbf{r}']\mathbf{m}(\mathbf{r}')\,\mathrm{d}V',$$

where

$$G_{\alpha,\beta}(\mathbf{r}, \mathbf{r}') = -(\nabla_\mathbf{r})_\alpha (\nabla_{\mathbf{r}'})_\beta \frac{1}{\mathbf{r} - \mathbf{r}'}$$

is the tensor magnetostatic Green's function in cylindrical coordinates and $\alpha, \beta = (\rho, \phi, z)$ [64, 184]. The strategy is to find a system of eigenfunctions for the integral operator of the magnetostatic field $\hat{G}$, then use them as basis functions for an expansion of $\boldsymbol{\mu}(\mathbf{r})$.

Guslienko made the following assumptions: (1) $\mathbf{m}$ is uniform through the thickness L of the disk. This is reasonable for L on the order of the core radius and $L \ll R$, and leads to the form of Equation 5.3. (2) Azimuthal symmetry; $\mathbf{m}_0$ and $\boldsymbol{\mu}(\rho)$ have it. After averaging over z, z' and ϕ' only the $\rho\rho$ and zz components of $G_{\alpha,\beta}$ are nonzero. (3) The

exchange contribution is not dynamic, as reasoned above. (4) Only μ_ρ contributes to the dynamic magnetostatic energy. With these simplifications the task becomes an eigenvalue problem for the operator $\hat{G}$. By the spectral method Guslienko obtained the orthogonal set of eigenfunctions

$$\mu_n(\rho) = c_n J_1(\kappa_n \rho), \tag{5.4}$$

where c_n are the normalization constants, $J_1(\rho)$ is the Bessel function of the first kind, and α_n is the nth root of $J_1(\rho) = 0$. $\kappa_n = \alpha_n/R$ are a set of quantized radial wave numbers obtainable in the limit of strong pinning at the edge. In the limit of perfect pinning at the edge, they depend only on L and R [131]. Figure 5.6, from Ref. [140], shows the Bessel functions, which are the exact solutions when $L \to 0$ (dotted lines), and numerical solutions of the eigenvalue problem for aspect ratio $L/R = 0.15$ (solid lines). To first order, the eigenfrequencies are proportional to $\sqrt{L/R}$, and for thin disks the eigenfrequencies depend only on the aspect ratio. For an aspect ratio of 0.1, typical frequencies for the $n = \{0, 1, 2\}$ modes are 11, 15, and 17 GHz respectively [140].

5.3.2 Azimuthal modes

Zaspel and Ivanov and others studied the translational and high frequency azimuthal modes $m = \{\pm 1, 2, 3\}$ as well as the radial modes $n = \{0, 1\}$ [126, 185]. Note that there are two distinct $(\pm 1, 0)$ modes excited by an in plane field: the low frequency translational mode of Section 5.1 and the rotating, higher frequency azimuthal mode considered here. They are contrasted at the end of this section.

In azimuthal modes, different to the radial modes in Section 5.3.1, scattering between spin waves and the vortex core plays a critical role. The equilibrium and dynamic

magnetizations take the form

$$\Theta = \Theta_0(\rho) + \vartheta(\rho, \phi, t)$$

$$\Phi = \phi + \pi/2 + \mu(\rho, \phi, t)$$

where $\Theta_0(\rho)$ obeys limits of Equation 3.6 and ϑ and μ are small transverse oscillations about the static state. Interestingly, a term $\beta = 2qm\cos\Theta_0/\rho^2$ in the coupled equations for ϑ and μ lifts the degeneracy of clockwise and counterclockwise rotation ($\pm|m|$) [126]. Therefore, in contrast with the radial modes, the azimuthal modes are doublets, and since $\cos\Theta_0$ is determined by the core polarity, the doublet splitting depends on the product qp which is proportional to the magnitude of the gyrovector. So β is nonzero when $|m| \geq 1$ and the resultant splitting is attributed to the gyroscopic force.

In disks with a finite thickness and a nonlocal magnetostatic field, the dynamic magnetization contributes a position dependent dynamic exchange energy to the first term in the integrand of Equation 5.3 [57, 186]. Again the contributions to $\mathbf{H}_\mathrm{m}$ are volume and surface charges (Section 3.1.3), reduced at equilibrium to the surface charges on the top and bottom of the disk due to the vortex core. The volume charges are small, but if neglected the model underestimates the calculated eigenfrequencies compared to experiment, so they are treated using perturbation theory [57]. The remaining contribution to $\mathbf{H}_\mathrm{m}$ is the edge surface charge, which is required to find an effective boundary condition for the equation of motion. Using separation of variables, the ansatz for azimuthal and radial components is

$$\vartheta(\rho, \phi, t) = f(\rho)\cos(m\phi - \omega t)$$

$$\mu(\rho, \phi, t) = g(\rho)\sin(m\phi - \omega t).$$

The edge magnetostatic energy due to $\mu(\rho, \phi, t)$ is localized in the region $R - \rho \ll R$. The exchange energy is found by plugging f and g into the exchange operator and integrating over z and ϕ; the resultant radial integrodifferential equation simplifies to Neumann

boundary conditions on $g(\rho)$. The combined boundary condition takes the form

$$G(k) = \frac{\partial g(\rho)}{\partial \rho}\Big|_{\rho=R} + g(R)\Lambda(R, L, l_{\rm ex}) = 0$$

where $\Lambda(R, L, l_{\rm ex})$ is akin to the effective pinning parameter $d(p)$ in Equation 8 of Ref. [187] and depends only on characteristic lengths [188]:

$$\Lambda = \frac{L}{2\pi l_{\rm ex}^2} \ln \frac{4R}{L}. \tag{5.5}$$

The subsequent procedure is to write down the Landau-Lifshitz equations for f and g. Once $g(\rho)$ is known, the boundary conditions can be applied to obtain the wave number k, given by the zeros of $G(k)$, and then the frequency spectrum from the dynamical equations. Without the vortex, the radial eigenspectrum is $\mu = \sum_m C_m J_m(k\rho)\sin(m\phi + \omega t + \delta_m)$, where C_m are normalization coefficients and δ_m are phases. No splitting is found. With a vortex, the solution in $\rho \gg l_{\rm ex}$ has the same form, but with

$$J_m(k\rho) \to J_m(k\rho) - \sigma_m(k, l_{\rm ex}) Y_m(k\rho), \tag{5.6}$$

where Y_m are the Neumann functions and $\sigma_m(k, l_{\rm ex})$ is the scattering amplitude for the magnon vortex interaction [57]. For $m = \pm 1$, $\sigma_m(k, l_{\rm ex})$ has its maximum value $\pi k l_{\rm ex} m/4|m|$, which depends on the sign of m and determines the splitting of the $|m| = 1$ doublet. So, the core breaks the rotational symmetry of the CW and CCW rotations because magnon scattering by the core is different for the CW and CCW modes [185]. These modes are therefore circularly polarized. The obverse, that the structures of azimuthal spin waves excited by single period bursts of an RF field depend on the clockwise or anticlockwise circulation of the excitation, has been observed with MXTM [164].

Note also the anomalously low frequency of the translational mode $|m| = 1$. Predicted eigenfrequencies run between 0.5 and 1.2 GHz for aspect ratios from 0.05 to 0.4 [140, 188], approximately twice the splitting of the higher frequency azimuthal modes [126]. In

contrast, the first radial mode was predicted to precess at 11 GHz in Ref. [140], in the same range as the high frequency azimuthal modes and the modes of a uniformly magnetizated disk [184]. (All of these values are in approximate agreement with micromagnetic simulation and experiment.) While the higher frequency modes are generally long wavelength, small angle oscillations about the ground state, the translational mode is a long-wavelength wholesale shifting of the ground state itself. It is considered a pseudo-Goldstone mode, adapted to the boundary conditions of the disk much as the vortex is a soliton adapted to the same boundary conditions [126].

For our purposes, it is important to note first that gyrotropy of the vortex core affects not only the transient dynamics (Section 5.1) but also the high frequency precessions of relaxation. Second, while the core does not couple directly to the conventional radial modes, dynamic exchange, which is localized in the core and typically neglected in radial mode calculations, is increasingly important with decreasing disk radius. It has been predicted that the ignoring the vortex core on the grounds that it is small relative to the disk radius may not hold for $R < 200$ nm [140]. Third, the local magnetostatic energy approximation enabled by conventional ansatzes fails when the edge magnetization turns out of plane [58], and it will be shown that interlayer coupling in a nanopillar can induce this condition (Section 6.2).

5.3.3 Experiment

In parallel, micromagnetic simulations and experiments confirmed many of the analytical findings. Ref. [189] showed TR-MOKE and pulsed FMR investigations of the effects of in plane and perpendicular pulsed fields on $R = 350$ nm, $L/R = 0.085$ $Ni_{80}Fe_{20}$ disks. For perpendicular exciation, they found a strong FMR resonance at 9.3 GHz and a much weaker and rather broader peak at 13 GHz. For in plane excitation, peaks were found

at 0.4, 6.0 and 7.25 GHz, corresponding to the translational and rotational ($|m| = 1$) modes, and 9.5 and 12.8 GHz, matching radial modes. All were reproduced well by micromagnetic simulations. In addition, they simulated a ring with the same outer dimensions but a 5 nm-diameter hole in place of a vortex core – the ground state of a ring is a coreless vortex since the magnetization can lie tangent an edge at each radii, with no stray field energy and minimal, uniform exchange. They found only one resonance in the range of the $m = \pm 1$ modes: a 6.6 GHz standing wave polarized along the direction of the field pulse. Without the core, there was no doublet, as predicted in Ref. [57]. In this clever way, Ref. [190] provided experimental confirmation using TR-MOKE, operating on larger, thinner disks with aspect ratios 0.0025–0.015 and rings with 100 nm central holes. They found $m = \pm 1$ doublets in the disks and only singlets in the rings. These and other groups also measured the aspect ratio dependence of frequency [191], recorded coupled $(1, \{0, 1, 2, 3, 4\})$ modes [192] with TR-MOKE, and compared BLS amplitude maps to a generalized radial mode model [193]. In all of these cases, the systems were isolated single layer disks, with radius larger than 200 nm and aspect ratios much less than one, excited by a uniform magnetic field.

There have been a small number of studies on eigenmodes in vertically coupled disks. Spin wave spectra of nanopillars with uniform in plane [194] and perpendicularly magnetized [183] magnetic layers have been investigated. In the latter case, radial and azimuthal modes were found to be well-described by Bessel functions with strong edge pinning, and ST-FMR measurements confirmed the micromagnetic spectra. And recently, in a micromagnetic study, radial eigenmodes in a large diameter, exchange coupled, symmetric dual-vortex nanopillar were generated by an out of plane field [195]. The spectrum found showed a strong dependence on the sign of the interlayer coupling.

5.4 Summary

This chapter concerned magnetization dynamics in vortex-state magnetic disks. Switching of the topological polarity and chirality of the vortex by both magnetic field- and current-induced means were discussed in the context of Chapter 1. Reliable polarity switching proceeds by way of gyrotropic excursion of the vortex core, vortex-antivortex nucleation and annihilation, and subsequent relaxation. Chirality switching is less proven and most methods for it begin with annihilation of the vortex followed by nucleation of a new vortex under conditions that impose the desired handedness. The contrasting method of chirality control via spin transfer torque in a spin valve nanopillar was introduced, as well as an experiment supporting its viability, setting the stage for Chapter 6. After excitation, coherent relaxation of the magnetization generally involves the formation of spin wave eigenmodes. The final section of this chapter discussed eigenmodes with azimuthal and radial symmetries that often form in vortex-state disks near equilibrium. Analysis of radial eigenmodes formed in the free layer of a spin valve nanopillar is presented in Chapters 7 and 8, with an emphasis on deviations from the models discussed here.

Chapter 6

Chirality control

This analysis chapter is the first of three to discuss inquiries motivated by the topics of Chapter 1 and informed by the theoretical and experimental backgrounds of Chapters 2–5. All three concern numerical simulation of the Landau Lifshitz equation for magnetization dynamics in a spin valve nanopillar excited by spin transfer torque. After an introduction to the nanopillar system, the anatomy of chirality switching by spin transfer torque is presented with attention to experimental observables and internal energies. Then, novel switching diagrams covering the excitation current pulse phase space are used to characterize a range of impulse response processes. This forms the context for two subsequent results chapters, which cover magnetization relaxation, frequency domain properties, and the role of interlayer coupling in the dynamics. Some results in this chapter were published in Refs. [179] and [177].

6.1 Equilibrium configuration

The system under examination is a circular spin valve nanopillar with radius $R =$ 50 nm, cobalt polarizer ($L_{\mathrm{Co}} = 20$ nm), copper spacer layer ($L_{\mathrm{Cu}} = d$) and permalloy

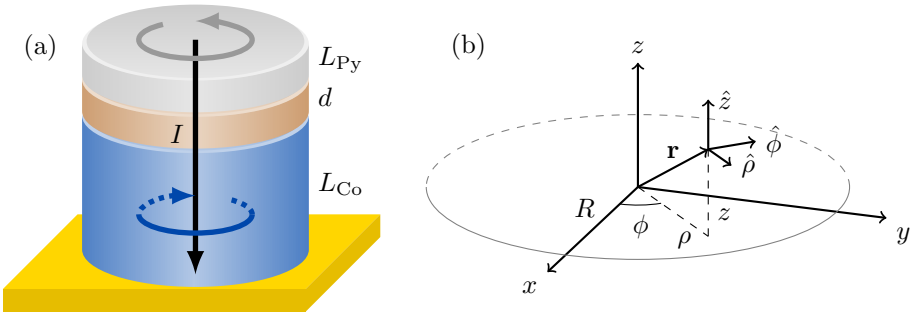

Figure 6.1: (a) Schematic nanopillar with in plane magnetizations (colored arrows), current direction (black arrow), and layer thicknesses indicated. (b) Position vector of a cell centered at $\mathbf{r} = (\rho, \phi, z)$ and the cylindrical magnetization basis in that cell.

(Py = $Ni_{80}Fe_{20}$) free layer ($L_{\mathrm{Py}} = 5$ nm), where d varies from 1 to 25 nm. By necessity, d is much less than the spin diffusion length in copper, which varies from several hundred nanometers to about 1 µm [62]. We consider only the dual vortex ground state with parallel positive core polarities and left-handed Co, so in the following parallel and antiparallel refer to the nominal (Equation 3.1) relative chirality of the pillar.

The system is discretized on a regular finite difference mesh with (2 nm × 2 nm × L) cells in each layer, and its time evolution via Equations 4.7 and 4.19 is calculated using the LLG Micromagnetics Simulator developed by M. R. Scheinfein [196]. Within each magnetic layer the reduced magnetization $\mathbf{m}(\mathbf{r})$ is azimuthally symmetric and independent of z, so in the cylindrical disk basis $\mathbf{r} = (\rho, \phi, z)$, the vector $\mathbf{m}(\mathbf{r}) = \mathbf{m}(\rho) = (m_\rho, m_\phi, m_z)$ (Figure 6.1(b)). Switching the free layer chirality over the range of d requires current densities from 1.5×10^8 to 8.4×10^8 A/cm^2 (I from 12 to 66 mA) for pulse widths τ from 50 to 200 ps. Currents travel along $\pm\hat{\mathbf{z}}$ and are uniformly distributed in the ρz plane in $\rho < R$. The pulses have 2 ps rise and fall times, and in the following time t is referenced to the start of the pulse. Relevant micromagnetic parameters are given in Table 6.1.

Spin transfer requires an angle included by magnetizations sequential along the direction of current (Section 4.2) [106]. In this system the interlayer dipole field and asym-

Layer	Parameter	Notation	Value	Units
Py	Saturation magnetization	M_s	800	$\mathrm{emu\,cm^{-3}}$
	Exchange stiffness	A	1.05×10^{-6}	$\mathrm{erg\,cm^{-1}}$
	Resistivity	—	8.6	$\mu\Omega\,\mathrm{cm}$
	Spin polarization	P	0.26	—
Cu	Resistivity	—	5.8	$\mu\Omega\,\mathrm{cm}$
	GMR Ratio	—	0.25	—
Co	Saturation magnetization	M_s	1400	$\mathrm{emu\,cm^{-3}}$
	Exchange stiffness	A	3.05×10^{-6}	$\mathrm{erg\,cm^{-1}}$
	Resistivity	—	5.8	$\mu\Omega\,\mathrm{cm}$
	Spin polarization	P	0.40	—
—	Gyromagnetic frequency	γ	1.76×10^{7}	$\mathrm{Oe\,Hz^{-1}}$
	Damping constant	α	0.01	—

Table 6.1: Material properties and micromagnetic parameters.

metry of the magnetic layers provides such an offset. Essentially, the fringing field of Co spreads out the Py core: The equilibrium vortex core radius R_c increases with the exchange stiffness A. Co is stiffer than Py, so in isolated disks the core radius is larger in Co than in Py. And since Co is magnetically harder, its stray field outweighs that of Py and imposes a measure of its divergence on $\mathbf{m}^\mathrm{Py}$. (The reciprocal effect is smaller but still significant.) The result is a somewhat wider but normally curling Co vortex and one considerably expanded and partially unwound in Py, and therefore a sizeable angular offset between the magnetizations.

These equilibrium features are summarized in Figure 6.2. In the free layer, $m_\phi^\mathrm{Py}(\rho) =$

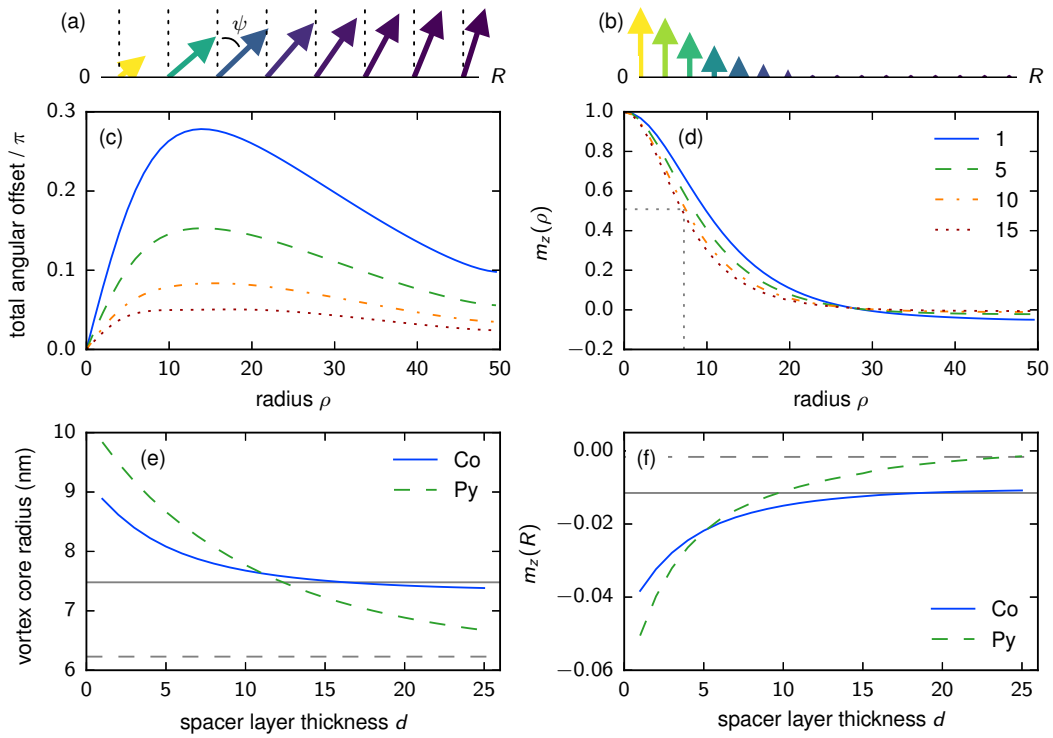

Figure 6.2: Effects of spacer layer thickness on the equilibrium state of the nanopillar. (a) In-plane projection of $\mathbf{m}^{\mathrm{Py}}$ at selected radii with the in-plane angular offset $\psi(\rho)$ indicated. The dotted lines give the magnetization direction of an ideal vortex. (b) Out of plane projection. (c) Total angular offset between the magnetizations along a radius for $d = 1, 5, 10$ and 15 nm, legend in (d). (d) As (c), but m_z^{Py}. The core radius for $d = 15$ nm and the corresponding value of $m_z(R_{\mathrm{c}})$ are connected by the dotted lines in the lower left corner. (e) Vortex core radius R_{c} in each magnetic layer for d from 1 to 25 nm. The horizontal lines indicate the core radii of isolated Co and Py disks having the same dimensions as the respective magnetic layers. (f) As (e), but the average out of plane magnetization at the edge of the disk.

$\phi + c[\pi/2 - \psi(\rho)]$ where $\psi(\rho)$ is the in-plane offset due to the polarizer. Nonzero $\psi(\rho)$ means that the radial component of the magnetization m_ρ is nonzero, in contrast with the ansatzes of Sections 3.1.3 and 5.3. In Figure 6.2(a), the direction of the in plane magnetization of the free layer along a radius (colored arrows) is compared to that of an ideal vortex ($\psi = 0$, dashed lines) for $d = 1$ nm. The color encodes $|m_z|$. The total angular offset $\arccos(\mathbf{m}^{\mathrm{Co}} \cdot \mathbf{m}^{\mathrm{Py}})$ is shown in (c) for four values of d in the parallel state, decreasing in amplitude as the interlayer coupling decreases. In both layers, m_z has the usual centered, nearly gaussian profile, with core radius $R_{\mathrm{c}} \approx l_{\mathrm{ex}}$ and a small negative component at the edge. The out of plane component corresponding to (a) is shown in (b), and the core profiles for the systems in (c) are shown in (d). The dotted lines in the lower left corner of (d) give the core radius and corresponding value of $m_z(R)$ for $d = 10$ nm. Note that interlayer coupling obviates the shallow dip around the core present in an isolated disk (cf. Sections 3.1.3 and 5.1). The variation of R_{c} with d is given for both layers in (e), showing the greater influence of the Co stray field, with the core radii of vortices in isolated disks of the same dimensions as the magnetic layers given by the horizontal lines. The out of plane component at the edge is also nonzero in both layers (f), unlike an ideal vortex, a product of the relatively large ratio R_{c}/R for a nanometric disk.

6.2 Switching process

During the pulse, the current contributes energy to the system via two mechanisms. Foremost is the spin transfer torque, which depends on the angle between the magnetizations and therefore changes in magnitude and direction as the magnetizations evolve. Secondary is the curling current induced Oersted field. It typically contributes $< 1/10$ of the torque due to spin transfer, but is always oriented to assist in switching the free layer. Like the

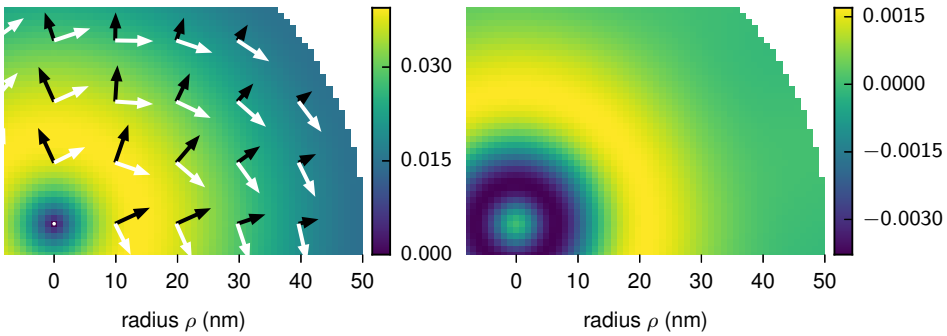

Figure 6.3: Reduced spin transfer torque in the free layer $g_\tau[\mathbf{m}^{\mathrm{Py}} \times (\mathbf{m}^{\mathrm{Py}} \times \mathbf{m}^{\mathrm{Co}})]$ at the onset of the pulse for initially parallel chiralities and $d = 3$ nm. (a) Radial component. Black arrows correspond to the in-plane spin transfer torque, color to the magnitude of the radial component, and white arrows give the direction of the magnetization. (b) Magnitude of the out of plane component.

initial configuration, both are axisymmetric. Figure 6.3 shows the (a) radial and (b) out of plane components of the reduced spin torque in the free layer $g_\tau[\mathbf{m}^{\mathrm{Py}} \times (\mathbf{m}^{\mathrm{Py}} \times \mathbf{m}^{\mathrm{Co}})]$ (Equation 4.19) at $t = 2$ ps for $d = 1$ nm in the parallel state. Since the cores share polarity and are aligned, there is no angular offset in the center, and demagnetization limits the offset at the edge by aligning the magnetizations nearly tangent to the edge, so the torques at $\rho = 0$ and $\rho = R$ are minimal. The majority of the spin torque is oriented radially in the annular region of Figure 6.2(c), increasing from the vortex core and tailing off toward the the disk edge. The smaller out of plane component in the core halo acts to expand $R_{\mathrm{c}}^{\mathrm{Py}}$ in the parallel case and vice versa. Spin transfer amplitudes in this system increase until $\theta \approx 0.56\pi$ and then approach zero as $\theta \to \{0, \pi\}$ in accordance with Equation 4.20.

An example of parallel to antiparallel switching is shown in Figure 6.4 ($d = 5$ nm). The left column shows the in-plane projection of the free layer magnetization, the right the out of plane component. At the onset of the pulse (top row), the configuration corresponds to the dashed lines in Figure 6.2(c) and (d). As spin torque unwinds m_ϕ, Figure 6.4(c)

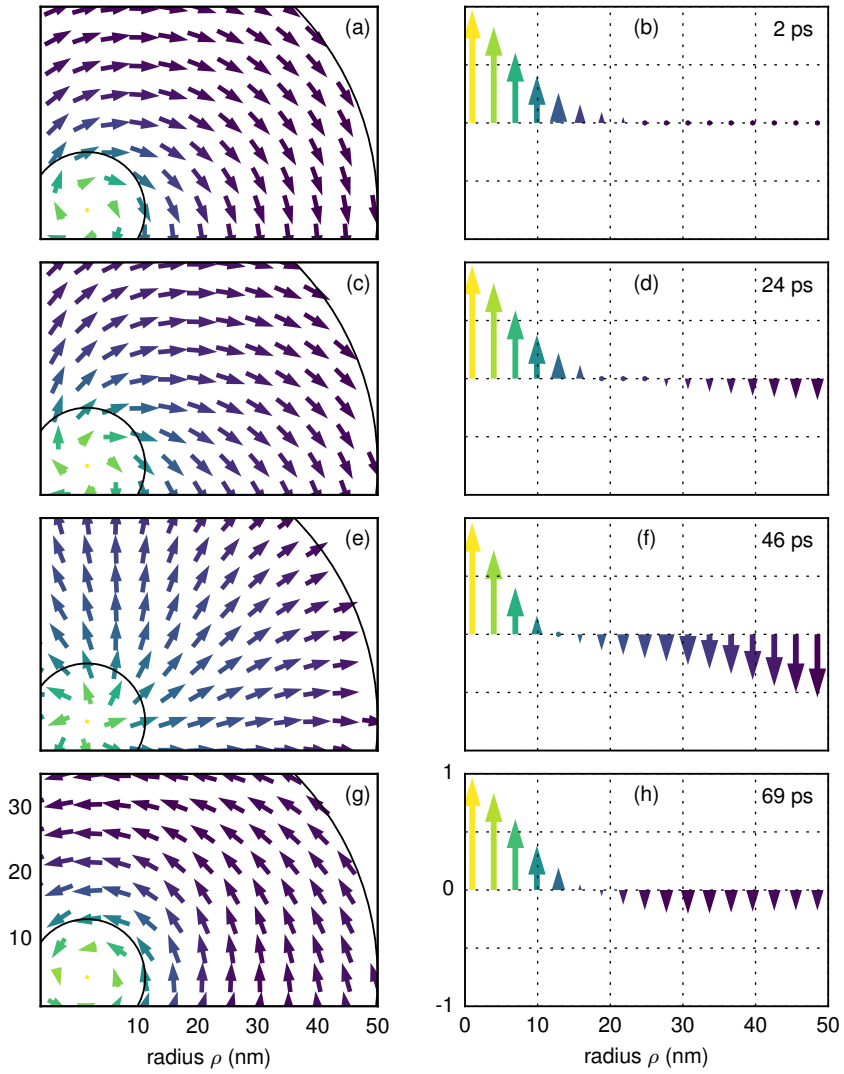

Figure 6.4: In-plane projection (left column) and out of plane component (right) of the free layer magnetization in select cells during chirality switching (initially parallel, d = 5 nm). The axis labels in the bottom row apply to each panel in their respective columns. $\rho = 10$ nm and the disk radius are indicated with black lines in the left column.

and (e), the edge magnetization rotates out of plane and the core compresses, (d) and (f). Then the magnetization quickly curls into the opposite handedness, and the deviations in m_z propagate out from the core and in from the edge (g–h).

In an idealized process, the exchange energy is invariant under a global rotation of m_ϕ and only demagnetization energy changes [77]. Here however m_z is time dependent and both exchange and demagnetization energies vary during switching. As the in plane projection of the free layer magnetization is driven through the curl-free hedgehog configuration $m_\rho^{\mathrm{Py}} \approx 1$, Figure 6.4(e), the increased edge pole density drives the systemic demagnetization energy over its maximum. Exchange oscillates nearly in antiphase with demagnetization energy in coherent rotation, having local maxima in the ground states. In a typical coherent case systemic demagnetization energy more than doubles during the switching process while exchange varies about 15%.

With parallel (antiparallel) initial chiralities, the pillar is in the low (high) resistance state (Section 3.2.2). In the first few picoseconds, the rate of rotation of the free layer and thus the rate of change of the resistance is proportional to the amplitude of the current pulse, consistent with Equation 4.19; then, the increasing angle between the magnetizations increases the spin transfer efficiency and the rotation accelerates. In the ideally coherent case, pillar resistance as a function of time follows a sigmoid curve, diverging from its initial value until $m_\rho^{\mathrm{Py}} \approx 1$ and then approaching its final value. Figure 6.5 shows resistance signals for four simulations with pulse amplitudes $I = 30.0$ mA (3.8×10^8 A/cm^2), pulse widths $\tau = 52.5$, 62.5, 107.5, and 197.5 ps, and intially parallel chiralities. The dashed horizontal line indicates the resistance of the divergent transition configuration, Figure 6.4(e–f). Each begins with rapid increase as the free layer vortex unwinds. After each pulse cuts off (black circles), the trajectory of the magnetization is subject only to damping and gyroscopic torques. The magnetization may rewind to its original chirality (dotted line) or continue

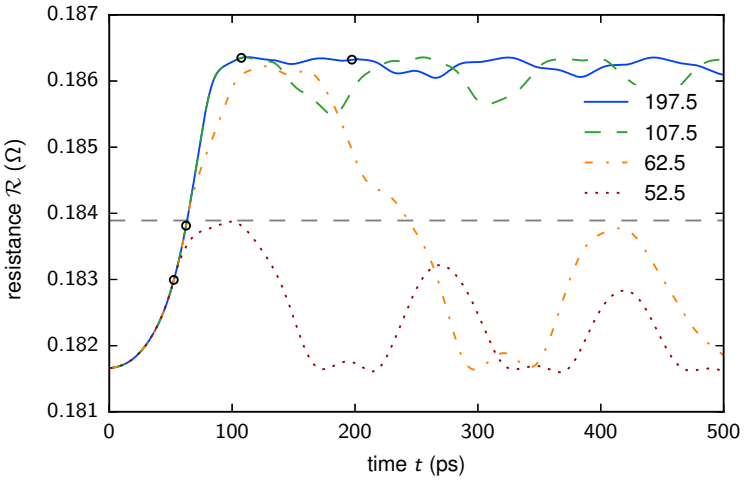

Figure 6.5: Resistance versus time for 30.0 mA pulses with widths $\tau = 52.5$, 62.5, 107.5, and 197.5 ps indicated by black circles. The dotted grey line is the resistance of the pillar with magnetization pointing radially out in the free layer. Despite only 10 ps separating the $\tau = 52.5$ and 62.5 ps pulse widths, the systems switch zero and twice respectively. Comparing the 107.5 ps and 197.5 ps signals (dashed and solid lines respectively), the continued spin transfer of the latter contributes an effective damping toward the antiparallel configuration, reducing the ringing after switching. (Initially parallel, $d = 5$ nm.)

its rotation (dot-dashed), but if the configuration is far from a ground state at the end of the pulse, the coherence of the vortex and integrity of its core are at risk (Section 6.3).

For low amplitude pulses, if the energy input is not sufficient to overcome the barrier between chirality states within about 75 ps, half the period of the impulse response oscillation (ringing), demagnetization acts to rewind the vortex. For intermediate inputs and longer pulses, either energy accrues, with the oscillation growing in amplitude until switching occurs, or the free layer magnetization rings with decaying amplitude about a slightly unwound state until the pulse cuts off. This extends to the dc case: a $d = 3$ nm pillar subject to a continuous 6.4×10^7 A/cm^2 switches after 2.5 ns of growing precession, about 16 periods at 6.4 GHz, and then damps out over an additional five cycles. However, a stable torsional oscillation cannot be generated by a subcritical dc current without unrealistic fine-tuning of the current amplitude.

After switching, the magnetization precesses nearly in the ρz plane, with an azimuthal component proportional to $\psi(\rho)$. The decay of the ringing depends on the configuration at the pulse cutoff, both its overall coherence and chirality relative to the new equilibrium state. If the pulse extends past switching and into the ringing, it contributes an effective damping, evident in the suppressed amplitude of the $\tau = 197.5$ ps signal after switching compared to the 107.5 ps case in Figure 6.5. This damping torque rotates the magnetization in the direction of the true parallel or antiparallel configuration rather than the new equilibrium, which are dissimilar when $\psi(\rho)$ is nonzero. The discrepancy can lead to an additional step response at the end of the pulse. Details of the relaxation process for $t > 500$ ps are discussed in Chapter 7.

6.3 Switching diagrams

Ranges of current densities and pulse widths affect switching. Switching diagrams in the literature are generally binary maps in $I-\tau$ parameter space, but useful details can be revealed by diagrams of continuous quantities that evolve in time. Maps of device resistance $\mathcal{R}$ show switching speed as well as ringing amplitude over the parameter space, and can be annotated with filters for coherence, polarity, and number of switches. Comprehensive switching diagrams have been constructed for $d = 5$ nm, for both initial chiralities. The balance of this section is dedicated to these datasets. Specific regions were also explored for $d = 10$, 15, and 20 nm with parallel initial chirality; these simulations are discussed in Section 6.4.

To select the cutoff time for the simulations, we inspected of 320 runs of length 1.0 ns, spanning $16 \leq I \leq 50$ mA between $\tau = 40$ and 120 ps and 16 to 21 mA between 120 and 260 ps, as well as a sparser grid of longer for each combination of 10 mA, 50 ps

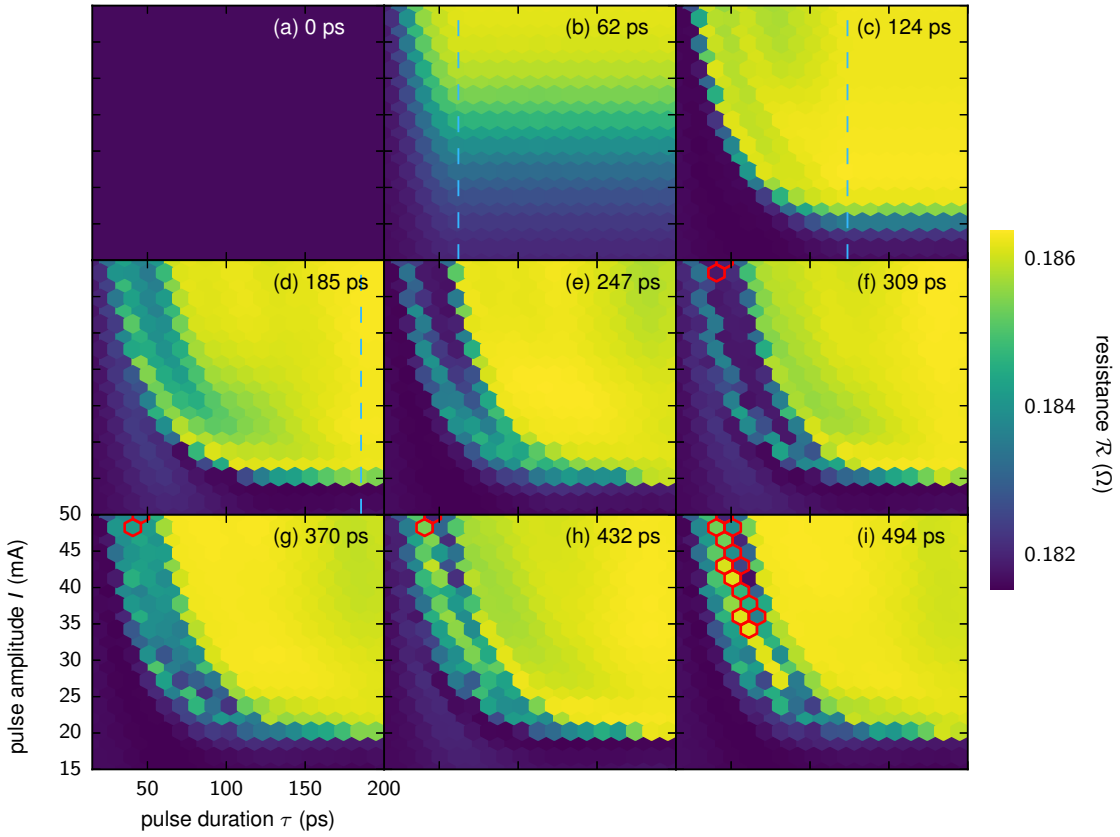

Figure 6.6: Resistance $\mathcal{R}$ at select times for simulations spanning pulse durations $15 \leq \tau \leq 200$ ps and amplitudes $15 \leq I < 50$ mA ($d = 5$ nm). Bins outlined in red contain at least one simulation where $m_z(\rho = 0) < 0$ at some time preceding that frame. (a) All systems have initially parallel chiralities and therefore low resistance. (b) After 62 ps have elapsed, the free layer has unwound to a degree depending on the pulse amplitude, increasing $\mathcal{R}$. (c) Most systems assume the high resistance antiparallel configuration. A clear energy curve emerges that separates switching from non-switching regimes. (d–f) On either side of the demarcation, ringing occurs. A third unstable region emerges in which some simulations switch back to parallel. (g–i) Switching and non-switching regions relax, the unstable region continues to ring, and some systems switch a third time.

increments over the same current range with 50 to 500 ps pulse durations. In every case, $\mathcal{R}$ at $t = 0.5$ ns was closer to its eventual limit than its initial value before $\tau = 420$ ps. No system in the parameter space switched more than three times. This does not entirely ensure that the final frame represents the final state of the system, but we found no pathological cases.

Figure 6.6 shows resistance in nine sequential frames for 2242 simulations spanning pulse durations $15 \leq \tau \leq 200$ ps and amplitudes $15 \leq I < 50$ mA. Each bin represents the mean resistance of three to eight simulations, each with a unique combination of I and τ. Time in picoseconds is indicated in the top right of each frame. The blue line in select frames marks $t = \tau$; pulses in simulations to the left of the line have cut off by that frame and vice versa. Initially in the parallel relative chirality configuration, all systems are in the low resistance state in (a). As time progresses, the free layer unwinds, increasing the angle between magnetizations and therefore pillar resistance. As systems assume the high resistance antiparallel configuration, the boundary between critical and subcritical regimes sweeps downward, switching speed being proportional to pulse amplitude, revealing switching and non-switching regimes (b–c). The boundary curve is proportional to pulse energies $I^2\tau$. Proximally on either side, large amplitude ringing occurs. An intermediate unstable region emerges in which some simulations switch back to parallel (e–f), in the manner of the 62.5 ps simulation in Figure 6.5. While the majority of systems relax into a final configuration, the unstable region continues to ring, and some systems switch a third time (g–i). Bins outlined in red contain at least one simulation where the out of plane magnetization at the center of the disk changed sign at some time preceding that frame. Many of these are simulations like the one represented by the dot-dashed line in Figure 6.5, where the free layer configuration was mostly unwound at the end of the pulse, then, without the stabilizing influence of the spin torque, over-rotated through the opposite handedness

and rebounded almost as a torsion spring.

6.4 Spacer thickness dependence

A full set of switching diagrams for d from 1 to 25 nm is beyond the scope of this work, but subsets of the parameter space were explored in the preparation of Chapter 8. These surveys yielded the switching diagrams in Figures 6.7 – 6.9 and several qualititative guidelines for optimization. First, the stabilizing influence of the polarizer's field diminishes with increasing d. Second, larger current densities are required for thicker spacers because $\langle\psi(\rho)\rangle$ decreases as well. The implications:

(1) With increasing d, the pulse regime for successful single switching shrinks.

(2) Out of plane excursions at the edge during switching propagate radially inward; if the free layer vortex is insufficiently stabilized by interlayer coupling, these waves can inundate the core entirely. The bins marked in red in Figures 6.6 – 6.9 contain one or more simulations where $m_z(\rho = 0)$ changed sign, indicating a polarity flip, dissolution of the vortex, gyrotropy, or other nonlinear event.

(3) Short, high amplitude pulses (e.g. 60 mA, 80 ps) generally incur more incoherence after the cutoff than longer, lower ones (48 mA, 200 ps). Local inhomogeneities tend to relax quickly through short-wavelength spinwaves. Dissimilarly, two long-wavelength conditions prolong relaxation and can provoke additional switches: ρ dependent m_ϕ, for example when magnetization in the annular region of peak spin torque rotates more rapidly than the magnetization at the edge, and broken symmetry of the vortex's confining potential, which can lead to extended gyrotropic motion of the vortex core.

(4) When d exceeds 20 nm, switching without polarity flips and other undesirable behaviour (in the context of Chapter 1) is improbable and requires trial-and-error fine

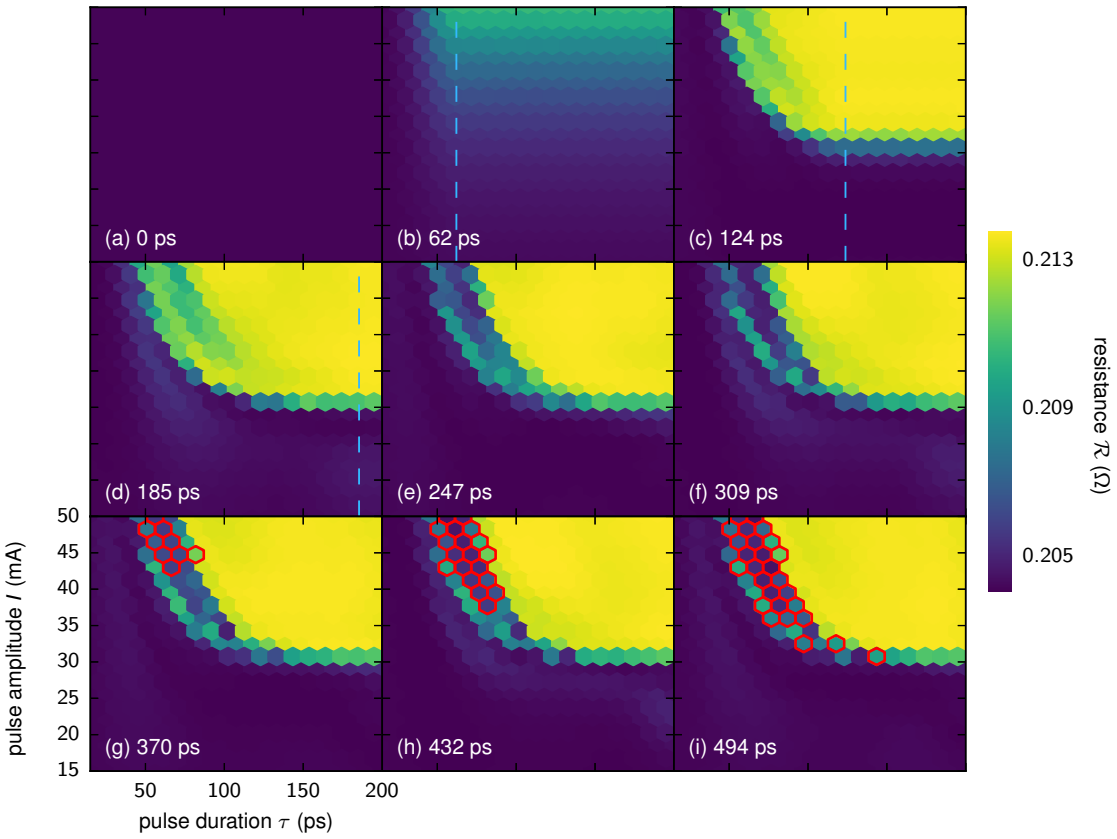

Figure 6.7: As Figure 6.6, but for $d = 10$ nm.

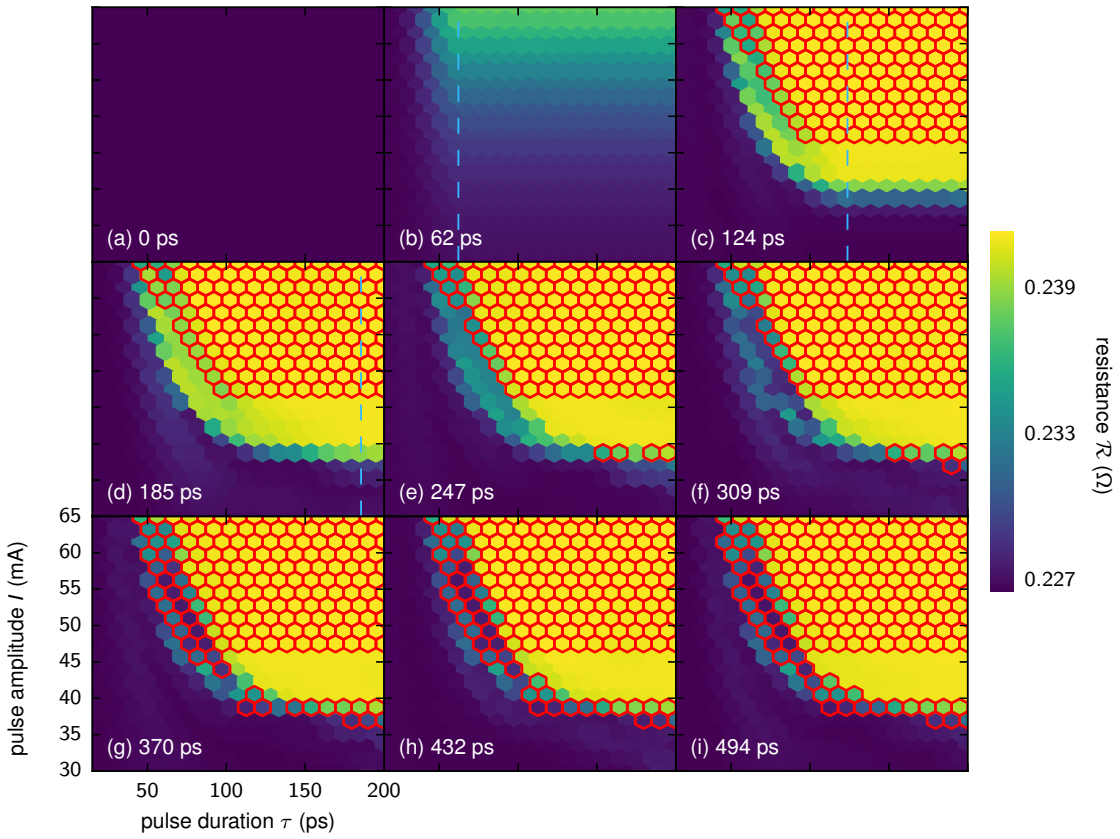

Figure 6.8: As Figure 6.6, but for $d = 15$ nm. Note change in y axis range.

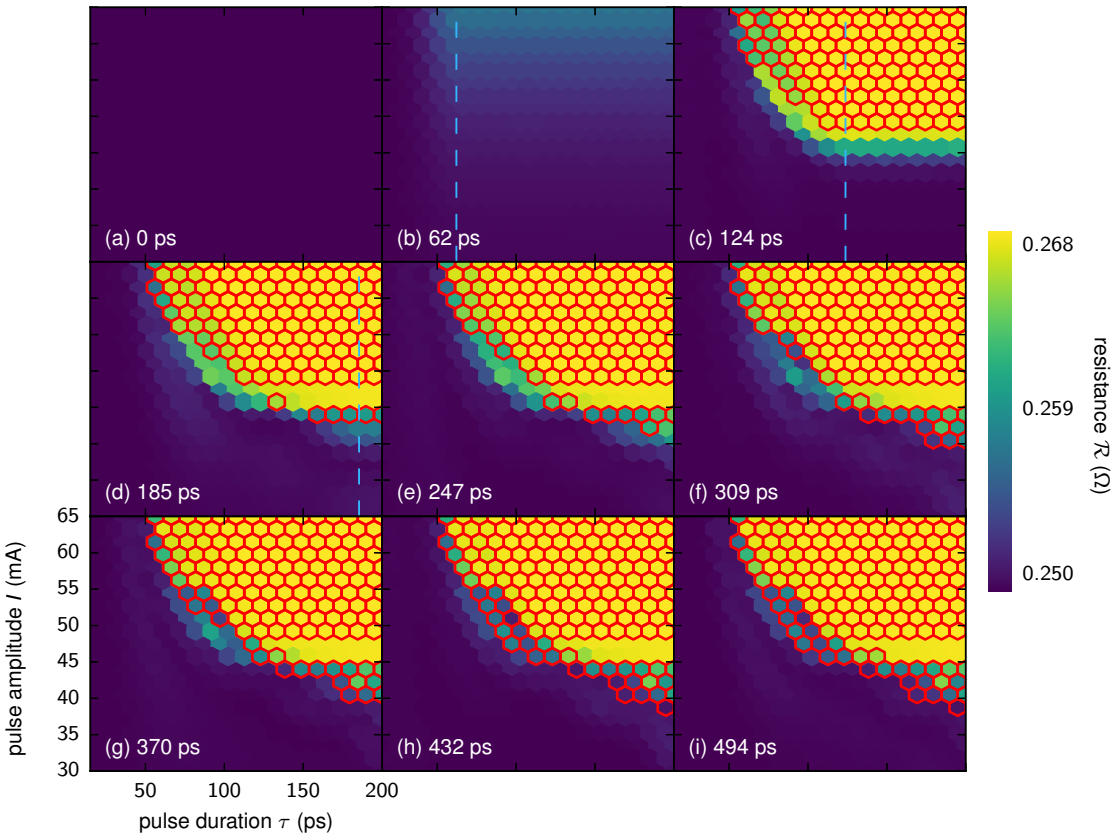

Figure 6.9: As Figure 6.8, but for $d = 20$ nm.

tuning of the pulse. Approximately 37% of simulations with $d = 20$ nm met the condition to be flagged with a red bin in Figure 6.9.

6.5 Summary

Switching the free layer chirality with spin transfer torque in a circular spin valve nanopillar is a fast, repeatable, and compact approach to single bit manipulation. Switching times are deep subnanosecond, competitive with polarity control processes. This method is considerably faster than gyrotropic chirality switching when relaxation is taken into account, and more straightforward to fabricate due to uniform layer thicknesses. The required current densities are accessible in the lab and reasonable from a Joule heating standpoint, and the all-current chirality control method requires less auxiliary circuitry than field-driven counterparts. For spacer layer thicknesses on the order of the magnetic layers' exchange length, a wide range of current pulse parameters affect switching. Pulses that persist after switching contribute an effective damping that stabilizes the final chirality state and reduces ringing. Due to the stability of the fixed layer, the pillar magnetoresistance serves as an accesible proxy for the relative chirality of the magnetization configuration. Vortices in pillars with thicker spacers require larger current amplitudes to excite, are less stabilized by interlayer dipole coupling, and exhibit less coherent dynamics, leading to a reduction of the successful switching pulse parameter space with increasing spacer thickness.

Chapter 7

Eigenmodes

Whereas the preceding chapter concerned chirality switching over tens of picoseconds and the dynamics of the first few precessional cycles thereafter, this chapter concerns magnetization relaxation processes spanning several nanoseconds after excitation. At this stage, any short-wavelength transients in the magnetization have calmed and only the magnetostatic modes remain, from 0.5 (the last panel of Figure 6.6) to 5.0 ns after the start of the pulse, where the period of the major oscillation is approximately 150 ps. As in the previous chapter, we refer to the layer resolved reduced magnetization $\mathbf{m}(\mathbf{r}) = \mathbf{m}(\rho) = (m_\rho, m_\phi, m_z)$ (Figure 6.1). During relaxation, the configuration of each layer reduces to a static vortex and a small angle deviation about it, $\mathbf{m}(\rho) = \mathbf{m}_0(\rho) + \boldsymbol{\mu}(\rho, t)$, where the dynamic magnetization $\boldsymbol{\mu}(\rho, t) = (\mu_\rho, \mu_\phi, \mu_z)$ is comprised of spin wave eigenmodes over the ground state $\mathbf{m}_0$ (Section 5.3). The configuration remains coherent and azimuthally symmetric about a centered vortex, so for taxonomy we need only the mode index n, the number of radial nodes between the core and edge, with, e.g., μ_{z1}^{Py} the notation for the z component of the Py $n = 1$ eigenmode. Data presented in this chapter are representative of both relative chiralities and all values of d unless otherwise indicated; variation with these parameters is

the subject of Chapter 8. The simulation methods are unchanged from Chapter 6 except for in plane cell dimensions reduced to (1×1) nm. Results from this chapter were published in Ref. [197].

7.1 FFTs

7.1.1 Fourier spectra

As in Chapter 6, the main observables are device resistance $\mathcal{R}$ and layer-resolved magnetization. Of the dynamic components, μ_z is most often measured experimentally and treated analytically. Radial magnetization μ_ρ is next-most prevalent because relaxation precession occurs in the ρz plane in isolated disks. Precession in m_ϕ, the cellwise chirality, is significant when $\psi(\rho)$ is substantial and is found in the same core halo region (Section 6.2). Figure 7.1 shows that the spectra of all three components are highly covariant with one another, indicating strong coupling between components. The first peak at 8.90 GHz ($d =$ 7 nm) is evident in all components of both layers, with m_z^{Co} suppressed in the power spectrum by 20 dB compared to μ_z^{Py}. It is fundamentally a Py mode, and the measureable oscillation in Co is induced via interlayer coupling. This distinction is substantiated in Section 7.1.2.

Giant magnetoresistance follows from an angular offset between sequential magnetizations along the direction of current (Section 3.2.2). Therefore the time evolution and Fourier spectra of m_ϕ^{Py} and $\mathcal{R}$ are strongly covariant because m_ϕ^{Co} is comparatively static, as illustrated in Figure 7.2(a–c). Based on the discussion of core and edge dynamics in Section 6.2, we expect spectra for the internal energies of the pillar to be similar. Systemic demagnetization and exchange energies were extracted from the same simulation and the associated FFTs are shown along with that of the pillar-averaged magnetization in

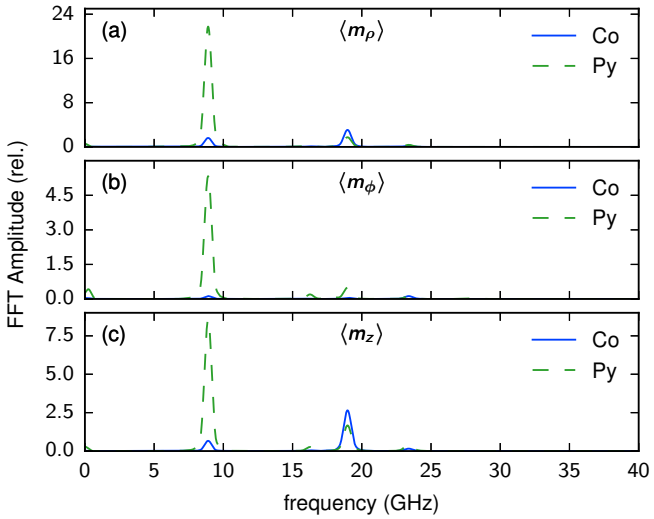

Figure 7.1: Fourier spectra of component resolved, layer averaged magnetization (parallel relaxation, $d = 7$ nm).

Figure 7.2 (d–f). Compared to the spectrum of $\mathcal{R}$, which closely follows Py, the energies mimic the Co spectrum in (a) because Co carries greater weight in these systemic measures: in dynamic exchange due to its higher exchange stiffness, in demagnetization due to its relative hardness, and in pillar averaged magnetization due to the polarizer's bulk. As expected, the covariance of all three spectra is significant: exchange and demagnetization energies oscillate at the same frequency in each mode, driven by and shaping the dynamic magnetization.

7.1.2 Eigenmode maps

Cellwise transforms reveal azimuthally-symmetic eigenmodes during relaxation (Section 5.3). The fundamental mode in the Py layer (Figure 7.3) has zero amplitude at the core and a profile that differs in each component. The ρ component (a, b) is broadly peaked outside the core and has a large edge amplitude. The low-amplitude ϕ component (c, d) is peaked in the core halo region, with antinode width proportional to the equilibrium

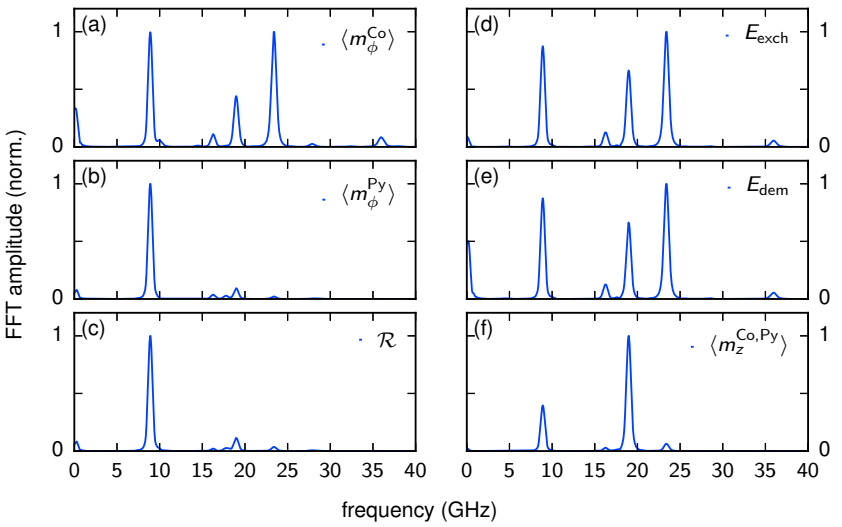

Figure 7.2: (Left column) Fourier spectra of layer chiralities $m_\phi^{\mathrm{Co,Py}}$ and pillar resistance $\mathcal{R}$ from the same simulation as Figure 7.1. Modes and induced oscillations in Co carry similar weights; Py is dominated by its $n = 0$ mode and $\mathcal{R}$ follows as explained in the text. (Right) Fourier spectra of exchange and demagnetization energies and pillar-averaged z component of magnetization.

offset $\psi(\rho)$ (Section 6.2), and falls off at the edge where $\psi(\rho)$ is minimal. The z component (e, f) has a broad antinode peaked outside the core radius with a shallow minimum near $\rho = 40$ nm and a large amplitude at the edge similar to that of the ρ component. $\boldsymbol{\mu}_0^{\mathrm{Py}}$ is found at 8.0 GHz for $d = 5$ nm in parallel relaxation. At the same frequency, the Co layer FFT shows a sympathetic oscillation with the same antinode position and a smaller edge amplitude (Figure 7.4(a) and (b)). It typically has the second heaviest spectral weight of the Co oscillations after the $\boldsymbol{\mu}_0^{\mathrm{Co}}$ mode near 20 GHz. Higher order modes in Py have additional antinodes and retain a nonzero edge amplitude. Counting radially, the first antinode, in the core halo, is the most intense; this coincides with optical measurements of isolated disks [182, 193]. Modes with $n > 2$ can only be resolved in particularly coherent cases. At each frequency, the induced oscillation in Co has a matching maximum in the core halo region, one or more depressions, and a nonzero edge amplitude.

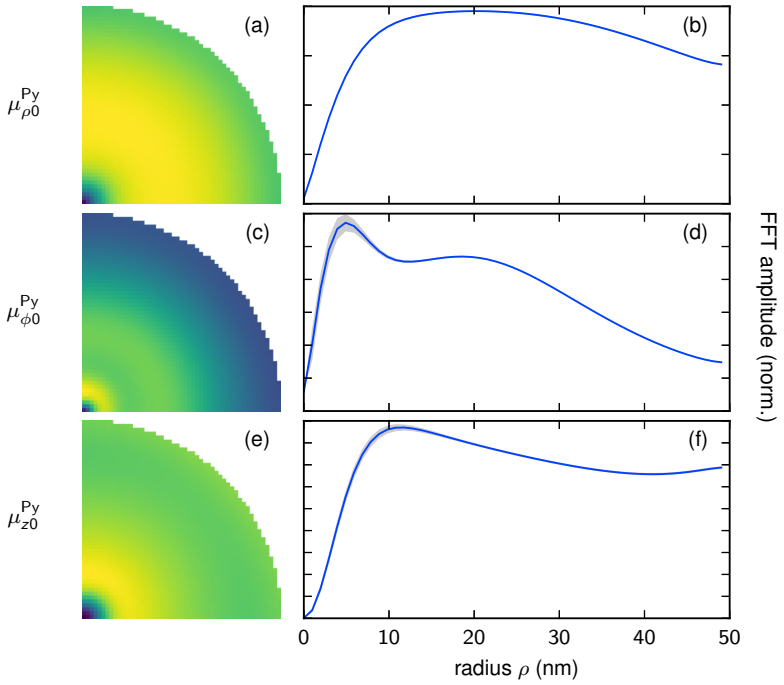

Figure 7.3: (Left column) Amplitude maps of each magnetization component of the Py $n = 0$ eigenmode and (right) their profiles from core to edge, each panel individually normalized. Each radial profile is the average of four linescans (at $\phi = 0, \pi/2, \pi$, and $3\pi/2$). The grey curves give the corresponding standard deviations, measures of the spatial coherence. (Antiparallel relaxation, $d = 10$ nm, 9.0 GHz.)

There also are three consistent modes in Co with counterpart oscillations in Py. The $n = 0$ mode shown in Figure 7.5(a) and (c) has the least distinctive core halo antinode – in some cases the amplitude increases smoothly from zero at the core to an antinode at the edge without any radial minimum. In contrast, the $n = \{1, 2\}$ modes closely resemble the corresponding Py modes. Induced oscillations in Py at each Co frequency are peaked in the core halo and decay to a nonzero edge amplitude (dashed curves in Figure 7.5(c), (f), and (i)), with considerable variation in radial profile between simulations. Figure 7.5(i) shows asymmetric distortion typical of the low amplitude, high frequency induced oscillations.

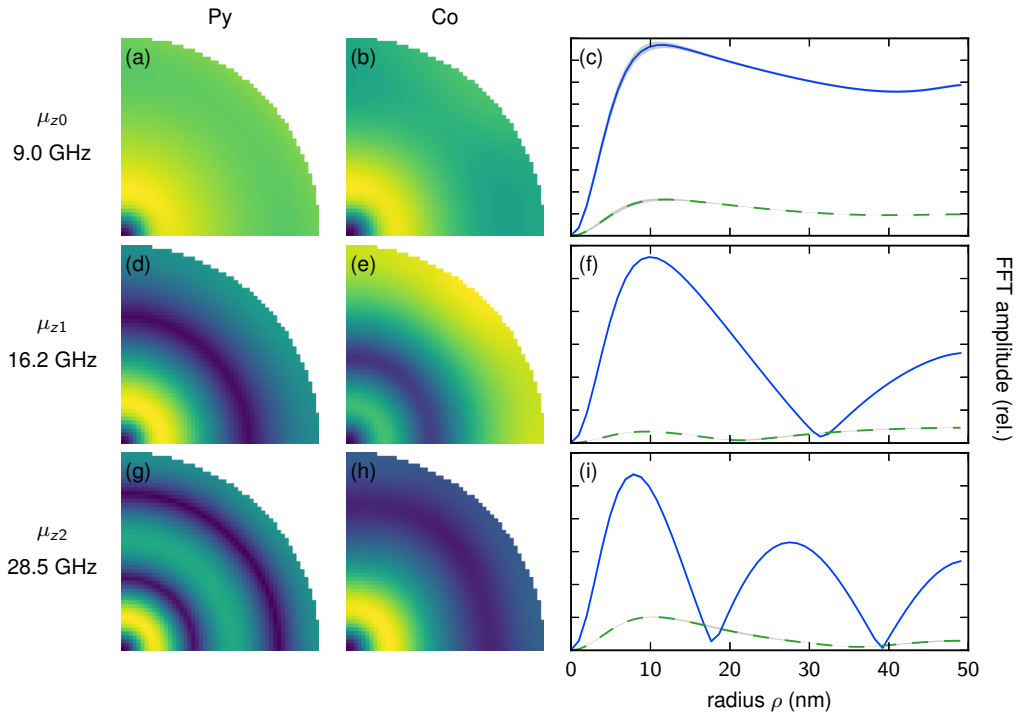

Figure 7.4: (Left column) Amplitude maps of the out of plane component of the Py $n = \{0, 1, 2\}$ eigenmodes and (center) the corresponding induced oscillations in Co. (Right) Profiles from core to edge for Py (solid line) and Co (dashed). (Same simulation as Figure 7.3.)

7.2 Intralayer phase

Intralayer phase measurements complete the characterization of the eigenmodes. For every mode, and most of the induced oscillations, the measured phase is stable between $t = 0.5$ and 4.2 ns, more than 22 periods of the lowest frequency mode.

7.2.1 Method

We use two techniques with different virtues to measure phase. The first is to take the arctangent of the imaginary and real parts of the signal FFT at every point, the angle counterclockwise from the positive real axis on the complex plane. This is computationally

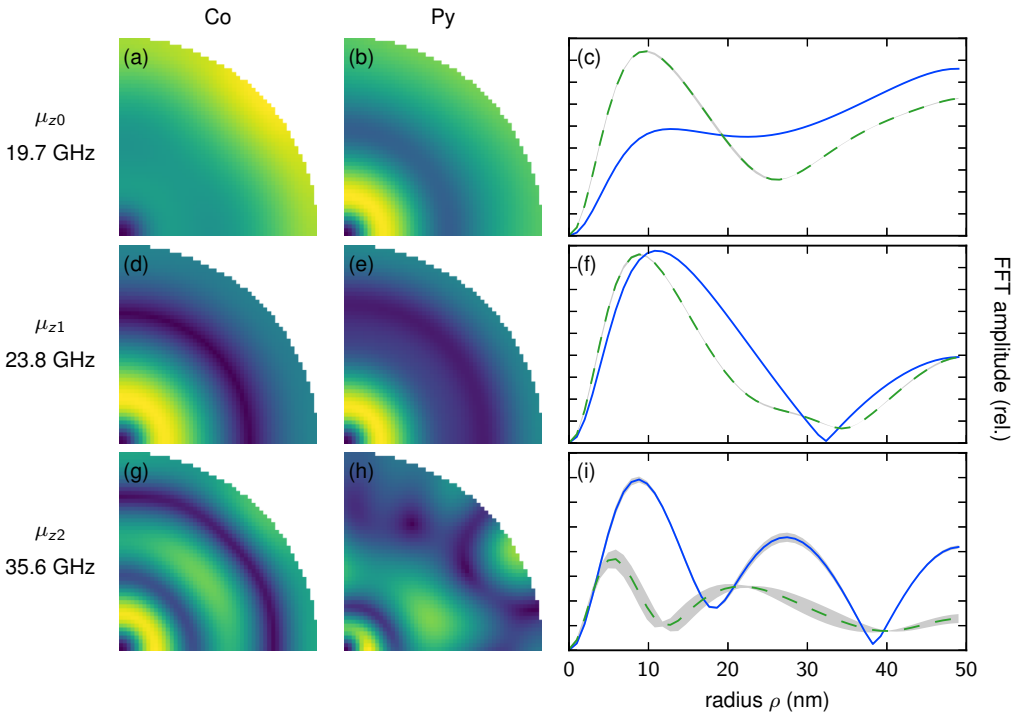

Figure 7.5: As Figure 7.4, but with Co modes in the left column and induced Py oscillations in the center. Right column: Co (solid lines) and Py (dashed) profiles.

efficient and works transparently with arrays of signals but returns a phase relative to the start of the FFT window, often introducing spurious shifts. The second is more expensive but more reliable. First, peaks frequencies in the FFT spectra are obtained and cached for each d and relative chirality. This is automated with cubic spline interpolation and peak finding using a continuous wavelet transform. Then the signal is bandpass filtered at the frequency of interest, either forward-backward with a digital infinite impulse response filter or with a gaussian filter in the frequency domain, then windowed in the time domain to remove the edge effects of the filter. A reference signal is chosen – e.g. the edge magnetization for a radial line scan or the average edge magnetization for a cellwise calculation – for which a functional representation is generated using cubic spline interpolation. Finally, the time shift is then calculated by least squares minimization of an error function whose

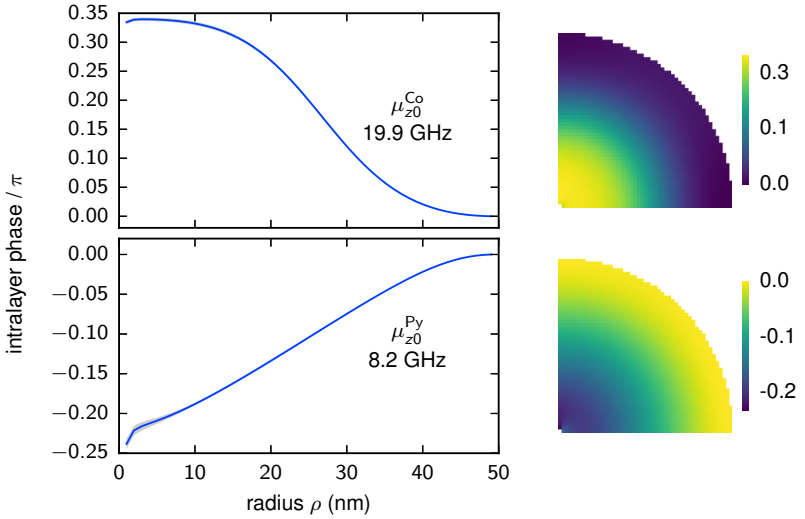

Figure 7.6: Phase measured in a filtered time series (left) and FFT phase (right) of Co (top) and Py (bottom) $n = 0$ modes. Antiparallel relaxation, $d = 6$ nm.

only fitting variable is the time shift between the reference function and filtered time series. We typically calculate the phase shift over several sample windows to test phase coherence over the course of relaxation.

7.2.2 Radial phase shifts

The Py $n = 0$ mode is essentially traveling, with phase increasing smoothly from edge to core (parallel relaxation) or core to edge (antiparallel). Evidently, primary oscillations in the core size or edge magnetization emit radial spin waves. This is a significant result: usually eigenmodes are taken to be standing waves, the superposition of equal amplitudes traveling in opposite directions. Modes with a single antinode are expected to oscillate totally in phase, and by definition antinodes in normal modes oscillate with fixed phase with respect to one another. These primary modes, however, are imperfectly standing with nonuniform phase. We know of no previous report of such structures.

The resulting in-plane projection is similar to the so-called sawtooth mode in Ref. [198] but is neither spatially uniform nor in phase throughout the disk. The Co $n = 0$

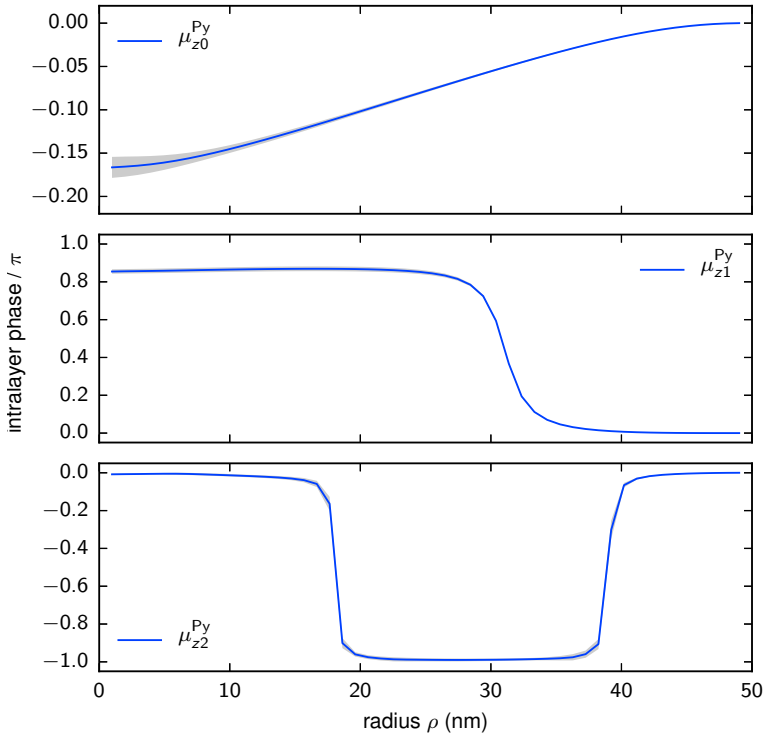

Figure 7.7: Intralayer phase of Py $n = 0, 1, 2$ modes for $d = 8$ nm in antiparallel relaxation. Bending near nodal lines instead of abrupt $\pm\pi$ jumps indicates quasi-traveling character.

mode phase is similar to the Py $n = 0$ in profile and amplitude in antiparallel relaxation, but in parallel relaxation it precesses virtually in phase throughout the disk. Both fundamental modes are shown in Figure 7.6, for antiparallel relaxation with $d = 6$ nm. Oscillations induced by the $n = 0$ modes always begin at the edge and radiate inward; the phase smoothly increases from the core to the edge over as much as a 0.8π shift. Thus in Py $n = 0$, antiparallel relaxation, waves in each layer travel in the same inward direction, and, with approximately linear phase along ρ, nearly constant speeds. Conversely, in parallel relaxation the waves in each layer propagate in opposite directions, and the phases vary nonlinearly with ρ. In particular, the phase of the induced oscillation in Co decreases steeply around the mode amplitude minimum, signifying that the traveling wave nearly

stalls before the region opposite the Py antinode flips almost in unison. This dependence on relative chirality will be explored further in Chapter 8.

The $n = \{1, 2\}$ modes in both layers are generally more consistent with convention. But in many cases, instead of abrupt phase shifts of $\pm\pi$ across nodes, we found bending near the nodes that indicates a traveling character superimposed on the standing modes. Nodes oscillate radially as much as 7 nm during precession in certain cases. The greater this fluctuation, the less abrupt the measured phase transitions across nodes. This effect is pronounced when d is small. Figure 7.7 shows phase relative to the edge magnetization. The shifts across the $n = 1$ node (middle panel) and $n = 2$ nodes (bottom panel) are spread over several cells. Also, there are differences with relative chirality. For the $n = 1$ mode in parallel relaxation, the antinodes oscillate with a $\pm\pi$ phase shift, as expected. However, in antiparallel relaxation, the phase shift is only 0.8π at $d = 1$ nm, increasing to 0.95π at $d = 25$ nm. (There is no qualitative difference in the mode amplitude profiles.) It is not clear why this is the case, but it appears in both the FFT and directly measured phases. And while the $n = 2$ mode in parallel relaxation has the expected shifts, in antiparallel relaxation it has a diminished phase shift in the central antinode. The diminished phase is consistent throughout relaxation, is not a result of averaging over spatial incoherence, and does not correspond to eigenfunctions with greater radial oscillation of the nodes.

7.3 Eigenfunctions

7.3.1 Novel eigenfunctions

Inverse Fourier transforms of the frequency components specific to the eigenmodes reveal the underlying structure of the eigenmodes. A striking difference to existing models (Figure 5.6) is that the edge is generally not a node for any projection of any radial mode.

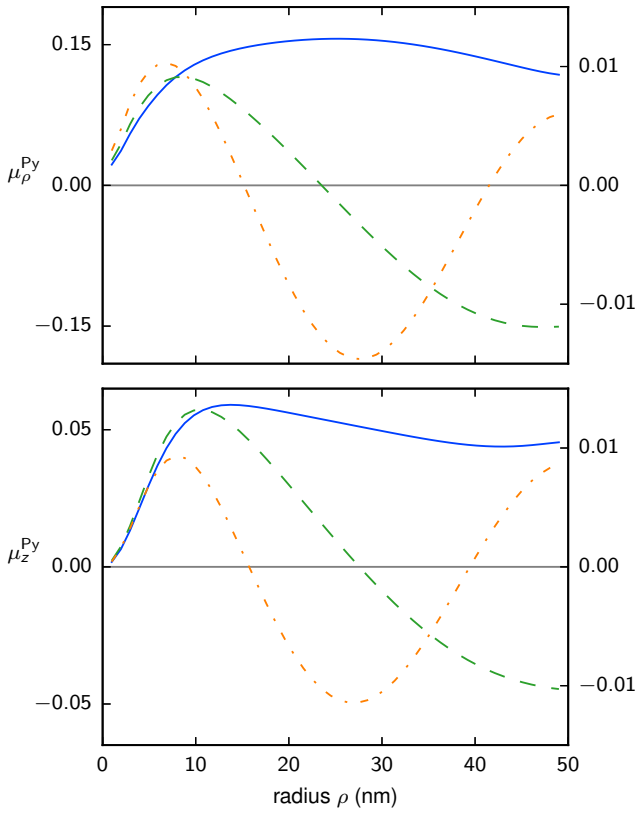

Figure 7.8: Eigenfunctions for Py $n = \{0, 1, 2\}$ ($d = 4$ nm, parallel relaxation). The left axes are for $n = 0$ and the right for $n = \{1, 2\}$.

In Figure 7.8, snapshots of the modes constituent of the dynamic magnetization $\mu_{\rho,z}^{\mathrm{Py}}$ are shown. Each curve is an instantaneous linescan from the core to the edge, obtained by filtering $\mu(\boldsymbol{\rho})$ at an eigenfrequency and finding the local maximum within a window, in this case between $t = 0.63$ and 0.80 ns. They can be compared to calculated eigenfunctions in the same manner as experimental data by considering the corresponding spatial FFT amplitudes (Figure 7.4) and phases (Figure 7.7). Previously reported radial modes have strong pinning at the edge, close to the thin disk approximation of Section 5.3. The radial functions in Figure 7.8, however, more resemble standing waves in an air tube with one closed end (the core) and one open end (the edge).

7.3.2 Discussion

The foremost analytical model for radial eigenmode spectra in isolated disks, see Ref. [193], gives us a qualitative interpretation of our results. To good approximation, the boundary conditions at $\rho = 0$ and $\rho = R$ and the aspect ratio L/R determine the mode profiles. Referring to Figure 7.8, we find the expected pinning of both components at the core: for L/R increasing from zero, pinning is weakened for the ρ component but for the z component remains strong. However, at the edge, we find large amplitudes in both the ρ and z components, the former of which is particularly unexpected. We checked numerically that the only ρ-dependence to the damping of the fundamental mode is that the core damps more quickly than the rest of the disk – there is no measured variation in the planar region $\rho > R_{\mathrm{c}}$.

We note several differences between our system and the cited analytical situation. (1) While the aspect ratio of our free layer ($L/R = 0.1$) is within the range usually considered, it is nanoscopic and therefore R_c is nonnegligible with respect to R. In this limit, exchange in the core region is important and core breathing is a significant contribution of dynamic magnetostatic and exchange energies. (2) $\psi(r)$ is nonnegligible in the ground state, so there are volume charges at equilibrium and ρ-dependence in $\mathbf{m}_0$. This complicates the expressions for $\boldsymbol{\mu}(\rho, t)$. (3) Nonuniform excitation: whereas radial modes in the literature are excited uniformly by perpendicular fields, these are excited with radial torques and the μ_z oscillations are essentially byproducts. Finally, (4) each layer is dipole coupled to another vortex state disk. There is no analytical model for high frequency modes in nanometric disks or vertically coupled vortex state disks, and the only related micromagnetic study, of a field-excited, interlayer exchange-coupled dual vortex nanopillar with a 1 µm radius, reported no atypical dynamics [195]. To our knowledge, the radial spectrum of the dual vortex nanopillar is an open issue.

A full study of dimension and aspect ratio dependence of these eigenmodes is computationally expensive and otherwise problematic: too small a radius and the switching energy exceeds that required to transition between metastable vortex and single domain configurations; larger radius or free layer thickness requires a larger current amplitude, increasing Joule heating and the circumferential Oersted field; a thicker free layer likewise requires more current to overcome its inertia as spin torque is an interfacial effect. A reasonable starting point would be one value of d, radius up to 200 nm, and fixed aspect ratio. This would not only connect the present study of mode structure to the size regime of existing single-layer models but also yield eigenmode frequency spectra to guide future extensions of those models to the nanometric regime or the spin valve geometry. We expect that the core size is increasingly significant with shrinking R [58], and we have shown here that in a small-radius nanopillar system, core dynamics dictate the fundamental mode of the free layer.

Condition (2) is a feature of the system and provides the angular offset necessary for spin transfer; its other chief effect is to suppress the equilibrium exchange energy. If $\psi(\rho)$ were zero, relaxation oscillations would occur in the ρz plane. In an analytical treatment, nonzero $\psi(\rho)$ would modify at least the ground state and the terms for the free layer dynamic demagnetization and exchange energies in the vortex core region, leading to d dependence according to Figure 6.2. However, we find that radial eigenfunctions with large edge amplitudes in the ρ and z components exist for all values of d. The radial position of the maxima in $\boldsymbol{\mu}_0^{\mathrm{Py}}(d)$ and the first antinodes in $\boldsymbol{\mu}_{\{0,1\}}^{\mathrm{Py}}(d)$ shift outward by a few nanometers for $d < 5$ nm, due to the increased core radius, but the relative edge amplitudes do not change with d. Evidently, modification of the free layer ground state does not lead to the diminished edge pinning, therefore condition (2) can be relegated, more important to excitation than relaxation.

Condition (3) is a feature of the spin transfer excitation, and its radial orientation and nonuniformity are determined by (2). There is no systematic study of uniform field excitation for nanometric disks or nanopillars for reference, but it can be tested without changing the other conditions by replacing the current pulse with a field pulse. We subjected a pillar with $d = 6$ nm in the antiparallel configuration to a spatially uniform, 1.0 kOe, 100 ps pulse aligned with the core polarities. The resulting mode frequencies and structures coincided qualitatively with those excited by spin transfer torque: like the current-induced case, the vortex core size oscillated and there was a nonzero amplitude at the edge. And, as expected, the FFT peak frequencies were insensitive to the excitation mode and consistent with determination by geometry. From this brief check, we can eliminate (3) as a driving factor in generating large edge amplitude eigenmodes.

Dynamic interlayer coupling is ruled out as a contributing factor for the same reason as condition (2), the insensitivity of mode profiles to varying d. This is consistent with the dynamic demagnetization field being strongest in the core region and diminished at the edges. However, we did find that mode frequencies strongly depend on the strength of the coupling, and this variation with d is addressed in Chapter 8.

In sum, the nanoscopic radius and consequential nonnegligible ratio R_c/R is the most viable explanation for the novel eigenmodes presented in this chapter. The dynamic vortex cores, typically neglected in analytical calculations of radial eigenmode spectra, modulate the dynamic demagnetization and exchange energies of the system, and oscillation of the core size is integral to the magnetization dynamics. Despite differences to previously reported modes, this conclusion is consistent with the established principle that boundary conditions shape not only equilibrium states but also high frequency processes in nanomagnets. In the context of Chapter 1, large edge amplitudes in the radial component of the magnetization may induce crosstalk in an array of nanopillars.

Chapter 8

Variation with spacer thickness and relative chirality

At the conclusion of the last chapter, we identified radial eigenfunctions with unusually large edge amplitudes and four potentially signficant differences between our case, an asymmetric nanopillar excited by spin transfer torque, and larger, field-excited, single layer systems with small edge amplitudes attributed to strong edge pinning. To recap, these four differences are (1) scale, (2) a ground state modified by interlayer coupling, (3) nonuniform radial excitation, and (4) interlayer dipole coupling. While eigenmode amplitudes have been found insensitive to changes in conditions 2, 3, and 4, consideration of the latter has revealed considerable dependence of the frequency properties of the nanopillar on spacer layer thickness. In the present chapter, variation of the spacer layer thickness and relative chirality are shown to affect changes in the frequency, intralayer phase, and interlayer phase shift of the mutual precessions of the magnetic layers.

In order to gauge the influence of interlayer dipole coupling on the magnetization dynamics, the simulations of Chapter 7 have been extended to spacer layer thicknesses d

from 1 to 25 nm. A simple grid search for suitable pulse parameters has been performed by refining switching diagrams (Chapter 6) for each d, in each initial chirality, with subcritical and critical excitations. For each system, the conditions were: one switch, minimal gyrotropic excursion of the vortex core, no polarity switching, and coherence during relaxation. The difficulty in meeting these criteria as $d \to 25$ nm is summarized in Section 6.4.

Although $n > 0$ eigenmode profiles are less well preserved in less coherent cases, layer-averaged frequency measurements during relaxation have been found consistent regardless of excitation process – following not only highly coherent switching but also mild gyrotropic disturbance as well as highly incoherent response including transient telegraph switching of the free layer vortex core polarity. In relatively incoherent cases in which $n > 0$ modes get washed out by short-wavelength spin waves, the primary modes and their induced oscillations remain quite robust. As long as the vortex core remains within a few nanometers of the center of the disk, symmetry preserves the radial structure and phase. As in Chapter 7, we focus here on coherent relaxation at least 300 ps after the end of the current pulse, when the magnetization dynamics are limited to small angle precession about an equilibrium state.

8.1 Frequency shifts

Figure 8.1 displays FFT power spectra for d from 1 to 25 nm in parallel relaxation. Each curve is offset by 12 dB to enable comparison, with d increasing from bottom to top. The modes responsible for each ridge are labeled at the top of the figure. The frequencies of the Py modes increase and saturate with increasing d. In contrast, the Co mode frequencies are relatively insensitive to d: mode frequencies in parallel relaxation increase slightly for $d < 4$ nm and level off, and in antiparallel relaxation decrease slightly over the range of d.

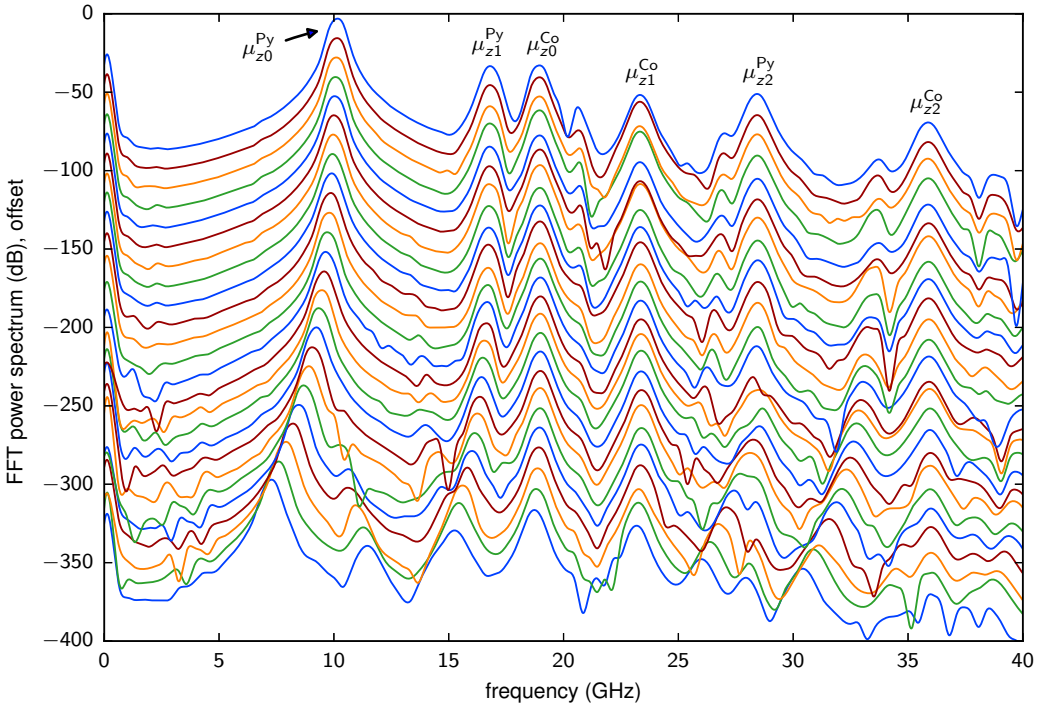

Figure 8.1: Carpet plot of Fourier power spectra of $\langle m_z^{\mathrm{Py}} \rangle$ for d from 1 (bottom curve) to 25 nm (top) in parallel relaxation. Signals are successively offset by 12 dB. Nearly uniform spacing between the curves indicates consistent spectra. Ridge lines depict d dependence of the frequency, for example the left most set of peaks (μ_{z0}^{Py}) blue shifts from bottom to top with increasing d.

All modes approach limiting values as $d \to 25$ nm.

We find consistently a frequency shift between relative chiralities. Eigenmode frequency is shown as a function of spacer thickness in Figure 8.2. Each curve corresponds to a ridge line in Figure 8.1 or its antiparallel counterpart. Convergence to the saturation frequencies as $d \to 25$ nm is consistent, indicating that the frequency shift is a product of interlayer coupling. For Py eigenmodes with induced oscillations in Co, the antiparallel configuration precesses at a lower frequency than the parallel configuration. In Co the chirality dependence varies: the parallel configuration precesses at a lower frequency than antiparallel in the $n = 0$ and $n = 1$ modes, and higher in the $n = 2$ mode. The $d = 1$ nm

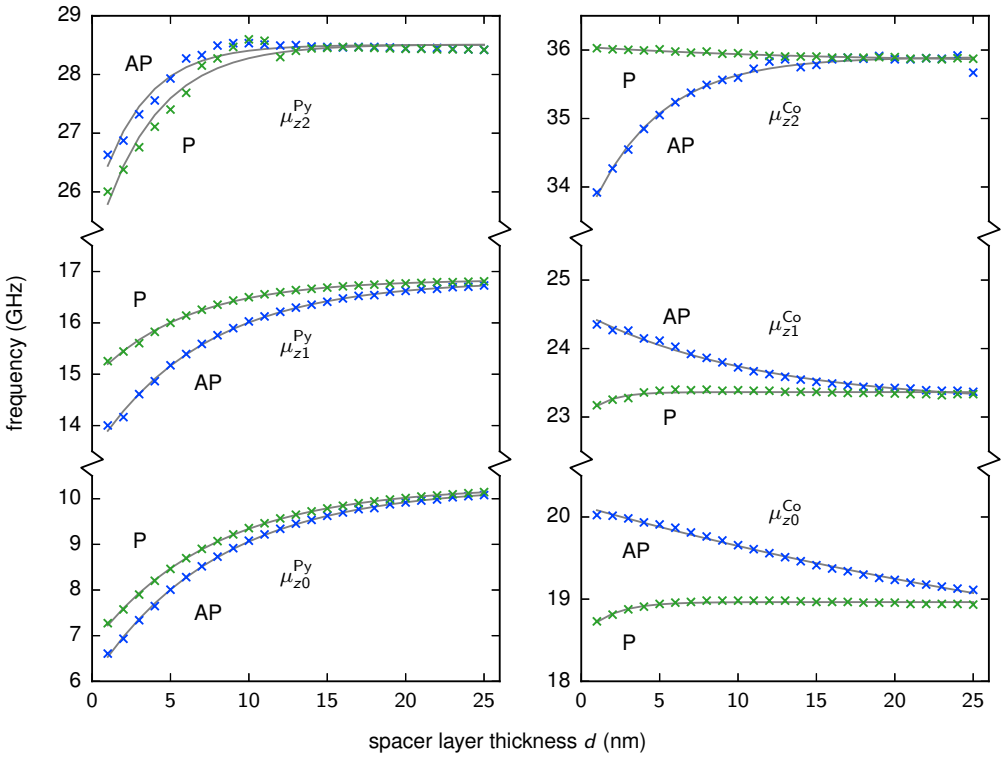

Figure 8.2: Relative chirality and spacer thickness dependence of eigenmode frequencies in Py (left column) and Co (right). All modes show splitting that decreases with increasing d. Py modes blue shift with increasing spacer thickness. Co modes in parallel relaxation are relatively insensitive.

splittings for Py $n = \{0, 1, 2\}$ are 10%, 8%, and 2%; for Co, 7%, 5%, and 6%. In all cases splitting decreases with d.

8.2 Mode intralayer phase

In Chapter 7 we reported that the eigenmode node positions and relative edge amplitudes do not significantly change with spacer layer thickness. However, intralayer phase (Section 7.2) does change in both the modes and the induced oscillations. Figure 8.3 summarizes changes in the the modes in parallel relaxation, with Py in the left column, Co in the right, and the mode index increasing from top to bottom. Each panel shows the

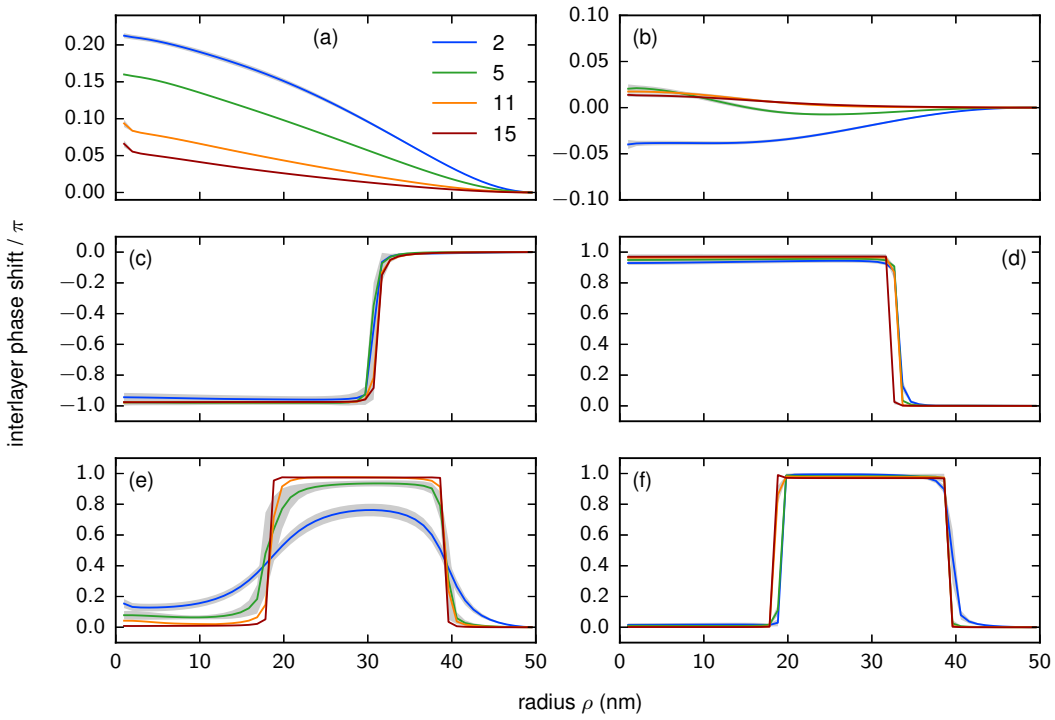

Figure 8.3: Intralayer phase relative to the edge for the Py (left column) and Co (right) $n = \{0, 1, 2\}$ modes, for $d = 2$, 5, 11, and 15 nm in parallel relaxation (top to bottom in (a) and with the same colours in other panels). (a) μ_{z0}^{Py} loses its traveling character with increasing d. (b) μ_{z0}^{Co} precesses nearly in phase in parallel relaxation. (c, d) $\mu_{z1}^{\mathrm{Co,Py}}$ are relatively insensitive to spacer thickness. (e) μ_{z2}^{Py} shows bending at the nodes and a suppressed antinode amplitude, while (f) μ_{z2}^{Co} has a conventional radial phase. The standard deviation of six measurements over the course of relaxation (grey curve) for $d = 2$ and $d = 5$ nm in (e) indicates that these unusual phases are consistent over time.

intralayer phase relative to the edge magnetization for $d = 2, 5, 11$, and 15 nm.

With increasing d, the Py $n = 0$ modes lose their traveling character. Shown in Figure 8.3(a), the radial shift of 0.23π in parallel relaxation (0.32π antiparallel) decreases to 0.02π. The Co $n = 0$ mode precesses nearly in phase throughout the layer, (b), in contrast to the large radial shift in antiparallel relaxation shown in Figure 7.6 for $d = 6$ nm that decreases as (a) with increasing d. Variation in the higher order modes is also chirality-dependent. Both $n = 1$ modes are relatively insensitive to increasing d with π shifts across the node that become only slightly more abrupt, (c) and (d). This is different to the antiparallel case for both Co and Py, the latter shown in Figure 7.7 with a phase shift diminished in magnitude and spread over several nanometers, features that decrease with increasing d. (See Section 7.2 for a discussion.) In the Py $n = 2$ mode shown in (e) the second antinode amplitude increases and the bending decreases with increasing d, while the shifts in the Co $n = 2$ mode in (f) are conventional. Evidently, stronger coupling between layers increases the traveling nature of the eigenmodes, and as the magnetic layers become decoupled the eigenmodes tend to the standing nature previously observed in large isolated disks. If one considers the eigenmodes described in the previous chapter to be superpositions of standing and traveling waves, the standing part is fundamental to the disk system and the traveling part is induced by interlayer coupling.

8.3 Interlayer phase

The frequency shift with relative chirality originates in the interlayer phase of precession. m_z^{Py} and m_z^{Co} are coupled by their dynamic stray field, and as coupled oscillators their frequency depends on their mutual phase. This effect has been shown for in-plane coupled, normally-magnetized disks, in analogy to a two level molecule with bonding and

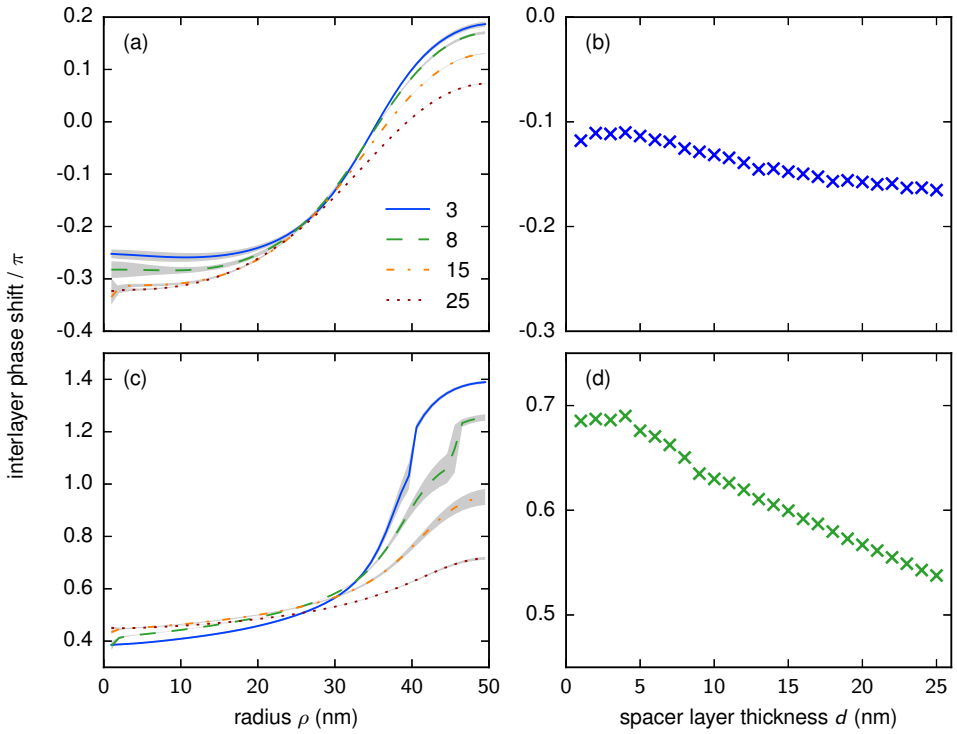

Figure 8.4: Interlayer phase in the Py $n = 0$ mode for $d = 3, 8, 15$ and 25 nm, from top to bottom at $\rho = R$, in (a) antiparallel and (c) parallel relaxation, with grey curves giving the standard deviation. (b, d) The mean interlayer phase shifts for all values of d, for antiparallel and parallel relaxation respectively.

anti-bonding states [183], and for coupled vortex systems in the translational mode [199].

The left column of Figure 8.4 shows interlayer phase as a function of pillar radius. Py is the reference layer, so a negative phase indicates μ_z^{Py} leading μ_z^{Co}. Panels (a) and (c) depict representative cases $d = 3, 8, 15$, and 25 nm of the Py $n = 0$ mode, in order from top to bottom at $\rho = R$ in panel (a), showing the insensitivity and minimal decline of the interlayer phase shift in the antiparallel and parallel configurations respectively.

The average shift for each value of d is shown in the right column of Figure 8.4. Py and Co precess nearly in phase in μ_{z0}^{Py} in the antiparallel configuration, with phase decreasing slightly with increasing d from -0.11π to -0.17π, on average $(-0.14 \pm 0.02)\pi$. In the higher frequency parallel configuration, the interlayer phase decreases with d, from 0.69π to 0.54π,

on average $(0.62 \pm 0.05)\pi$. In the Co $n = 0$ mode (not shown), the antiparallel configuration is nearly in antiphase, with Py trailing Co by $(0.90 \pm 0.01)\pi$ with negligible d dependence. In the lower frequency parallel configuration, the phase shift decreases linearly, from -0.08π, nearly in phase, to -0.22π, 11% desynced. Figure 8.4(b) and (d) show that even when the fundamental modes lose their traveling character (Section 8.2), the interlayer shift persists with relatively little dependence on d.

Collectively, these results explain the chirality dependence of the Py fundamental mode frequencies in Figure 8.2. In the antiparallel configuration, μ_{z0}^{Py} and the induced oscillation in Co precess nearly in phase at a lower frequency. When parallel, they precess out of phase by more than 0.5π at a consequently higher frequency. With increasing d, the phase shift remains but the contribution of the interlayer interaction to the total energy of the system diminishes and the frequencies of the different chiralities approach the same decoupled limit.

8.4 Stray field

The final analysis in this chapter is a visualization of the interlayer stray field that couples the dynamic magnetizations during relaxation. Stray field analysis for in plane coupled disks in Ref. [200] has shown that topological features in the field shape affect the stability and dynamics of field-coupled systems much as magnetic solitons do their respective magnetizations. Interlayer coupling is mediated by the demagnetization field, which is generated by surface charges, therefore the m_z component is apposite, in both layers and in each of its dynamic modes. We use the scalar potential method, Equations 2.20 and 2.22, to calculate the field in a volume enclosing the pillar. By bandpass-filtering the magnetization used as the source in Equation 2.22, we isolate the frequency component of

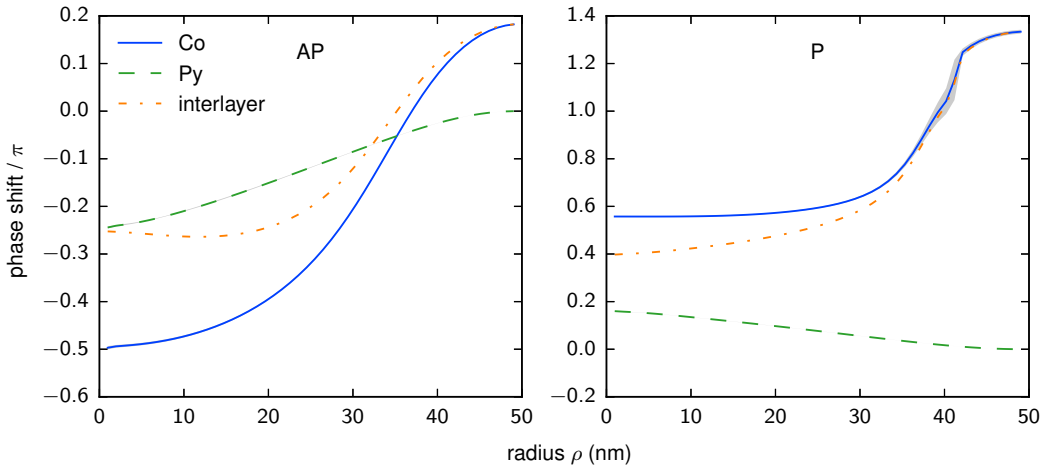

Figure 8.5: Intralayer and interlayer phase in the Py $n = 0$ mode for $d = 5$ nm in antiparallel (left panel) and parallel (right) relative chiralities.

the stray field corresponding to the dynamical mode of interest.

The stray field points opposite the magnetization in an isolated magnet, but outside it issues from positive surface charges $\mathbf{m} \cdot \hat{\mathbf{n}}$, so it is discontinuous on the boundary. The lowest energy configuration therefore has minimal surface charges and flux closure of the stray field outside with the magnetization inside. This occurs when the dynamic magnetizations orient antiparallel, resembling a pair of dipoles alongside one another, with field lines emanating from the head of one leading to the tail of the other. Precession occurs at a fixed frequency in the ρz plane (Section 6.2), so if the dipoles rotate in opposite directions, overall flux closure is maintained. If they rotate with the same handedness, they pass through head-to-head or tail-to-tail configurations, increasing the stray field energy. In the pillar this is complicated by nonuniformity, phase variation, and the fact that the dynamics are concentrated in the free layer. Also, as in the magnetization, complexity emerges in the vortex core. Due to symmetry, the stray field along the axis points either up or down, which in turn directs the stray field in the spacer near the core. While switching in the plane travels radially, switching along $\rho = 0$ proceeds axially.

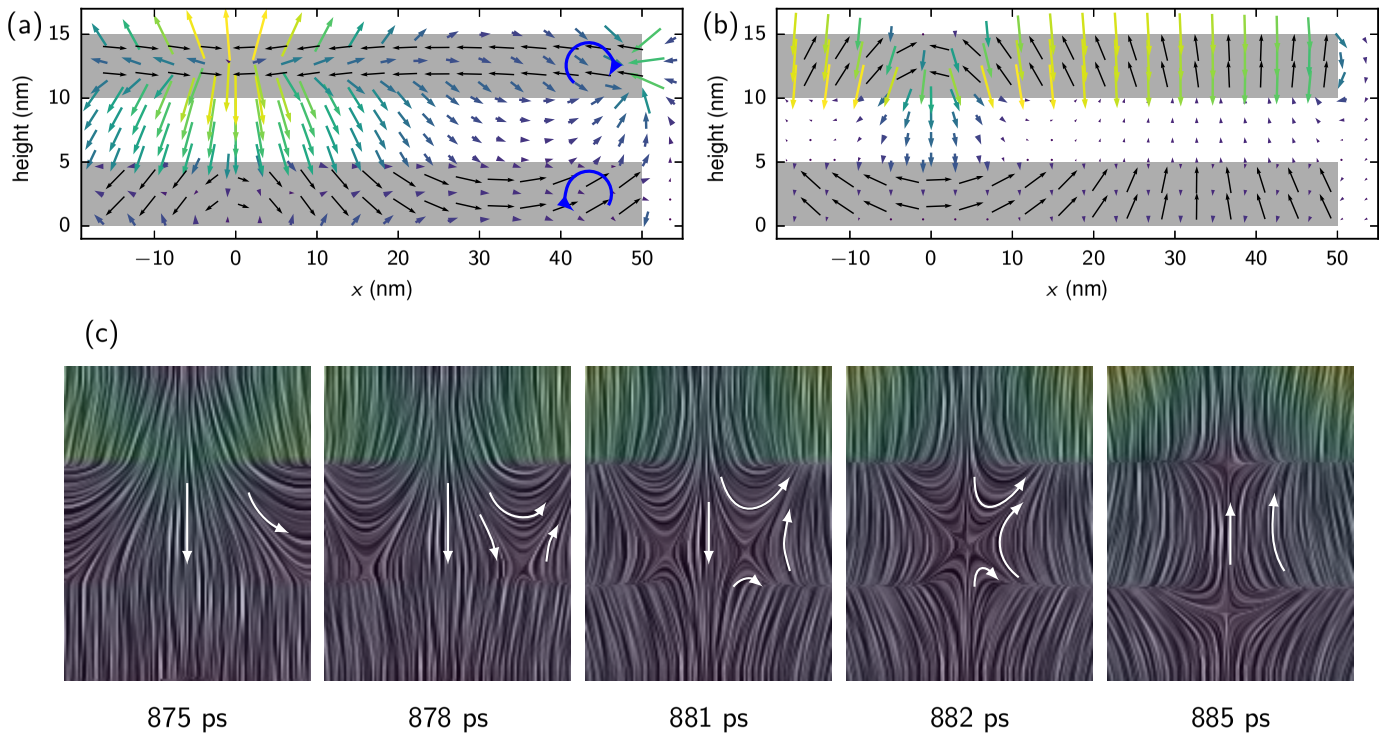

Figure 8.6: Stray field configuration during antiparallel relaxation ($d = 5$ nm, 8.0 GHz). (a) Flux closure of the stray field and magnetizations in the spacer and at the edge, shown in the xz plane. The magnetizations rotate with opposite sense (blue arrows). Grey boxes indicate the extents of the magnetic layers, with the Co layer scaled by a factor of four along z for clarity. (b) One quarter cycle after (a), the magnetizations are parallel and out of plane outside the core, and the stray field in the spacer layer rotates from negative to positive along $+x$. (c) Detail of the stray field switching process in the core. The first panel corresponds to (b). Each frame is 22 nm wide and centered at $x = 0$.

Antiparallel relative chirality is the lower-frequency configuration, and as Figure 8.5(a) implies, the stray field coupling is straightfoward. A cycle begins at a local minimum in (filtered) demagnetization energy, with $\mathbf{m}^{\mathrm{Co}}$ (Co) and μ_0^{Py} (Py) in a flux-closed arrangement. Co points radially outward in the region $\rho > 0.5R$, Py inward, and the stray field at $\rho > R$ connects the edge charges from bottom to top. From the mid-radius to the core, the magnetizations curl downward out of plane. The stray field in the spacer layer is generated by Py and points along $-\hat{\mathbf{z}}$, and the overall configuration is flux-closed. In Figure 8.5(a), recalling that a negative phase corresponds to Py leading Co, the edge component $m_z^{\mathrm{Co}}(R)$ is shown to precede $\mu_{z0}^{\mathrm{Py}}(R)$. (Here m_z^{Co} refers only to the component at the frequency of $\mu_{z0}^{\mathrm{Py}}(R)$.) Figure 8.6(a) shows the stray field (colored arrows, with length scaled by the norm) and dynamic magnetization (black unit vectors) in select cells after 15 ps have elapsed: Co rotates counterclockwise around $-\hat{\boldsymbol{\phi}}$, starting from the edge, and Py rotates clockwise (blue arrows). Then the waves in m_z spread inward, propagated by dynamic exchange; the wavefront in μ_{z0}^{Py} passes Co at $\rho \approx 0.7R$, where the interlayer phase is zero. After 45 ps, the magnetizations and stray field in $\rho > 0.5R$ point upward (Figure 8.6(b)). Still oriented downward in the core, the stray field buckles. Due to the stability of the core, the amplitude of the dynamic magnetization goes to zero as $\rho \to 0$. The buckling in the stray field forms an antivortex as it is compressed, and the magnitude of the field vanishes as it converges at the center and then propagates axially outward. This process is shown in Figure 8.6(c), the first frame corresponding to the configuration in (b). The fourth frame in (c) coincides with the termination of the μ_{z0}^{Py} antinode at $\rho = 0$. Immediately after this sequence, the stray field emerges along $+\hat{\mathbf{z}}$ at the center, connecting the arriving wavefront in m_z^{Co} (lagging 0.25π behind Py, Figure 8.5(a)) to the diminishing negative charge of μ_{z0}^{Py}. As the stray field grows, the pillar rotates into the left-handed version of the configuration in Figure 8.6(a), completing one half-cycle of the mode. On

average, the out of plane moments precess nearly in phase, and the flux-closure of the stray field and magnetizations sustains a relatively low energy configuration.

Figure 8.5(b) depicts the contrasting case of the parallel configuration. Here m_z^{Co} and μ_{z0}^{Py} propagate in opposite directions, Figure 8.5(b), but again the radial phase shift in Py is minimal and it rotates almost in unison. The cycle begins in the mostly flux-closed state shown in Figure 8.7(a), similar to the antiparallel case. Figure 8.7(b) shows the component of the demagnetization energy corresponding to the eigenmode (solid line) and the total demagnetization energy offset by its equilibrium value (dashed line). The minimum at 800 ps corresponds to (a) and the black circles the successive frames of (c). Different to antiparallel relaxation, both magnetizations rotate counterclockwise around $-\hat{\boldsymbol{\phi}}$. The stray field flips positive in the core at the top surface of Py, preceding the emergence of μ_{z0}^{Py}, and the resulting node propagates downward through the layer, as shown in Figure 8.7(a). Py rotates further, and the node in the stray field forms an antivortex at the bottom surface of Py, seen in the third panel of Figure 8.7(c). As Py aligns almost uniformly along $-\hat{\mathbf{z}}$, perpendicular to Co in the region $\rho < 0.6R$ and nearly antiparallel at the edge, the antivortex transits the spacer layer, from 822–825 ps in Figure 8.7(c), carrying the positive orientation of the stray field down the axis. It then disperses at the Co surface as m_z^{Co} finally reaches the core. This completes one half-cycle of the mode, with Py pointing radially out and another stray-field soliton forming at its top surface. Due to the interlayer phase, the average interaction is a repulsive configuration.

Unlike Ref. [200], we find no evidence that antivortex packets in the stray field carry energy between the magnets. In this case they are simply topological consequences of the traveling nature and radial symmetry of the eigenmodes. Also in contrast, we identify the transient solitons with a vanishing stray field rather than local maxima in its magnitude. This is indicated by the color saturation in Figure 8.7(c), which is proportional to the field

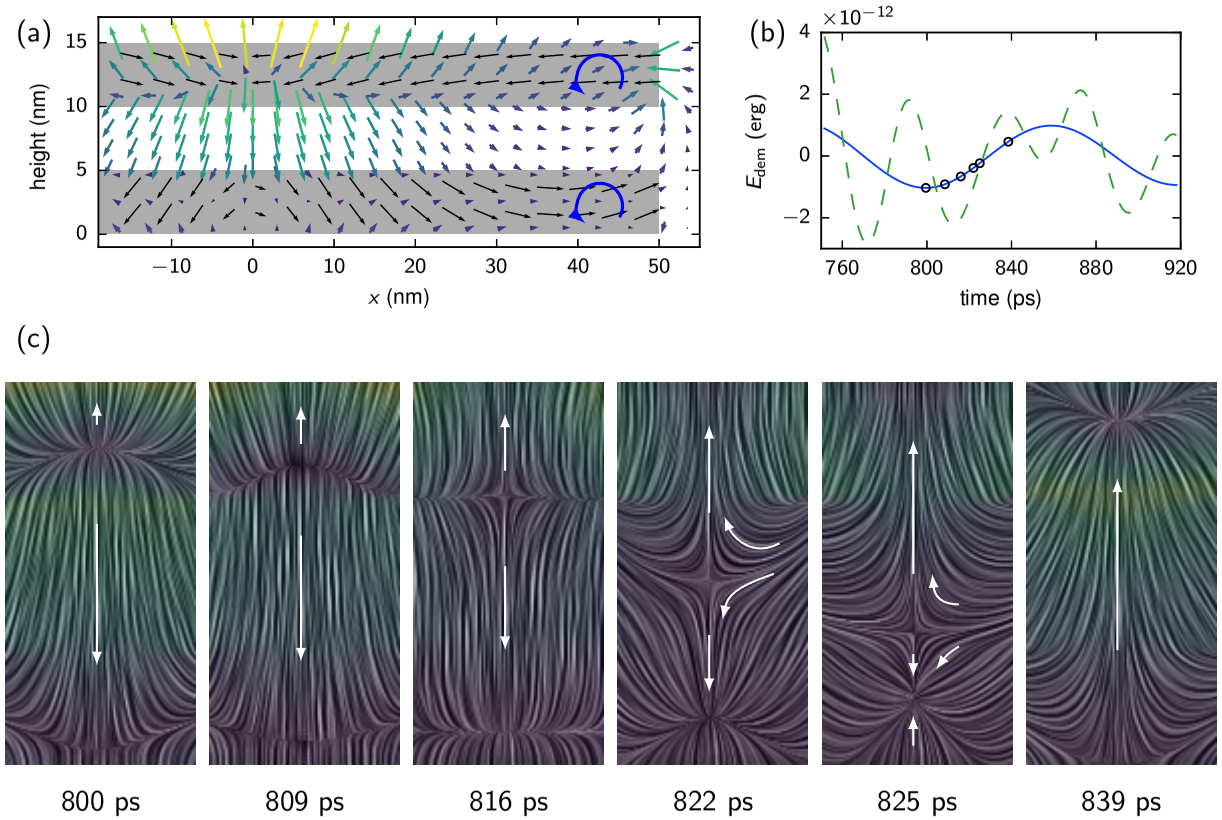

Figure 8.7: Stray field configuration during parallel relaxation ($d = 5$ nm, 8.5 GHz). (a) Stray field (colored arrows, with length scaled by the norm) and normalized magnetization (black). (b) Demagnetization energy: 8.5 GHz component (blue line) and total less an offset (dashed green line). (c) Antivortex in the stray field propagating from Py to Co, resolved by line integral convolution. The magnified region spans $\pm R_c^0$ along the x axis, and the color saturation is proportional to the norm of the field. Frames correspond to the black circles in (b).

norm and most intense before and after the antivortex flips the orientation of the axial stray field. We found a similar process for parallel relaxation with several spacer layer thicknesses and in the Co $n = 1$ mode, but have not yet performed a comprehensive survey.

8.5 Summary

Eigenmode structures have been found insensitive to, but the eigenfrequencies strongly dependent on, variation of the spacer layer thickness. This supports the conclusion that the vortex cores are responsible for the eigenmode profiles and not the interlayer coupling. The interlayer dipole interaction itself depends not only on spacer thickness but also the relative chirality, and determines the phase shift between Co and Py layer precession and therefore the frequencies of precession. Frequency splitting between the relative chiralities decreases with spacer thickness because the coupling of the in plane magnetizations diminishes, even as the interlayer phase shift is relatively consistent. Finally, the effect of the interlayer phase on the stray field in the Py fundamental mode has been demonstrated with a series of visualizations. On average, the magnetizations in antiparallel relaxation precess nearly in phase, resulting in a flux-closed stray field and lower precessional frequency. In contrast, for parallel relaxation there is considerable frustration between the magnetizations and stray field throughout the cycle, increasing the frequency of precession. We find the evolution of the stray field to be mediated by transient solitons.

Chapter 9

Conclusions

Vortex chirality switching has been demonstrated by micromagnetic simulation. The switching method employs nonresonant excitation by spin transfer torque in an all-metallic spin valve nanopillar, and switching proceeds without soliton nucleation and annihilation and without gyrotropic perturbation of the vortex core. As a method for writing and retrieving binary information, it compares favourably to vortex polarity switching in its coherence, speed, and large readout signal via giant magnetoresistance. Furthermore, it is simpler, more compact, and more efficient than other chirality control mechanisms since proposed, and could be realized with standard spintronic materials and fabrication techniques. Switching times are on the order of 100 ps, sufficient for memory and logic applications.

The principle motivation of this thesis is to fully describe the chirality switching process. Two new results have emerged. First, we implemented numerical modelling of a nanopillar system tailored for spin transfer torque to characterize the dynamic excitation and relaxation of the pillar's free layer vortex-state magnetization. Second, we analyzed unique radial spin wave eigenmodes that form during the relaxation of the system and

determined their origin.

To control and detect relative chirality, we implement a nanopillar system with an asymmetric spin valve. The relative chirality state of the pillar, the parallel or antiparallel sense of the individual in plane chiralities, stores one bit of information, and switching the free layer magnetization toggles the bit state. Asymmetric means that its fixed and free magnetic layers are dissimilar. For stability and ease of switching respectively, the fixed layer is designed to be relatively thick and magnetically hard and the free layer thin and soft. This arrangement also provides the angular offset between fixed and free layer magnetizations necessary for spin transfer torque. The current induced dynamics immediately following onset of the current pulse are tracked and dissected in two ways. First, detection of the dynamic relative chirality is provided by the giant magnetoresistance of the spin valve, with low and high resistances at remanence corresponding to parallel and antiparallel pillar configurations respectively. Time-resolved resistance would be accessible in a straightforward experiment. Second, the dynamic magnetizations and internal micromagnetic energies of the pillar and individual magnetic layers are tracked numerically. New experimental techniques can image material specific (and therefore in our case layer-resolved) magnetization on picosecond time scales, with in plane resolution on the order of 10 nm. Visualization of cell- and layer-resolved magnetization in addition to internal fields is now standard in our simulation methodology and can provide useful checks against future experiments.

A wide range of current pulse parameters leading to distinct regimes of dynamic response has been investigated. In addition, the thickness of the spacer layer in the spin valve was varied in order to change the angular offset between magnetizations and therefore the efficiency of excitation by spin transfer torque. Thinner spacer layers, between 1 and 10 nm, are found to require less current pulse amplitude to switch and exhibit more coherent dynamics after switching. Thicker spacer layers, between 10 and 25 nm, with

smaller angular offsets and less of the stabillizing coupling between magnetic layers, require larger current pulse amplitudes to switch and exhibit less coherent dynamics, resulting in gyrotropy and polarity switching of the free layer vortex core over a wider range of pulse parameters than pillars with thinner spacer layers. Interlayer exchange coupling has been neglected throughout; a study of thin spacer layers, between 0.5 and 5 nm, that includes interlayer exchange coupling between the ferromagnetic layers could be performed in order to determine to what degree it modifies the remanent states, interferes with chirality switching, or alters the relaxation process. For example, antiferromagnetic coupling has been found elsewhere in multilayers with similar composition and 1 nm spacer layers [201]. Pinholes may also induce ferromagnetic coupling for spacers thinner than about 1.5 nm.

The second focus of this is magnetization relaxation after chirality switching. Spin wave eigenmodes stimulated by the switching process with unusual, large edge-amplitude radial eigenmode profiles are reported. These differ from the predictions of analytical models and observations of previous experiments on single layer disks with larger radii. By a series of checks, including variation of the spacer layer thickness, several possible causes for these novel profiles were ruled out, including the existence of the angular offset, which is absent in isolated disks, the nonuniformly distributed and radially oriented spin transfer torque versus the uniform out of plane magnetic field previously used, and the magnetic stray field coupling between the fixed and free layers, a feature of spin valve systems absent in previous studies. We have determined that the large ratio of vortex core size to free layer size in our system is the causative factor in the eigenmode formation. This result confirms the prediction of Guslienko that the prevailing model may not hold for disks smaller than 400 nm and demonstrates how relaxation dynamics differ in this regime. Large edge amplitudes in the radial component have implications for crosstalk in memory applications.

Not only do the reported spin wave eigenmodes have large edge amplitudes, con-

trary to the convention of strong in-plane magnetic pinning at the edge, the fundamental mode in the free layer was found to have a traveling rather than standing character. These spin waves were found to propagate radially inward, from the edge of the disk to the vortex core. With decreased interlayer coupling, the traveling waves revert to conventional standing waves.

The strength of the dynamic coupling between the magnetic layers of the spin valve has been found to change the precessional frequencies but not the structures of the radial eigenmodes. The fundamental mode frequencies in the free layer increase from approximately 6.5 GHz to 10.3 GHz over spacer layer thicknesses from 1 to 25 nm, with similar trends in the higher order modes. We also found frequency splitting between relative chirality states, and its origin in the interlayer phase of precession was identified. Splitting vanishes with increasing spacer layer thickness (decreasing coupling between the magnetic layers), from 10% to less than 0.1% in the free layer fundamental mode over spacer layer thicknesses from 1 to 25 nm. In order to quantify the effect of pillar radius on eigenmode edge amplitudes and elucidate the limits to the existing analytical model, a systematic numerical study of both pillar radius and aspect ratio could be performed in the future.

Visualizations of the interlayer stray field give connection to the interlayer phase and dynamic energies of the nanopillar during relaxation. An implementation of the algorithm in Ref. [101] using the scalar potential method allows for efficient computation of the stray field. Filtering the dynamic magnetization at the eigenmode frequencies and then computing the stray field it generates in the spacer layer reveals the phase-dependent interplay between magnetic layers in the spin valve and explains qualitatively the frequency shift between relative chiralities. Similarly filtered systemic demagnetizaiton energy adds a more quantitative context to the analysis, but we point out that the demagnetization field and internal energies are inaccessible to experiment.

As well as the above suggestions, there are several other possibilities for future work. Efforts could be made to eliminate precession in the fixed layer of the nanopillar, which is considered advantageous for efficient switching. Despite the relative bulk and magnetic hardness and thus limited amplitude response of the fixed layer in this study, its dynamics during relaxation were shown to play a notable role. A more strongly pinned fixed layer should further diminish its contribution and simplify the switching process. However, increasing hardness, for example by alloying, may also change spin polarization efficiency, anisotropy, remanent states, and interface quality; these are each accessible to varying degress in micromagnetic simulation and experiment. Exchange biasing the fixed layer with an antiferromagnetic underlayer may be another direction, but adds considerable complexity to fabrication.

Experimental efforts to realize dynamic chirality control in nanopillars have evidently stalled. Ref. [178] tested our system quasistatically, and confirmed our prediction in Ref. [179] that chirality selection by spin transfer torque is viable. Similarly, an early objective of the work in this thesis included the design and implementation of a four point probe apparatus for transport measurements of patterned layered magnetic structures. The apparatus was completed and successful measurements of hysteretic magnetoresistance in nanowires and magnetic tunnel junctions were made. However, we were unable to progress to magnetization dynamics excited by time-dependent fields or spin transfer torque. The limiting factor throughout, both in development of the apparatus and in experimental work, was sample fabrication. Even relatively straightforward devices require multiple lithographic steps ranging from functional features less than 100 nm in size to micron-wide connecting wires to contact pads hundreds of microns in diameter. Spin valve components require well-calibrated sputter deposition for multilayer deposition, and, a particular challenge, clean interfaces between each of the circuit elements. Our capabilities have de-

veloped considerably since this work began, and in-house experiments on multilayer devices may soon be possible.

Finally, this work can inform future applications-oriented research with a few key modifications. Our method is competitive with other proposals for topological control of magnetic vortices, and exceeds other bases for magnetic soliton-based magnetic random access memory (MRAM). However, a metallic spin valve-based MRAM cell is incompatible with the current complementary metal-oxide semiconductor (CMOS) platform for integrated circuits: Write currents on the order of 10 mA are an order of magnitude too high for minimum size MOSFETs (0.1–0.2 mA) [202], the nominal resistance is too low to pair with a CMOS transistor, and the GMR ratio, the difference in resistance between bit states, is too small relative to the spread of remanent state resistances in an array of cells. A magnetic tunnel junction, the tunneling magnetoresistance analog to the spin valve, meets these criteria and is used in place of the spin valve in present day MRAM [203]. The nanopillar system in this thesis could be modified by replacing the metallic interlayer with a thin insulating spacer to incorporate tunneling spin transfer torque and tunneling magnetoresistance. Special attention should be paid to the out-of-plane torque that is negligible in spin valves but can be significant in magnetic tunnel junctions [22]. With current techniques for thin insulator deposition, fabrication on a proof of concept scale would be similar to that for the system in this thesis.

Together these are noteworthy steps forward in the understanding of magnetization dynamics in confined magnetic multilayer structures, and the merits of vortex-based MRAM make it worth further study. Complementary numerical simulations, experiments, and fabrication technologies will continue to be necessary for progress. Despite many unknowns surrounding future computing technologies, it appears certain that nanomagnetism will continue to play a notable role in research and development.

Bibliography

[1] R. Kling and W. Scacchi, in *The Web of Computing: Computer Technology as Social Organization*, Vol. 21 of *Advances in Computers*, edited by M. C. Yovits (Elsevier, Amsterdam, Netherlands, 1982), pp. 1–90.

[2] H. Geser, Knowledge, Technology & Policy **19**, 8 (2006).

[3] R. W. Keyes, Solid-State Circuits Society Newsletter **11**, 25 (2006).

[4] D. E. Liddle, Solid-State Circuits Newsletter, IEEE 28 (2006).

[5] D. W. Jorgenson, M. S. Ho, and J. D. Samuels, in *Long-term Estimates of U.S. Productivity and Growth* (Tokyo: Third World KLEMS Conference, Tokyo, Japan, 2014).

[6] C. Orwat, A. Graefe, and T. Faulwasser, BMC Medical Informatics and Decision Making **8**, (2008).

[7] T. M. Mogotlhwane, M. Talib, and M. Mokwena, in *Digital Information and Communication Technology and Its Applications: International Conference, DICTAP 2011, Dijon, France, June 21-23, 2011, Proceedings, Part II*, edited by H. Cherifi, J. M. Zain, and E. El-Qawasmeh (Springer Berlin Heidelberg, Berlin, Heidelberg, 2011), pp. 642–653.

[8] J. M. D. Coey, *Magnetism and Magnetic Materials* (Cambridge University Press, Cambridge, UK, 2010).

[9] L. Hoddeson, Historical Studies in the Physical Sciences **12**, 41 (1981).

[10] Z. Bandic and R. H. Victora, Proceedings of the IEEE **96**, 1749 (2008).

[11] R. Wood, IEEE Transactions on Magnetics **36**, 36 (2000).

[12] W. Thomson, Proceedings of the Royal Society of London **8**, 546 (1856).

[13] C. A. Ross, Annual Review of Materials Research **31**, 203 (2001).

[14] K. Prall, N. Ramaswamy, and A. Goda, in *Charge-Trapping Non-Volatile Memories: Volume 1 – Basic and Advanced Devices*, edited by P. Dimitrakis (Springer International Publishing, Cham, 2015), pp. 37–64.

[15] E. Vogel, Nature Nanotechnology **2**, 25 (2007).

[16] D. S. Jeong, R. Thomas, R. S. Katiyar, J. F. Scott, H. Kohlstedt, A. Petraru, and C. S. Hwang, Reports on Progress in Physics **75**, 076502 (2012).

[17] B. C. Choi, Y. K. Hong, A. Lyle, and G. W. Donohoe, *CMOS Processors and Memories* (Springer, New York, NY, USA, 2010), pp. 233–252.

[18] L. M. Grupp, J. D. Davis, and S. Swanson, in *Proceedings of the 10th USENIX Conference on File and Storage Technologies* (USENIX Association, Berkeley, CA, USA, 2012), pp. 2–2.

[19] M. H. Kryder and C. S. Kim, IEEE Transactions on Magnetics **45**, 3406 (2009).

[20] M. Gajek, J. J. Nowak, J. Z. Sun, P. L. Trouilloud, E. J. O'Sullivan, D. W. Abraham, M. C. Gaidis, G. Hu, S. Brown, Y. Zhu, and R. P. Robertazzi, Applied Physics Letters **100**, 132408 (2012).

[21] J. J. Nowak, R. P. Robertazzi, J. Z. Sun, G. Hu, J. H. Park, J. H. Lee, A. J. Annunziata, G. P. Lauer, C. Kothandaraman, E. J. O'Sullivan, and P. L. Trouilloud, IEEE Magnetics Letters **7**, 1 (2016).

[22] N. Locatelli, V. Cros, and J. Grollier, Nature materials 1 (2014).

[23] V. V. Kruglyak, S. O. Demokritov, and D. Grundler, Journal of Physics D: Applied Physics **43**, 264001 (2010).

[24] A. V. Chumak, V. I. Vasyuchka, A. A. Serga, and B. Hillebrands, Nature Physics **11**, 453 (2015).

[25] G. E. Bauer and Y. Tserkovnyak, Physics **4**, 40 (2011).

[26] A. V. Chumak, A. A. Serga, and B. Hillebrands, Nature Communications **5**, 4700 (2014).

[27] T. Schneider, A. A. Serga, B. Leven, B. Hillebrands, R. L. Stamps, and M. P. Kostylev, Applied Physics Letters **92**, 022505 (2008).

[28] M. Jamali, J. H. Kwon, S.-M. Seo, K.-J. Lee, and H. Yang, Scientific Reports **3**, (2013).

[29] G. A. Prinz, Science **282**, 1660 (1998).

[30] F. Büttner, Ph.D. thesis, Johannes Gutenberg-Universit at Mainz, 2013.

[31] J. Miltat and A. Thiaville, Science **298**, 555 (2002).

[32] P. A. M. Dirac, Proceedings of the Royal Society of London, Series A **123**, 714 (1929).

[33] A. A. Abrikosov, Type II Superconductors and the Vortex Lattice, Nobel Lecture, 2003.

[34] P. Kapitza, Nature **141**, 3558 (1938).

[35] J. F. Allen and A. D. Misener, Nature **142**, 3597 (1938).

[36] M. W. Zwierlein, J. R. Abo-Shaeer, A. Schirotzek, C. H. Schunck, and W. Ketterle, Nature **435**, (2005).

[37] A. M. Kosevich, B. A. Ivanov, and A. S. Kovalev, Physics Reports **194**, 117 (1990).

[38] T. Shinjo, Science **289**, 930 (2000).

[39] M. Schneider, H. Hoffmann, and J. Zweck, Applied Physics Letters **77**, 2909 (2000).

[40] Ultramicroscopy **109**, 264 (2009).

[41] A. Wachowiak, J. Wiebe, M. Bode, O. Pietzsch, M. Morgenstern, and R. Wiesendanger, Science **298**, 577 (2002).

[42] H. Stoll, A. Puzic, B. van Waeyenberge, P. Fischer, J. Raabe, M. Buess, T. Haug, R. Höllinger, C. Back, D. Weiss, and G. Denbeaux, Applied Physics Letters **84**, 3328 (2004).

[43] B. van Waeyenberge, A. Puzic, H. Stoll, K. W. Chou, T. Tyliszczak, R. Hertel, M. Fähnle, H. Brückl, K. Rott, G. Reiss, I. Neudecker, D. Weiss, C. H. Back, and G. Schütz, Nature **444**, 461 (2006).

[44] K. W. Chou, A. Puzic, H. Stoll, D. Dolgos, G. Schutz, B. van Waeyenberge, A. Vansteenkiste, T. Tyliszczak, G. Woltersdorf, and C. H. Back, Applied Physics Letters **90**, 202505 (2007).

[45] M. Ammar, M. LoBue, E. Snoeck, M. Hÿtch, Y. Champion, R. Barrué, and F. Mazaleyrat, Journal of Magnetism and Magnetic Materials **320**, e716 (2008).

[46] K. He, D. J. Smith, and M. R. McCartney, Applied Physics Letters **94**, 1 (2009).

[47] S. H. Chung, R. D. McMichael, D. T. Pierce, and J. Unguris, Physical Review B **81**, 1 (2010).

[48] J. Rudge, H. Xu, J. Kolthammer, Y. K. Hong, and B. C. Choi, Review of Scientific Instruments **86**, (2015).

[49] Y. Acremann, Science **290**, 492 (2000).

[50] V. Novosad, M. Grimsditch, K. Guslienko, P. Vavassori, Y. Otani, and S. Bader, Physical Review B **66**, 052407 (2002).

[51] L. Giovannini, F. Montoncello, F. Nizzoli, G. Gubbiotti, G. Carlotti, T. Okuno, T. Shinjo, and M. Grimsditch, Physical Review B 172404 (2004).

[52] M. D. Stiles and J. Miltat, in *Spin Dynamics in Confined Magnetic Structures III*, Vol. 101 of *Topics in Applied Physics*, edited by B. Hillebrands and A. Thiaville (Springer-Verlag, Berlin Heidelberg, 2006), pp. 225–308.

[53] R. M. Martin, *Electronic Structure: Basic Theory and Practical Methods*, 2011 paperback edition ed. (Cambridge University Press, Cambridge, UK, 2004).

[54] W. Heisenberg, Zeitschrift für Physik **49**, (1928).

[55] M. d'Aquino, Ph.D. thesis, University of Napoli, 2004.

[56] N. A. Usov and S. E. Peschany, Journal of Magnetism and Magnetic Materials **118**, L290 (1993).

[57] C. Zaspel, B. A. Ivanov, J. Park, and P. Crowell, Physical Review B **72**, 024427 (2005).

[58] R. Zivieri and F. Nizzoli, Physical Review B **78**, 064418 (2008).

[59] B. Skubic, J. Hellsvik, L. Nordström, and O. Eriksson, Journal of Physics: Condensed Matter **20**, 315203 (2008).

[60] D. C. Ralph and M. D. Stiles, Journal of Magnetism and Magnetic Materials **320**, 1190 (2008).

[61] D. L. Mills and S. M. Rezende, *Spin Dynamics in Confined Magnetic Structures II* (Springer-Verlag, Heidelberg, 2003), Chap. 2, p. 27.

[62] Y. Tserkovnyak and A. Brataas, Reviews of Modern Physics **77**, (2005).

[63] C. Andreas, S. Gliga, and R. Hertel, Journal of Magnetism and Magnetic Materials **362**, 7 (2014).

[64] J. Jackson, *Classical Electrodynamics*, 3 ed. (Wiley, New York, NY, USA, 1999).

[65] W. F. Jr. Brown, *Magnetostatic Principles in Ferromagnetism* (Wiley-Interscience, New York, NY, USA, 1962).

[66] A. J. Newell, W. Williams, and D. J. Dunlop, **98**, 9551 (1993).

[67] M. Schabes and A. Aharoni, IEEE Transactions on Magnetics **23**, 3882 (1987).

[68] C. Abert and G. Selke, IEEE Transactions on Magnetics **48**, 1105 (2012).

[69] A. M. Chang, H. D. Hallen, L. Harriott, H. F. Hess, H. L. Kao, J. Kwo, R. E. Miller, R. Wolfe, J. Van Der Ziel, and T. Y. Chang, Applied Physics Letters **61**, 1974 (1992).

[70] Y. Martin and H. K. Wickramasinghe, Applied Physics Letters **50**, 1455 (1987).

[71] J. Ha, R. Hertel, and J. Kirschner, Physical Review B **67**, 064418 (2003).

[72] J. Ha, R. Hertel, and J. Kirschner, Physical Review B **67**, 224432 (2003).

[73] G. M. Wysin, in *Electromagnetic, Magnetostatic and Exchange Interaction Vortices in Confined Magnetic Structures*, edited by Eugene Kamenetskii (Research Signpost, India, 2009), Vol. 56, Chap. Influence of a perpendicular current on the circulation of a pinned magnetic vortex.

[74] A. Thiaville, J. García, R. Dittrich, J. Miltat, and T. Schrefl, Physical Review B **67**, 094410 (2003).

[75] E. Feldtkeller and H. Thomas, Physik der kondensierten Materie **4**, 8 (1965).

[76] W. F. Jr. Brown, *Micromagnetics* (Wiley, New York, NY, USA, 1963).

[77] R. Höllinger, A. Killinger, and U. Krey, Journal of Magnetism and Magnetic Materials **261**, 178 (2003).

[78] K. L. Metlov, Journal of Magnetism and Magnetic Materials **343**, 55 (2013).

[79] A. Aharoni, Journal of Applied Physics **68**, 255 (1990).

[80] V. Novosad, K. Guslienko, H. Shima, Y. Otani, S. Kim, K. Fukamichi, N. Kikuchi, O. Kitakami, and Y. Shimada, Physical Review B **65**, 2 (2002).

[81] S. Sugimoto, Y. Fukuma, S. Kasai, T. Kimura, A. Barman, and Y. Otani, Physical Review Letters **106**, 197203 (2011).

[82] K. W. Chou, A. Puzic, H. Stoll, G. Schütz, B. van Waeyenberge, T. Tyliszczak, K. Rott, G. Reiss, H. Brückl, I. Neudecker, D. Weiss, and C. H. Back, Journal of Applied Physics **99**, 08F305 (2006).

[83] S.-H. Jun, J.-H. Shim, S.-K. Oh, S.-C. Yu, D.-H. Kim, B. Mesler, and P. Fischer, Applied Physics Letters **95**, 142509 (2009).

[84] O. V. Sukhostavets, G. R. Aranda, and K. Y. Guslienko, Journal of Applied Physics **111**, 093901 (2012).

[85] P. Grünberg, R. Schreiber, Y. Pang, M. B. Brodsky, and H. Sowers, Physical Review Letters **57**, (1986).

[86] C. F. Majkrzak, J. W. Cable, J. Kwo, M. Hong, D. B. McWhan, Y. Yafet, J. V. Waszczak, and C. Vettier, Physical Review Letters **56**, 2700 (1986).

[87] M. B. Salamon, S. Sinha, J. J. Rhyne, J. E. Cunningham, R. W. Erwin, J. Borchers, and C. P. Flynn, Physical Review Letters **56**, (1986).

[88] S. S. P. Parkin, N. More, and K. P. Roche, Physical Review Letters **64**, (1990).

[89] M. E. Brubaker, J. E. Mattson, C. H. Sowers, and S. D. Bader, Applied Physics Letters **58**, 2306 (1991).

[90] A. Cebollada, J. L. Martinez, J. M. Gallego, J. J. de Miguel, R. Miranda, S. Ferrer, F. Batallan, G. Fillion, and J. P. Rebouillat, Physical Review B **39**, 9726 (1989).

[91] G. Binasch and P. Grünberg, Physical Review B **39**, 4828 (1989).

[92] S. Petit-Watelot, J.-V. Kim, A. Ruotolo, R. M. Otxoa, K. Bouzehouane, J. Grollier, A. Vansteenkiste, B. van de Wiele, V. Cros, and T. Devolder, Nature Physics **8**, 682 (2012).

[93] K. Y. Guslienko, Journal of Nanoscience and Nanotechnology **8**, 2745 (2008).

[94] E. Y. Tsymbal and D. G. Pettifor, in *Solid State Physics*, edited by H. Ehrenreich and F. Saepen (Academic Press, Cambridge, United Kingdom, 2001), Vol. 56, Chap. Perspectives of Giant Magnetoresistance, pp. 113–237.

[95] K. Nagasaka, Journal of Magnetism and Magnetic Materials **321**, 508 (2009), current Perspectives: Perpendicular Recording.

[96] U. Mizutani, *Introduction to the Electron Theory of Metals* (Cambridge University Press, Cambridge, United Kingdom, 2001).

[97] B. Dieny, V. S. Speriosu, S. S. P. Parkin, B. A. Gurney, D. R. Wilhoit, and D. Mauri, Physical Review B **43**, 1297 (1991).

[98] R. Wieser, Physical Review Letters **110**, 147201 (2013).

[99] M. Lakshmanan, Philosophical Transactions of the Royal Society of London A: Mathematical, Physical and Engineering Sciences **369**, 1280 (2011).

[100] G. Rado and J. Weertman, Journal of Physics and Chemistry of Solids **11**, 315 (1959).

[101] C. Abert, F. Bruckner, C. Vogler, R. Windl, and D. Suess, A full-fledged micromagnetic code in less than 70 lines of NumPy, 2014.

[102] M. D. Stiles, W. M. Saslow, M. J. Donahue, and A. Zangwill, (2008).

[103] N. Smith, Physical Review B **78**, 216401 (2008).

[104] W. M. Saslow, Journal of Applied Physics **105**, 07D315 (2009).

[105] M. Stiles and A. Zangwill, Physical Review B **66**, 1 (2002).

[106] J. C. Slonczewski, Journal of Magnetism and Magnetic Materials **159**, L1 (1996).

[107] L. Berger, Physical Review B **54**, 9353 (1996).

[108] J. C. Slonczewski, Journal of Magnetism and Magnetic Materials **195**, L261 (1999).

[109] J. C. Slonczewski, Journal of Magnetism and Magnetic Materials **247**, 324 (2002).

[110] P. M. Haney, H. W. Lee, K. J. Lee, A. Manchon, and M. D. Stiles, Physical Review B **87**, 1 (2013).

[111] J. Xiao, Ph.D. thesis, Georgia Institute of Technology, 2006.

[112] X. Waintal, E. Myers, P. Brouwer, and D. Ralph, Physical Review B **62**, 12317 (2000).

[113] A. Manchon, N. Strelkov, N. Ryzhanova, A. Vedyayev, B. Dieny, and J. C. Slonczewski, Journal of Magnetism and Magnetic Materials **316**, e977 (2007).

[114] M. Tsoi, A. Jansen, J. Bass, W.-C. Chiang, M. Seck, V. Tsoi, and P. Wyder, Physical Review Letters **80**, 4281 (1998).

[115] E. B. Myers, Science **285**, 867 (1999).

[116] M. Tsoi, A. G. M. Jansen, J. Bass, W.-C. Chiang, V. Tsoi, and P. Wyder, Nature **406**, 46 (2000).

[117] S. I. Kiselev, J. C. Sankey, I. N. Krivorotov, N. C. Emley, R. J. Schoelkopf, R. A. Buhrman, and D. C. Ralph, Nature **425**, 380 (2003).

[118] M. D. Stiles and A. Zangwill, Journal of Applied Physics **91**, (2002).

[119] B. T. Jonker, A. T. Hanbicki, D. T. Pierce, and M. D. Stiles, Journal of Magnetism and Magnetic Materials **277**, 24 (2004).

[120] M. D. Stiles, Journal of Applied Physics **79**, 5805 (1996).

[121] Y. Bazaliy, B. Jones, and S.-C. Zhang, Physical Review B **57**, R3213 (1998).

[122] A. A. Thiele, Physical Review Letters **30**, 3 (1973).

[123] D. L. Huber, Journal of Applied Physics **53**, 1899 (1982).

[124] D. L. Huber, Physical Review B **26**, (1982).

[125] G. M. Wysin, Physical Review B **54**, 15156 (1996).

[126] B. A. Ivanov, H. J. Schnitzer, F. G. Mertens, and G. M. Wysin, Physical Review B **58**, 8464 (1998).

[127] B. A. Ivanov, G. G. Avanesyan, A. V. Khvalkovskiy, N. E. Kulagin, C. E. Zaspel, and K. A. Zvezdin, JETP Letters **91**, 178 (2010).

[128] F. Mertens, H. Schnitzer, and A. Bishop, Physical Review B **56**, 2510 (1997).

[129] K. Y. Guslienko, R. H. Heredero, and O. Chubykalo-Fesenko, Physical Review B **82**, 014402 (2010).

[130] G. M. Wysin, Journal of Physics: Condensed Matter **22**, 376002 (2010).

[131] K. Y. Guslienko, B. A. Ivanov, V. Novosad, Y. Otani, H. Shima, and K. Fukamichi, Journal of Applied Physics **91**, 8037 (2002).

[132] J. P. Park, P. Eames, D. M. Engebretson, J. Berezovsky, and P. A. Crowell, Physical Review B **67**, 020403 (2003).

[133] A. Thiaville, Y. Nakatani, J. Miltat, and Y. Suzuki, Europhysics Letters **69**, 990 (2005).

[134] S. Kasai, P. Fischer, M. Im, K. Yamada, Y. Nakatani, K. Kobayashi, H. Kohno, and T. Ono, Physical Review Letters **101**, 237203 (2008).

[135] S. S. Cherepov, B. C. Koop, A. Yu. Galkin, R. S. Khymyn, B. A. Ivanov, D. C. Worledge, and V. Korenivski, Physical Review Letters **109**, 097204 (2012).

[136] B. Krüger, M. Najafi, S. Bohlens, R. Frömter, D. P. F. Möller, and D. Pfannkuche, Physical Review Letters **104**, 077201 (2010).

[137] L. Heyne, J. Rhensius, D. Ilgaz, A. Bisig, U. Rüdiger, M. Kläui, L. Joly, F. Nolting, L. J. Heyderman, J. U. Thiele, and F. Kronast, Physical Review Letters **105**, 1 (2010).

[138] S. D. Pollard, L. Huang, K. S. Buchanan, D. A. Arena, and Y. Zhu, Nature Communications **3**, 1028 (2012).

[139] Q. F. Xiao, J. Rudge, B.C. Choi, Y. K. Hong, and G. Donohoe, Applied Physics Letters **89**, 262507 (2006).

[140] K. Guslienko, W. Scholz, R. Chantrell, and V. Novosad, Physical Review B **71**, 144407 (2005).

[141] S. B. Choe, Journal of Magnetics **12**, 113 (2007).

[142] V. S. Pribiag, I. N. Krivorotov, G. D. Fuchs, P. M. Braganca, O. Ozatay, J. C. Sankey, D. C. Ralph, and R. A. Buhrman, Nature Physics **3**, 498 (2007).

[143] T. Devolder, A. Meftah, K. Ito, J. A. Katine, P. Crozat, and C. Chappert, Journal of Applied Physics **101**, 063916 (2007).

[144] A. Khvalkovskiy, J. Grollier, A. Dussaux, K. Zvezdin, and V. Cros, Physical Review B **80**, 140401 (2009).

[145] A. V. Khvalkovskiy, J. Grollier, N. Locatelli, Ya. V. Gorbunov, K. A. Zvezdin, and V. Cros, Applied Physics Letters **96**, 212507 (2010).

[146] J. Shibata, K. Shigeto, and Y. Otani, Physical Review B **67**, 224404 (2003).

[147] J. Shibata, K. Shigeto, and Y. Otani, Journal of Magnetism and Magnetic Materials **272**, 1688 (2004).

[148] Y. Lu, Z. Zhang, and Y. Liu, Journal of Applied Physics **109**, 103906 (2011).

[149] J. F. Pulecio, P. Warnicke, and S. D. Pollard, Nature Communications **5**, (2014).

[150] A. D. Belanovsky, N. Locatelli, P. N. Skirdkov, F. Abreu Araujo, J. Grollier, K. A. Zvezdin, V. Cros, and A. K. Zvezdin, Physical Review B **85**, 100409 (2012).

[151] R. Hertel, S. Gliga, M. Fähnle, and C. Schneider, Physical Review Letters **98**, 117201 (2007).

[152] D. J. Keavney, X. M. Cheng, and K. S. Buchanan, Applied Physics Letters **94**, 172506 (2009).

[153] B. Pigeau, G. de Loubens, O. Klein, A. Riegler, F. Lochner, G. Schmidt, and L. W. Molenkamp, Nature Physics **7**, 26 (2010).

[154] J. Caputo, Y. Gaididei, F. Mertens, and D. Sheka, Physical Review Letters **98**, 056604 (2007).

[155] Y. Liu, H. He, and Z. Zhang, Applied Physics Letters **91**, 242501 (2007).

[156] Y.-S. Choi, S.-K. Kim, K.-S. Lee, and Y.-S. Yu, Applied Physics Letters **93**, 182508 (2008).

[157] K. Yamada, S. Kasai, Y. Nakatani, K. Kobayashi, and T. Ono, Applied Physics Letters **93**, 152502 (2008).

[158] D. Cimpoesu, H. Pham, A. Stancu, and L. Spinu, Journal of Applied Physics **104**, 113918 (2008).

[159] K. Nakano, K. Tanabe, R. Hiramatsu, D. Chiba, N. Ohshima, S. Kasai, T. Sato, Y. Nakatani, K. Sekiguchi, K. Kobayashi, and T. Ono, Applied Physics Letters **102**, 072405 (2013).

[160] R. Wang and X. Dong, Applied Physics Letters **100**, (2012).

[161] M.-W. Yoo, J. Lee, and S.-K. Kim, Applied Physics Letters **100**, 172413 (2012).

[162] X. Dong, Z. Wang, and R. Wang, Applied Physics Letters **104**, 112413 (2014).

[163] K.-W. Moon, B. S. Chun, W. Kim, Z. Q. Qiu, and C. Hwang, Scientific Reports **4**, 6170 (2014).

[164] M. Kammerer, H. Stoll, M. Noske, M. Weigand, G. Woltersdorf, and G. Schuetz, 1 (2011).

[165] M. Sproll, M. Noske, H. Bauer, M. Kammerer, A. Gangwar, G. Dieterle, M. Weigand, H. Stoll, G. Woltersdorf, C. H. Back, and G. Schtz, Applied Physics Letters **104**, 012409 (2014).

[166] R. Rückriem, T. Schrefl, and M. Albrecht, Applied Physics Letters **104**, 052414 (2014).

[167] M. Schneider, H. Hoffmann, and J. Zweck, Applied Physics Letters **79**, 3113 (2001).

[168] S. Yakata, M. Miyata, S. Nonoguchi, H. Wada, and T. Kimura, Applied Physics Letters **222503**, 1878 (2010).

[169] S. Yakata, M. Miyata, S. Honda, H. Itoh, H. Wada, and T. Kimura, Applied Physics Letters **99**, 242507 (2011).

[170] M. Jaafar, R. Yanes, D. Perez de Lara, O. Chubykalo-Fesenko, A. Asenjo, E. M. Gonzalez, J. V. Anguita, M. Vazquez, and J. L. Vicent, Physical Review B **81**, 054439 (2010).

[171] Y. Wen, Z. Feng, B. F. Miao, R. X. Cao, L. Sun, B. You, D. Wu, W. Zhang, Z. S. Jiang, R. Cheng, and H. F. Ding, Journal of Magnetism and Magnetic Materials **370**, 68 (2014).

[172] V. Uhlíř, M. Urbánek, L. Hladík, J. Spousta, M.-Y. Im, P. Fischer, N. Eibagi, J. J. Kan, E. E. Fullerton, and T. Sikola, Nature Nanotechnology **8**, 341 (2013).

[173] M. Urbánek, V. Uhlíř, C.-H. Lambert, J. J. Kan, N. Eibagi, M. Vařatka, L. Flajšman, R. Kalousek, M.-Y. Im, P. Fischer, T. Šikola, and E. E. Fullerton, Physical Review B **91**, 1 (2015).

[174] Y. Gaididei, D. D. Sheka, and F. G. Mertens, Applied Physics Letters **92**, 3 (2008).

[175] R. Antos and Y. Otani, Physical Review B **80**, 140404 (2009).

[176] C. Zaspel, E. Wright, A. Galkin, and B. A. Ivanov, Physical Review B **80**, 094415 (2009).

[177] J. Kolthammer, R. Gardner, Th. Speliotis, Y. K. Hong, G. Abo, Q. Liu, and B. C. Choi, Journal of Applied Physics **112**, (2012).

[178] N. Locatelli, V. V. Naletov, J. Grollier, G. de Loubens, V. Cros, C. Deranlot, C. Ulysse, G. Faini, O. Klein, and A. Fert, Applied Physics Letters **98**, 062501 (2011).

[179] B. C. Choi, J. Rudge, E. Girgis, J. Kolthammer, Y. K. Hong, and A. Lyle, Applied Physics Letters **91**, 2005 (2007).

[180] Y.-S. Choi, M.-W. Yoo, K.-S. Lee, Y.-S. Yu, H. Jung, and S.-K. Kim, Applied Physics Letters **96**, 072507 (2010).

[181] M. T. Moneck and J.-G. Zhu, IEEE Transactions on Magnetics **44**, 2500 (2008).

[182] M. Buess, T. P. J. Knowles, R. Höllinger, T. Haug, U. Krey, D. Weiss, D. Pescia, M. R. Scheinfein, and C. H. Back, Physical Review B **71**, 104415 (2005).

[183] V. V. Naletov, G. de Loubens, G. Albuquerque, S. Borlenghi, V. Cros, G. Faini, J. Grollier, H. Hurdequint, N. Locatelli, B. Pigeau, A. N. Slavin, V. S. Tiberkevich, C. Ulysse, T. Valet, and O. Klein, Physical Review B **84**, 224423 (2011).

[184] K. Y. Guslienko and A. N. Slavin, Journal of Applied Physics **87**, 6337 (2000).

[185] B. A. Ivanov and C. E. Zaspel, Applied Physics Letters **81**, 1261 (2002).

[186] B. A. Ivanov and C. E. Zaspel, Physical Review Letters **94**, 23 (2005).

[187] K. Guslienko, S. Demokritov, B. Hillebrands, and A. Slavin, Physical Review B **66**, 8 (2002).

[188] K. Guslienko and A. Slavin, Physical Review B **72**, 014463 (2005).

[189] X. Zhu, Z. Liu, V. Metlushko, P. Grütter, and M. Freeman, Physical Review B **71**, 180408 (2005).

[190] F. Hoffmann, G. Woltersdorf, K. Perzlmaier, A. Slavin, V. Tiberkevich, A. Bischof, D. Weiss, and C. Back, Physical Review B **76**, 014416 (2007).

[191] J. Park and P. Crowell, Physical Review Letters **95**, 167201 (2005).

[192] I. Neudecker, K. Perzlmaier, F. Hoffmann, G. Woltersdorf, M. Buess, D. Weiss, and C. Back, Physical Review B **73**, 134426 (2006).

[193] K. Vogt, O. Sukhostavets, H. Schultheiss, and B. Obry, Physical Review B **174401**, 1 (2011).

[194] O. Dmytriiev, T. Meitzler, E. Bankowski, A. Slavin, and V. Tiberkevich, Journal of Physics: Condensed Matter **22**, 136001 (2010).

[195] O. Heinonen, Physical Review B **92**, 054420 (2015).

[196] M. R. Scheinfein, http://llgmicro.home.mindspring.com.

[197] J. E. Kolthammer, J. Rudge, B. C. Choi, and Y. K. Hong, Spin **6**, 1650008 (2016).

[198] M. R. Mozaffari and K. Esfarjani, Physica B: Condensed Matter **399**, 81 (2007).

[199] S. Jain, V. Novosad, F. Y. Fradin, J. E. Pearson, and S. D. Bader, Applied Physics Letters **104**, 082409 (2014).

[200] D. Kumar, S. Barman, and A. Barman, Scientific Reports **4**, 4108 (2014).

[201] R. Kergoat, M. Labrune, J. Miltat, T. Valet, and J. C. Jacquet, Journal of Magnetism and Magnetic Materials **121**, 339 (1993).

[202] E. Chen, D. Apalkov, Z. Diao, A. Driskill-Smith, D. Druist, D. Lottis, V. Nikitin, X. Tang, S. Watts, S. Wang, and S. A. Wolf, IEEE Transactions on Magnetics **46**, 1873 (2010).

[203] J. J. Nowak, R. P. Robertazzi, J. Z. Sun, G. Hu, J. H. Park, J. Lee, A. J. Annunziata, G. P. Lauer, R. Kothandaraman, E. J. O'Sullivan, P. L. Trouilloud, Y. Kim, and D. C. Worledge, IEEE Magnetics Letters **7**, 4 (2016).